UNIVERSITY OF CALIFORNIA,

IRVINE

Unconventional methods of controlling microstructures to tailor the mechanical behavior of polycrystalline solids

DISSERTATION

submitted in partial satisfaction of the requirements for the degree of

DOCTOR OF PHILOSOPHY

in Materials Science and Engineering

by

Salma El-Azab

Dissertation Committee:

Professor Julie M. Schoenung, Chair

Professor Daniel Mumm

Professor Shen Dillon

2024

DEDICATION

To my parents

for everything that they have given me

TABLE OF CONTENTS

LIST OF FIGURES

Chapter 3

Chapter 4

LIST OF TABLES

LIST OF FORMULAE

ACKNOWLEDGEMENTS

I would like to thank my advisor, Professor Julie Schoenung, for her support throughout my time in graduate school. Her perspectives and guidance have made a huge impact on me and my development as a scientist. I am extremely thankful to her for the unique opportunities that she gave me both inside and outside of my research, and for all the encouragement she gave me to explore everything that the field of materials engineering has to offer.

I would also like to express my sincere gratitude to Professor Alexander Dupuy. His mentorship was essential to the successful completion of my PhD. Alex always went above and beyond to make sure that I had everything I needed to succeed, and I could not thank him enough. I would also like to thank Professor Xin Wang for all the great advice that she gave me throughout the years, and the expertise that she contributed to my work. I wish both the best of luck, although I'm sure they don't need it.

Thank you to my group mates, Justin Cortez and Jacob Norman, who have become family to me. I will miss them immensely and cherish all our memories in the office and in the lab dearly. Thank you to Drs. Katherine Acord, Aleksandra Vyatskikh, Arturo Meza, Sen Jiang, Parnian Kiani, Benjamin MacDonald, Kehang Yu, and other JMS/EJL group alum, who were great role models to me in the earlier years of my time in graduate school.

Thank you to Baolong Zheng, Darryl Mack, and Yizhang Zhou for all their support with my research behind the scenes. I learned so much about how to operate a lab, and I couldn't have survived without you all. I'd also like to thank Drs. Jian-Guo Zheng and Qiyin Li, and the rest of the IMRI staff for all the help they provided me with my characterization. I'd also like to thank Sakshi Bajpai and Brandon Fields for all their assistance with the ACRC equipment, and Professor Diran Apelian for allowing me to use his spaces, as well as all the wisdom and generosity that he showed me over the years.

Thank you to Luz Gomez and Alina Vizcaya for being such wonderful mentees and friends to me. I will never forget our camping trip and how chaotic and fun it was. I am immensely proud of both of you and I can't wait to see all the amazing things you both accomplish. I'd like to also thank the remaining undergraduate students that I worked with, many who have now graduated and gone to graduate school: Yiheng, Noriki, and Onus.

Thank you to my committee members, Professors Daniel Mumm and Shen Dillon, for their helpful feedback and insights. Thank you, Dan for encouraging me to come to UCI during my visit day. Thank you, Professors Stacy Copp and Timothy Rupert, for writing letters of recommendation for my NSF GRFP application. Thank you to our front office staff, Viviana Saadalla, Amy Ricks, and Desiree Rios, for all the support they provided throughout the years, and for their help with GSA.

Thank you to all the friends I made, both in and out of graduate school. To Sierra, Ethan, Calvin, Eshana, Abel, Naomy, Gigi, Vanessa, Aoon, Justin M., Rocky, Zahraa, Nada, Chloe, Peter S., Beto, and many others: I had such a blast with you all! Thank you for the memories and for always being down to do the most random things with me. I will miss you all so much.

I’d like to thank and acknowledge my mentors at Glidewell Dental Labs during my summer internship, Pavan Srivas and Dimple Pradhan, and the rest of the R&D team. I learned so many valuable lessons during my time at Glidewell, many of which I will carry into my future.

I’d like to give a shoutout to Hidden House Coffee in Santa Ana for being the best place to write and for having the perfect amount of natural light to focus on my work. Also, shout out to Shirley’s Bagels for just having the best bagel sandwiches I’ve ever had.

I’d like to acknowledge the brave journalists and reporters in Gaza for risking their lives to show the world the truth about what is happening in their homeland. May they one day know peace and may the world one day see a free Palestine.

Thank you to my family Professor Mohamed Abdou and his wife Soraya for opening up their home to me. Thank you to my parents, Anter & Sally, and my sister Sarah, for their unwavering love and support that carried me through some of the most difficult moments of my life. I love you all so much. Also, shoutout to Doobie, Boobie, Monty, and Simsim for being the cutest critters ever. Rest in peace, Boobie and Monty.

Some text in this dissertation is a reprint of the material as it appears in *Scientific Reports*. It is fairly used with permission according to the guidelines. Thank you to my co-authors Cheng Zhang, Sen Jiang, Aleksandra Vyatskikh, Lorenzo Valdevit, Enrique Lavernia, and Julie Schoenung.

Lastly, I’d like to acknowledge the funding support provided by UC Irvine, the National Science Foundation, the Army Research Office, and the ARCS Foundation.

CURRICULUM VITAE

EDUCATION

University of California, Irvine, *Irvine, California*
Ph.D. candidate in Materials Science & Engineering
Master of Science in Materials Science & Engineering [December 2020]
Department of Materials Science & Engineering

Purdue University, *West Lafayette, Indiana*
Bachelor of Science in Materials Engineering [May 2019]
Department of Materials Engineering

PUBLICATIONS

- **Mechanical behavior of multiphase entropy-stabilized oxides**
  Salma A. El-Azab, Jacob E. Norman, Luz Gomez, Alexander D. Dupuy, Julie M. Schoenung
  Under review
- ***In situ* observation of melt pool evolution during ultrasonic vibration-assisted directed energy deposition**
  Salma A. El-Azab, Cheng Zhang, Sen Jiang, Aleksandra L. Vyatskikh, Lorenzo Valdevit, Enrique Lavernia, Julie M. Schoenung
  Scientific Reports, October 2023
- **Thickness Dependent Microstructure in Additively Manufactured Stainless Steel**
  Aleksandra L. Vyatskikh, Thomas B. Slagle, Sen Jiang, Salma A. El-Azab, Umberto Scipioni Bertoli, Lorenzo Valdevit, Enrique Lavernia, Julie M. Schoenung
  Journal of Materials Engineering and Performance, June 2021

ORAL PRESENTATIONS

- **Mechanical behavior of multiphase entropy stabilized oxides** Winter 2023
  TMS, San Diego, CA
- ***In situ* observation of melt pool evolution in ultrasonic vibration-assisted directed energy deposition** Winter *2022*
  TMS, Anaheim, CA
- **Fabrication of Tungsten Carbide Cobalt via Laser Engineered Net Shaping** Summer 2019
  UC Irvine Summer Research Symposium, Irvine, CA
- **Value Recovery of Hard Disk Drives at Purdue University** Spring 2019
  University Surplus Property Association's National Conference, Columbus, OH
- **Life Cycle Analysis: Economics of Reuse for Purdue Surplus Hard Disk Drives** Spring 2018
  University Surplus Property Association's National Conference, West Lafayette, IN

POSTER PRESENTATIONS

- **Residual Stress Mitigation in Metal Additive Manufacturing Using Compositional Engineering** Winter 2022
  TMS, Anaheim, CA
- **Intermetallic Growth in Transient Liquid Phase Bonding** Fall 2018
  MS&T, Columbus, OH
- **Life Cycle Analysis: Economics of Reuse for Purdue Surplus Hard Disk Drives** Spring 2018
  Cascade Open House, Indianapolis, IN
- **Intermetallic Growth in Transient Liquid Phase Bonding** Spring 2018
  Purdue Undergraduate Research Symposium, West Lafayette, IN

EMPLOYMENT

Grant writing consultant Fall 2023

Rekovar, Irvine, CA

- Wrote project summary, project narrative, and commercialization plan for NIH grant
- Created figures and edited additional documents

Ceramics R&D Intern Summer 2023

Glidewell, Irvine, CA

- Improved machinability of zirconia dental implants by 200% by optimizing dopant concentrations and sintering routes

Consultant Fall 2022 – Spring 2023

Syntec Associates, Irvine, CA

- Developed models to quantify and compare energy consumption of additive manufacturing processes
- Compiled findings into technical report for industry stakeholders

Writer Summer 2021 – Summer 2022

The Loh Down on Science, Irvine, CA

- Wrote scripts based on interdisciplinary scientific literature for NPR-sponsored radio show broadcasted to lay audience of over 4 million

Metallurgical Intern Summer 2018

Nucor Steel, Decatur, AL

- Tracked sulfur and calcium content in steel at ladle metallurgical furnace to determine cause of contamination and defects using SEM and EDS to reduce defects in steel and improve clean steel practices

Teaching Assistant Fall 2017

Department of Materials Engineering, Purdue University

- Assisted with grading coursework and held weekly office hours for MSE 25000 and MSE 27000

IT Projects Assistant Summer 2015 – Summer 2019

Department of Biological Sciences, Purdue University

- Filmed and edited outreach videos and safety protocol tutorials to promote undergraduate research
- Created operational procedures for online servers for entire College of Science
- Identified need and budget for new equipment to support research and teaching efforts for 50+ faculty

HONORS

- **ARCS Foundation Scholar Award** Summer 2022
- **Loh Down on Science Fellowship** Spring 2021
- **National Science Foundation Graduate Research Fellowship** Spring 2021
- **Eugene Cota-Robles Fellowship** Spring 2019
- **Diversity Recruitment Fellowship** Spring 2019
- **Provost PhD Fellowship** Spring 2019
- **Matthew Slone Academic Excellence Award** Summer 2018
- **Purdue Moves Study Abroad Scholarship** Spring 2018
- **Office of Undergraduate Research Scholarship** Spring 2018
- **Purdue University Dean's List** Fall 2015 – Spring 2019
- **Presidential Scholarship** Spring 2015

SERVICE & OUTREACH

President's Council of Student Advisors Summer 2022 – Summer 2023

American Ceramic Society

- Served on Communications Committee; collaborated with 50+ undergraduate and graduate researchers
- Coordinated student writers for monthly publication *Bulletin* with global audience
- Created social media content on glass and ceramics science for Twitter, Instagram, and LinkedIn

Graduate Student Association Fall 2021 – Spring 2022

Department of Materials Science and Engineering, UC Irvine

- Served as president; led outreach, recruitment, and social initiatives
- Built pipelines of communication between students and department through quarterly townhalls
- Facilitated professional development opportunities for students, including fellowship writing workshops, research mixers, and monthly seminars with industry professionals

MSE at UCI Anti-Racism Working Group Summer 2020 – Summer 2023

Department of Materials Science and Engineering, UC Irvine

- Served as graduate student representative

SKILLS

- **Microscopy and Characterization**: Scanning Electron Microscopy, Optical Microscopy, X-Ray Diffraction, Energy Dispersive Spectroscopy, Atomic Force Microscopy, Automated Feature Analysis
- **Material Preparation**: Containment Chambers, Pellet Press, Coin Cell Assembly, Electrode Preparation, Solid State Synthesis, Tube Furnace, Sample Polishing, Rockwell Hardness Testing, Spark Plasma Sintering, Ball Milling
- **Software**: Java, MATLAB, Mathcad, Microsoft Office, ImageJ, OriginPro, R

ABSTRACT OF THE DISSERTATION

Unconventional methods of controlling microstructures to tailor the mechanical behavior of polycrystalline solids

By

Salma El-Azab

Doctor of Philosophy in Materials Science and Engineering

University of California, Irvine, 2024

Professor Julie M. Schoenung, Chair

As new materials and manufacturing techniques are developed to suit the needs of several key industries, creative methods of designing microstructures to tailor mechanical behavior must be explored to control deformation and prevent failure. Additionally, the underlying mechanisms that dictate such control must be well understood. To this end, this dissertation includes three distinct investigations: a study on the underling mechanisms that control the microstructure of samples fabricated with ultrasonic vibration-assisted directed energy deposition; an exploration of the role of phase state and composition on the room-temperature mechanical behavior of entropy stabilized oxides; and an analysis of the role of microstructure and phase state on the high-temperature deformation of entropy stabilized oxides.

In the first study, ultrasonic vibration (UV) was applied *in situ* to directed energy deposition (DED) of 316L stainless steel single tracks and bulk parts. For the first time, high-speed video imaging and thermal imaging were implemented *in situ* to quantitatively correlate the application of UV to melt pool evolution in DED. Findings show that UV increases the melt pool peak

temperature and dimensions, while improving the wettability of injected powder particles with the melt pool surface and reducing powder particle residence time. Through *in situ* imaging we demonstrate quantitatively that these phenomena, acting simultaneously, effectively diminish with increasing build height and size, consequently decreasing the positive effect of implementing UV-assisted (UV-A) DED. Thus, this research provides valuable insight into the effects of UV on DED melt pool dynamics, the stochastic interactions between the melt pool and incoming powder particles, and the limitations of build geometry on the UV-A DED technique.

In the second study, we investigate the influence of these secondary phases on the mechanical behavior of the (CoCuMgNiZn)O transition metal ESO (TM-ESO). TM-ESOs of equimolar, Co-deficient, and Cu-deficient compositions were fabricated, heat treated to form secondary phases, and characterized. Room-temperature indentation was used to measure the hardness and elastic modulus of as-sintered single-phase and as-heat-treated multiphase bulk samples. As the atomic fraction of secondary phase increases, equimolar and Co-deficient TM-ESO harden then soften, and Cu-deficient TM-ESO continuously hardens. Hardness trends were analyzed by evaluating strengthening mechanisms, indicating that hardness is significantly influenced by the interactions between dislocations and secondary phases. The elastic modulus varies as a function of composition and quantity of secondary phases but falls within a range of values predicted by a composite model. Changing composition influences the hardness and elastic modulus of as-sintered single-phase TM-ESOs due to changes in cation-dislocation and cation-cation interaction energies. Overall, our findings indicate that the entropic phase transformation can be manipulated to tailor the room-temperature mechanical properties of TM-ESOs.

In the third study, we begin to address the high-temperature deformation behavior of TM-ESOs. The microstructure and phase state of TM-ESOs were varied. Fine-grained and coarse-grained

TM-ESOs were deformed at increasing loads over a range of elevated temperatures in both their single-phase and multiphase states. Stress exponent values were determined for all conditions, indicating that fine-grained and coarse-grained TM-ESO deformed superplastically. In fine-grained TM-ESO samples, the secondary phases did not have a significant effect on the stress exponent values. At low deformation temperatures, coarse-grained TM-ESO samples had higher stress exponent values than fine-grained samples, and the stress exponent increased with the presence of secondary phases. At high deformation temperatures, the stress exponents for single-phase and multiphase coarse-grained samples decreased. The drop in stress exponent for the coarse-grained samples at higher deformation temperatures indicates a temperature-induced switch in the deformation mechanism from grain boundary sliding to solute-drag creep. Overall, this work demonstrates that microstructure and phase composition of TM-ESO can be used to tailor the high-temperature deformation of TM-ESO.

This dissertation highlights that unconventional methods can be used to tailor the microstructure of polycrystalline metal alloys and oxide ceramics to control their mechanical behavior. Future studies examining the mechanical properties of individual secondary phases in TM-ESOs, the kinetics of the reversible phase transformation of TM-ESOs, and the reversible phase transformation and room-temperature mechanical behavior of nanocrystalline TM-ESOs would be meaningful additions to the studies included in this dissertation.

Chapter 1: Introduction

One of the biggest challenges facing materials scientists is the need for materials with properties that satisfy the rapidly evolving demands of society and technology. Mechanical properties, such as strength, hardness, and elastic modulus, are of particular significance because they deal with the way materials respond to force, determining their practical utility and service lifetime [1]. As such, material design is guided by a necessity to understand the mechanical characteristics of a material, to produce parts where deformation is controlled, and failure is prevented [2]. This chapter provides a high-level discussion of processing-microstructure-property relationships as they relate to the experiments discussed in this dissertation.

1.1 Processing

The microstructure of a material can be easily tailored by the way that it is processed. There are a variety of ways to manufacture crystalline materials. Each technique has distinct parameters that can be controlled to achieve specific microstructures. This dissertation covers two techniques for processing polycrystalline materials: additive manufacturing and sintering.

1.1.1 Additive manufacturing

Additive manufacturing (AM) is a novel processing technique where a computer aided design (CAD) model is used to achieve three-dimensional (3D) net-shape parts by incrementally adding thin layers of material from the bottom up. AM is beneficial for creating complex components without need for extensive machining or tooling [3]. AM is also quite versatile and can be used to manufacture components made from metals, ceramics, and polymers. The versatility and ease of production of complex parts have made AM popular in aerospace, medical, energy, and automotive industries.

There are many AM technologies that can be used to make metal parts, like directed energy deposition (DED) [4], powder bed fusion (PBF) [5], electron beam melting (EBM) [6], and wire arc additive manufacturing (WAAM) [7]. Various AM technologies are represented in Fig. 1.1.

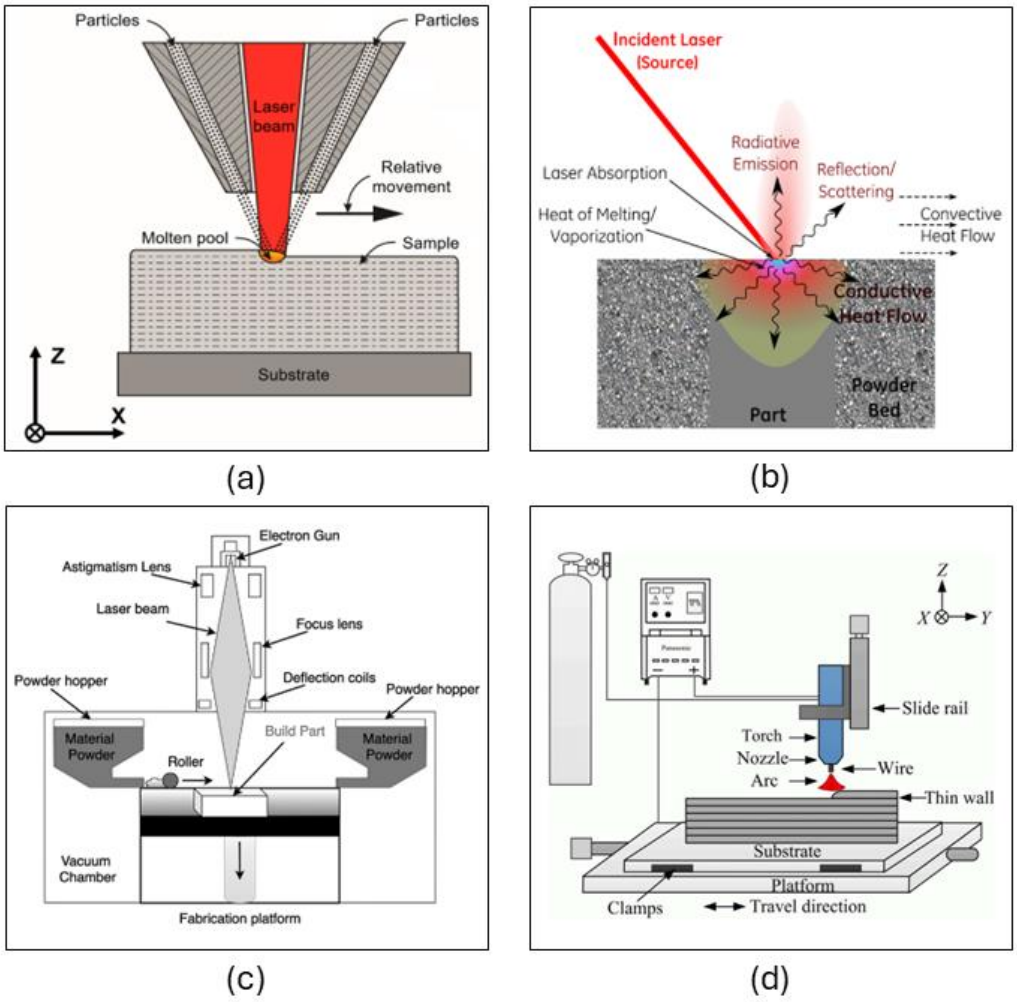

Figure 1.1: Various additive manufacturing technologies, including a) directed energy deposition [4], b) powder bed fusion [5], c) electron beam melting [6], and d) wire arc additive manufacturing [7].

These technologies use various feedstock materials like powder, wire, or sheets, and consolidate them into dense, net-shaped components through melting and solidification [3]. An energy source, like a laser, electron beam, or electron arc, is required to melt the material. DED uses a laser energy source to create a melt pool on the surface of a metal substrate, into which metal powder particles are injected. The laser or the stage raster in the X-Y direction, and the laser incrementally moves

up as the part is deposited. During DED, as layers are built, previously deposited layers are remelted and/or reheated. The substrate tends to act as a heat sink, drawing heat away from the melt pool at lower layers. As the build height increases, the substrate's intrinsic heat sink effects wear off, causing thermal accumulation in higher layers [8]. This dissertation covers a DED technique known as Laser Engineered Net Shaping© [9].

1.1.2 Sintering

Ceramics are typically created by compacting powder particles and heating it in a process known as sintering, which is a solid-state consolidation method [10]. Powder particles are first compacted to form a green body. In the green body, there are pores between the compacted powder particles. These pores must be eliminated to improve the mechanical strength and enhance other properties of the ceramic. The elimination of pores is achieved through sintering, which is a high-temperature heat treatment that densifies compacted powder particles into a polycrystalline microstructure [11]. The compacted powder particles are densified through solid-state atomic diffusion, which is driven by a gradient in chemical potential, causing atoms to diffuse from areas of high chemical potential to areas of low chemical potential through several mass transport mechanisms [11]. Sintering, as shown schematically in Fig. 1.2, is further described below.

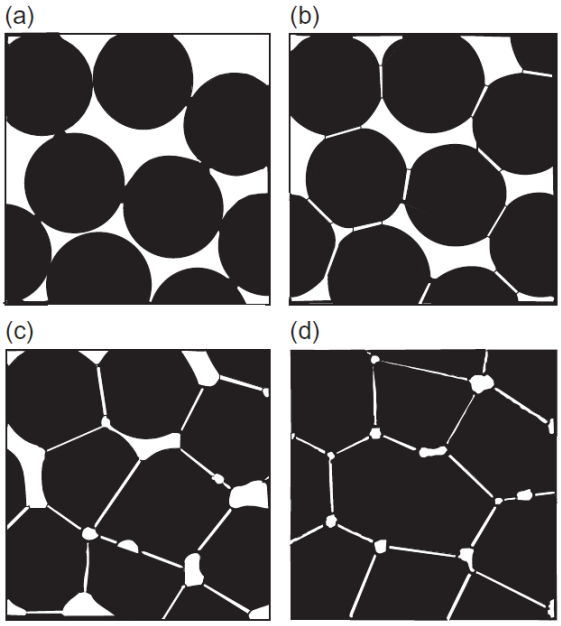

Figure 1.2: Schematics of microstructural evolution during the sintering process: a) powder compact, b) initial stage sintering, c), intermediate stage sintering, and d) final stage sintering [11].

Fig. 1.2a represents the compacted powder particles, where distinct powder particles are in contact with one another, forming pores. In Fig. 1.2b, initial stage sintering is shown. At this stage, heat is added to activate atomic diffusion, resulting in an increase in contact area between the powder particles. This phenomenon is known as necking, and is driven by a need to reduce the surface energy between powder particles [12]. Fig 1.2c represents intermediate stage sintering, where the space between the powder particles starts to decrease, and the powder particles start to take on a grain-like shape. Finally, the final stage of sintering is achieved, and powder particles become grains, as shown in Fig. 1.2d. At this final stage, the contact area between powder particles becomes a grain boundary, and the density of the part increases, causing its macroscopic geometric dimensions to shrink [11]. The driving mechanism for sintering is diffusion. There are several diffusion pathways during sintering, as demonstrated in Fig. 1.3 [13]. Mechanisms I-IV in Fig. 1.3 represent evaporation-condensation, surface diffusion, volume diffusion, and grain boundary diffusion, respectively.

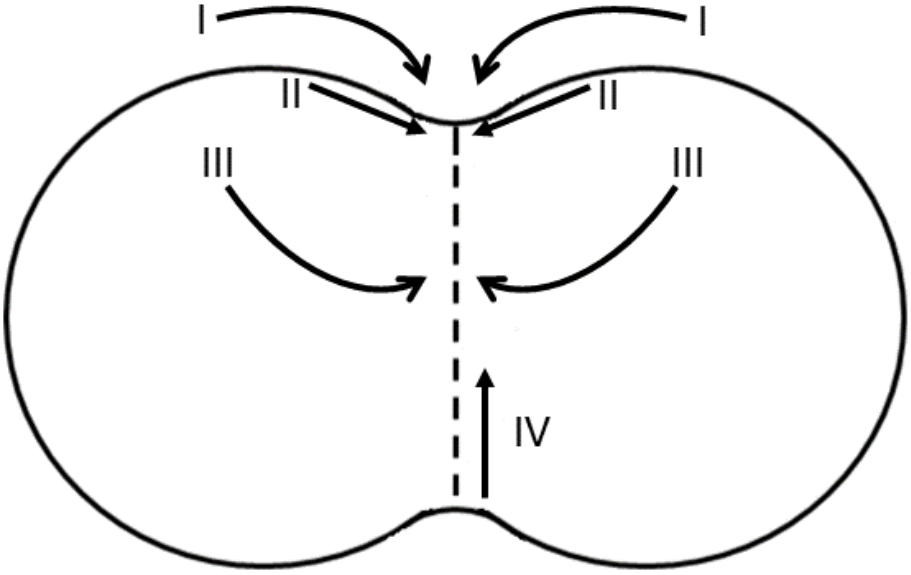

Figure 1.3: Diffusion mechanisms that occur during sintering [13].

Spark plasma sintering (SPS), also known as field-assisted sintering technique (FAST) or current-activated, pressure-assisted densification (CAPAD), is a sintering technique that has become quite popular over the last few decades. In SPS, a pulsed current is applied through electrodes at the top and bottom of the sintering apparatus [14]. The use of this electric current allows for fast heating rates and enhanced rates of solid-state diffusion, allowing for precise control over grain size and even the production of nanocrystalline materials [14]. The benefits of SPS are that it is an efficient process with fast fabrication times, and that it can be used to fabricate materials that are otherwise difficult to produce with other manufacturing techniques [14].

1.2 Microstructure

A material's microstructure can be described as its structural features that can be observed under a microscope [2]. Microstructural features can include things like grains, twins, precipitate particles, and cracks, among other things. These features can be controlled through processing to influence a material's mechanical behavior. The following discussion covers two microstructural features that are relevant to this dissertation: grain size and precipitates.

1.2.1 Grain size

In a crystalline material, internal boundaries act as obstacles to dislocation motion [15]. One such boundary is the grain boundary, which is particularly effective at impeding the movement of dislocations, because it blocks their path from one crystal to another of a different orientation. This results in a pile-up of dislocations at grain boundaries [15], shown schematically in Fig. 1.4.

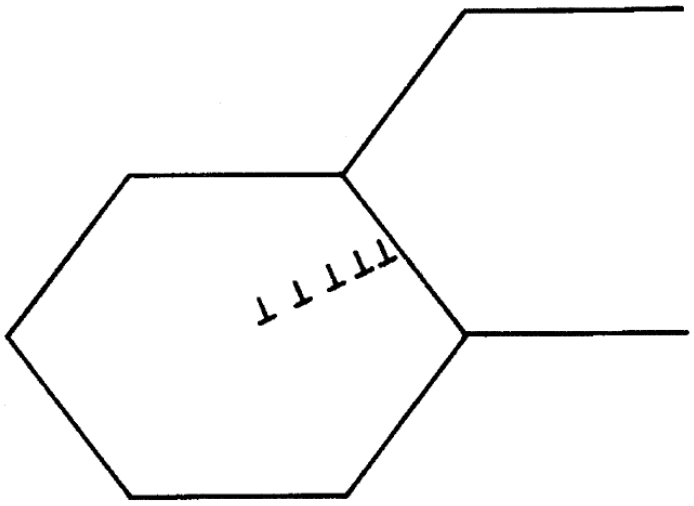

Figure 1.4: Schematic showing the pileup of dislocations at a grain boundary, adapted from [15].

By controlling the grain size, one can influence the way that dislocations pile up at the grain boundary, thereby influencing the material's overall mechanical behavior. This behavior is known as the Hall-Petch effect, which is a classic example of the influence of microstructure on a material's mechanical behavior. The Hall-Petch effect can be described mathematically in the equation below [15]:

$$\sigma_y = \sigma_0 + k_y d^{-1/2} \tag{1.1}$$

where σ_y is yield strength, σ_0 is a material constant for stress necessary to initiate dislocation movement, k_y is a strengthening coefficient, and d is average grain diameter. Eqn. 1.1 essentially states that a polycrystalline material's yield strength increases with decreasing grain size. This

increase in yield strength is due to an increase in overall grain boundary area to impede dislocation movement.

1.2.2 Precipitates

Precipitates, or particles of different phases, can form within a grain or at a grain boundary through solid-state diffusion, which can be activated by heat treatment at high temperatures [2, 15]. Secondary phase precipitate particles can influence a material's strength because they can resist dislocation motion, even if they are present in small volume fractions. The degree to which a secondary phase precipitate particle can contribute to strengthening a material depends on its size, volume fraction, shape, and lattice mismatch at its boundary with the matrix phase. At smaller precipitate particle sizes, there are several mechanisms for material strengthening, including coherency strengthening, modulus strengthening, and chemical strengthening, shown in Fig. 1.5.

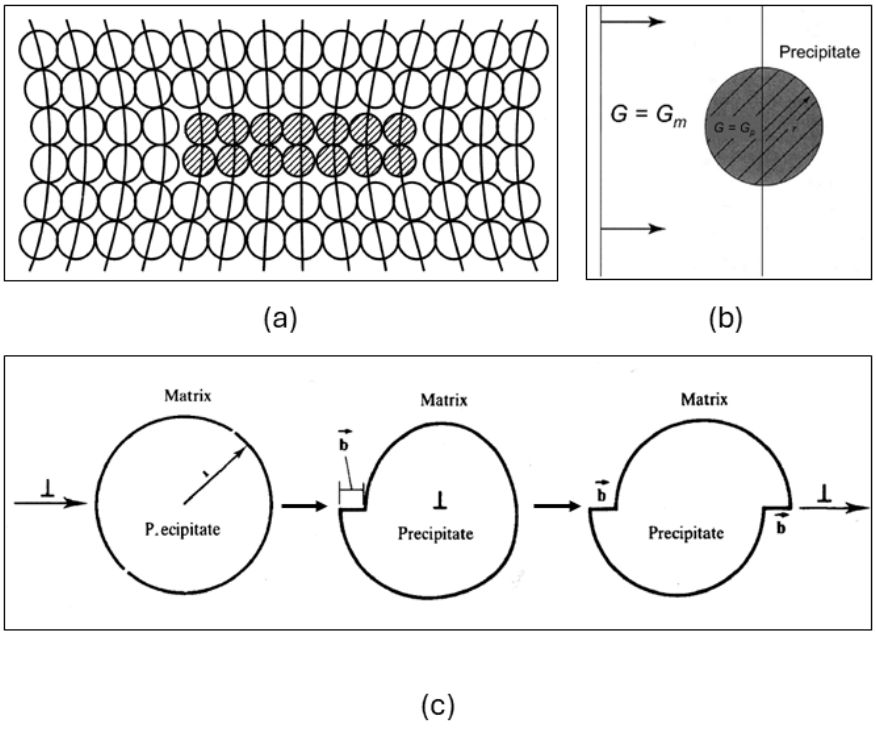

Figure 1.5: Various strengthening mechanisms at small secondary phase precipitate particle sizes, including a) coherency strengthening, b) modulus strengthening, and c) chemical strengthening. This figure is adapted from [15].

These strengthening mechanisms can happen simultaneously and are defined by the way that a dislocation interacts with the precipitate particle. When precipitate particles are larger, and the spacing between them is larger, the strengthening mechanism typically switches to a bypassing mechanism like Orowan looping [15]. In this case, the dislocations bow around the precipitate particle and continue to pass on through the matrix lattice, rather than interacting directly with the precipitate particle like as shown in Fig. 1.5. Orowan looping is schematically shown in Fig. 1.6.

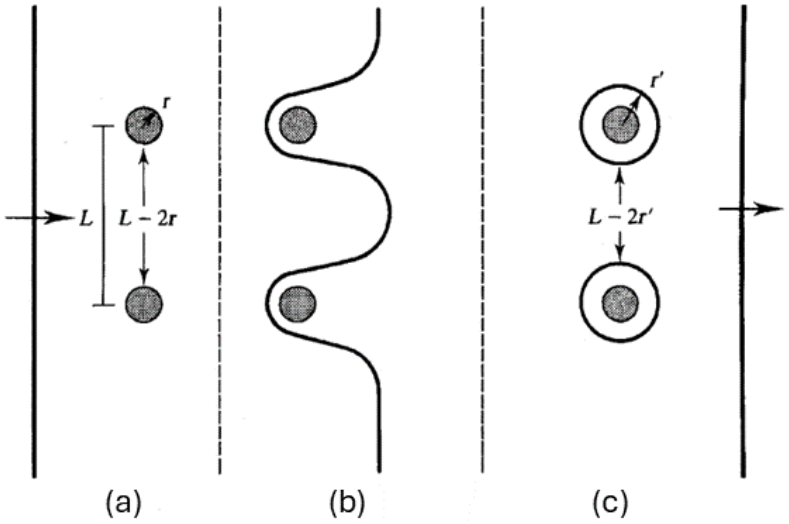

Figure 1.6: Schematic of Orowan looping in its stages: a) dislocation approaches precipitate particles, b) the dislocation bows around the precipitate particles, and c) dislocation forms loops around the precipitate particles as it continues through the matrix lattice. This figure is adapted from [15].

1.3 Mechanical properties

A material's mechanical behavior is governed by microscopic and atomistic interactions. A material's response to an applied force depends on its characteristics and the magnitude of the force. For example, plastic deformation and fracture are macroscale events that manifest due to phenomena that occur at an atomistic scale, corresponding to the severance of atomic bonds and the net movement of many atoms in response to applied stress. It is critical that materials scientists understand the mechanisms that govern a material's behavior under an applied load. This section discusses three types of mechanical properties: hardness, elastic modulus, and creep.

1.3.1 Elastic Modulus

Upon external loading, a material undergoes a shape change, which may be permanent depending on the applied load. Plastic deformation refers to the permanent shape change of a material upon an applied load [15]. Before plastic deformation is achieved, a material will deform elastically, meaning that it will go back to its original shape once the force is removed. Hooke's Law is used to represent a material's elastic behavior in the following equation [15]:

$$(l - l_0) = \delta l - F \tag{1.2}$$

where l_0 is the original sample length, l is the sample length after the force is applied, and F is the applied force. The expression $l - l_0$ represents the amount of extension experienced by a material when a tensile force is applied. The amount of extension depends on the sample's dimensions, and so F is typically normalized by the cross-sectional area of the sample, A. The normalized force is represented by the stress, σ, and the normalized extension is represented by strain, ε [15]. Stress and strain are related through the following equation [15]:

$$E = \frac{\sigma}{\varepsilon} \tag{1.3}$$

where E is the elastic modulus of the material. The relationship expressed in Eqn. 1.3 is represented by the classic stress-strain curve, shown in Fig. 1.7a. The slope of the stress-strain curve before the onset of plastic deformation is represented by E [15]. The elastic modulus E is a representation of a material's stiffness (i.e., the strength of the atomic bonds in a material) and can therefore be interpreted as a measure of the resistance to the severance of the bonds between adjacent atoms, as represented by Fig. 1.7b [2]. The composition, crystallographic structure, and bond type all influence E.

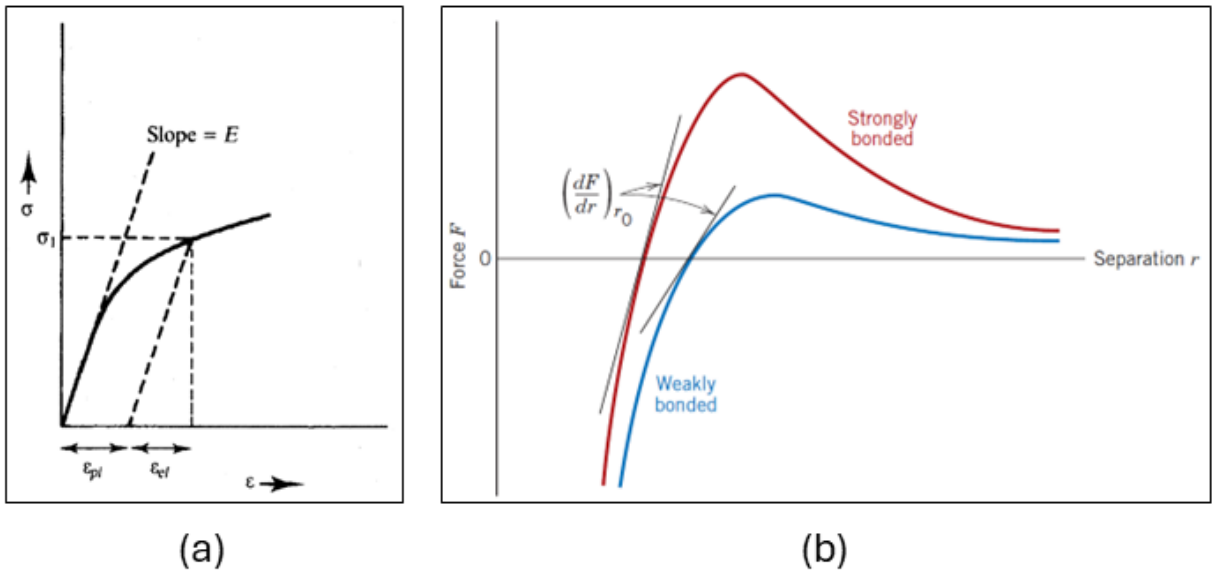

Figure 1.7: a) A schematic of a tensile stress-strain curve [15]. The strain ε is on the x-axis, and the stress σ is on the y-axis. The slope of the curve before the onset of plastic deformation represents the elastic modulus E. b) A graph showing force versus interatomic spacing [2]. The red curve represents strongly bonded atoms, with high E, and the blue curve represents weakly bonded atoms, with low E. The magnitude of E is represented by the slope of the curve at r_0, the equilibrium interatomic spacing.

Although E is typically measured through tensile testing, it can also be measured through methods like nanoindentation. Nanoindentation is an indentation testing method where a controlled mechanical load is applied to a sample surface using an indenter with a specific geometry (e.g., a Berkovich tip, as shown in Fig. 1.8a) [16]. In nanoindentation, small loads on the order of μN are applied with a specified load rate. As the load is applied, the displacement into the sample surface is recorded, generating load-displacement curves as shown in Fig. 1.8b [17].

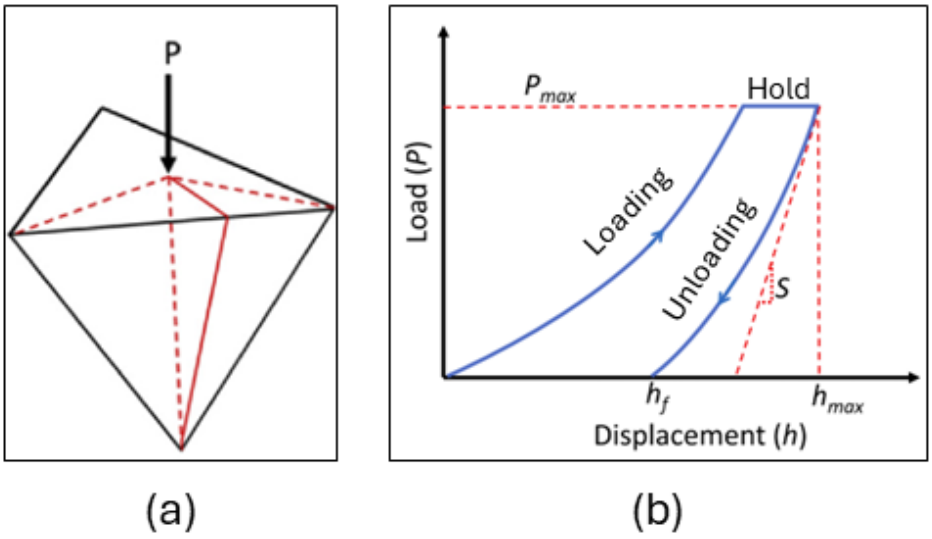

Figure 1.8: Schematics showing a) the geometry for a Berkovich indenter tip [16], and b) a typical load-displacement curve generated during a nanoindentation test [17].

From the load-displacement curve, several mechanical properties can be extracted, such as the stiffness *S*. Stiffness *S* is related to the elastic modulus with the following equation [16]:

$$S = \frac{2}{\sqrt{\pi}} E_r \sqrt{A} \tag{1.4}$$

where E_r is the reduced modulus and A is the indented area at maximum load. The reduced modulus E_r can then be related to the elastic modulus of the sample through the following equation [16]:

$$\frac{1}{E_r} = \frac{1 - {v_s}^2}{E_s} - \frac{1 - {v_i}^2}{E_i} \tag{1.5}$$

where v_s and v_i are the Poisson's ratio of the sample and the indenter, respectively, and E_s and E_i are the elastic moduli of the sample and the indenter, respectively.

1.3.2 Hardness

A material's hardness is essentially its resistance to plastic deformation, usually measured by surface penetration through indentation [1, 15]. Indentation of a material's surface occurs through plastic deformation, so hardness is a function of a material's resistance to plastic flow. Hardness is typically measured through indentation testing, where a load is applied to a material's surface

through a small indenter. There are several types of indentation tests, defined by the shape of the indenter and the applied load. Because these tests can be done at different loads, hardness is not an intrinsic material property, but is a comparative test of resistance to plastic deformation [15].

A common hardness test is Vickers hardness. Vickers hardness testing is quite versatile and can be used to measure the hardness of hard and soft materials. During Vickers hardness testing, a load is applied with a diamond shaped indenter, with applied loads varying from 1 to 120 kg [15]. The material's hardness is derived from the applied load and the corner-to-corner dimensions of the indent on the material's surface and is expressed as a Vickers hardness number (VHN) [15]. Vickers hardness testing is schematically shown in Fig. 1.9.

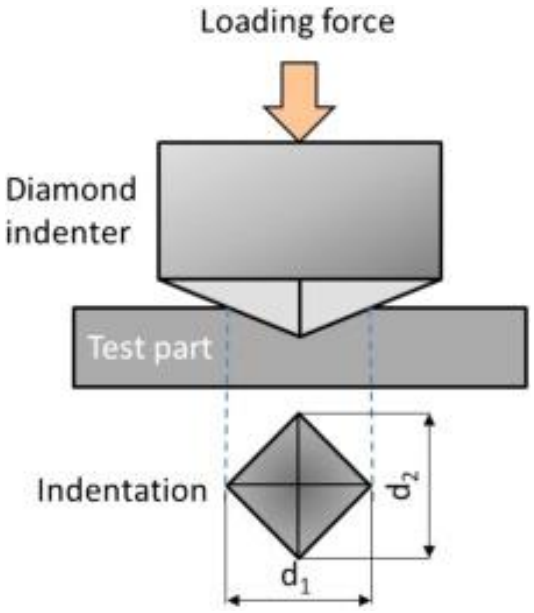

Figure 1.9: A schematic of Vickers hardness testing. A force is applied to a sample's surface with a diamond shaped indenter, leaving a diamond-shaped indent on the surface with corner-to-corner dimensions of d1 and d2 [18].

1.3.3 High-temperature deformation

As technology advances, there is a need for materials to perform at higher temperatures, often in the range of 0.4 – 0.65 T_m (where T_m is the material's absolute melting temperature) [15]. In such a temperature range, a phenomenon known as creep is thermally activated. Creep is a

time-dependent deformation that occurs in both crystalline and non-crystalline materials and occurs at stress levels below the typical yield strength for a material [15]. Creep can be represented schematically in Fig. 1.10.

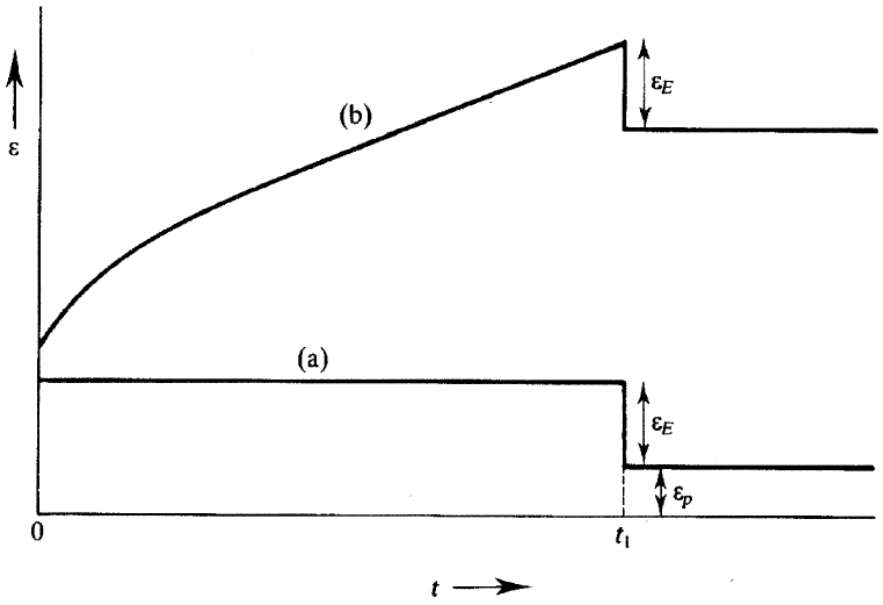

Figure 1.10: Schematic representation of deformation at constant loads, with two conditions: a) time-independent deformation, where elastic strain ε_E is constant from time $t = 0$ to t_1, when the load is removed and only the plastic strain ε_p remains; and b) time-dependent deformation (creep), where strain continuously increases as a load is applied at $t = 0$, and only the initial ε_E is recovered after the load is removed at t_1 [15].

Creep typically occurs at temperatures where solid-state diffusion is thermally activated. There are several mechanisms by which creep can occur, including diffusional-flow mechanisms, grain boundary mechanisms, dislocation climb, and dislocation glide. The mechanism typically varies as a function of temperature and applied load. Creep tests are typically performed by applying a constant load or stress at constant temperature over long time periods, and can be used to determine a material's creep strain rate (i.e., the rate at which a material deforms under a constant load over time), the mechanisms for creep (i.e., the roles which diffusion, grain boundaries, and dislocations play in deformation), and the activation energy for creep [1].

1.4 Overview of dissertation

As new materials and manufacturing techniques are developed to suit the needs of several key industries, creative methods of tailoring microstructure to control mechanical behavior must be explored. Additionally, the underlying mechanisms that dictate such control must be well understood. To this end, this dissertation includes three distinct investigations:

I. To determine the underlying mechanisms that control the microstructure of samples fabricated with ultrasonic vibration-assisted directed energy deposition;

II. To explore the role of phase state and composition on the room-temperature mechanical behavior of entropy stabilized oxides; and

III. To explore the role of microstructure and phase state on the high-temperature deformation of entropy stabilized oxides.

The following sections provide brief overviews of these three experimental studies.

1.4.1 Melt pool evolution in ultrasonic vibration-assisted directed energy deposition

The presence of defects, such as pores, in materials processed using AM represents a challenge during the manufacturing of many engineering components. Recently, ultrasonic vibration-assisted (UV-A DED) has been shown to reduce porosity, promote grain refinement, and enhance mechanical performance in metal components. Whereas it is evident that the formation of such microstructural features is affected by the melt pool behavior, the specific mechanisms by which ultrasonic vibration (UV) influences the melt pool remain elusive. In the present investigation, UV was applied *in situ* to DED of 316L stainless steel single tracks and bulk parts. For the first time, high-speed video imaging and thermal imaging were implemented *in situ* to quantitatively correlate the application of UV to melt pool evolution in DED. Extensive imaging data were coupled with in-depth microstructural characterization to develop a statistically robust dataset

describing the observed phenomena. Our findings show that UV increases the melt pool peak temperature and dimensions, while improving the wettability of injected powder particles with the melt pool surface and reducing powder particle residence time. Near the substrate, we observe that UV results in a 92% decrease in porosity, and a 54% decrease in dendritic arm spacing. The effect of UV on the melt pool is caused by the combined mechanisms of acoustic cavitation, ultrasound absorption, and acoustic streaming. Through *in situ* imaging we demonstrate quantitatively that these phenomena, acting simultaneously, effectively diminish with increasing build height and size due to acoustic attenuation, consequently decreasing the positive effect of implementing UV-A DED. Thus, this research provides valuable insight into the value of *in situ* imaging, as well as the effects of UV on DED melt pool dynamics, the stochastic interactions between the melt pool and incoming powder particles, and the limitations of build geometry on the UV-A DED technique.

1.4.2 Room-temperature mechanical properties of multiphase entropy stabilized oxides

There have been limited investigations into the mechanical behavior of entropy stabilized oxides (ESOs), which display a reversible, entropic phase transformation leading to the formation of secondary phases. To fill this gap in the literature, we investigate the influence of these secondary phases on the mechanical behavior of the (CoCuMgNiZn)O transition metal ESO (TM-ESO). TM-ESOs of equimolar, Co-deficient, and Cu-deficient compositions were fabricated, heat treated to form secondary phases, and characterized. Room-temperature indentation was used to measure the hardness and elastic modulus of as-sintered and multiphase bulk samples. Hardness values ranged from 3700 to 6400 MPa, and elastic modulus values ranged from 140 to 170 GPa. As the atomic fraction of secondary phase increases, equimolar and Co-deficient TM-ESO harden then soften, and Cu-deficient TM-ESO continuously hardens. Hardness trends were analyzed by evaluating strengthening mechanisms, indicating that hardness is significantly influenced by the

interactions between dislocations and secondary phases. The elastic modulus varies as a function of composition and quantity of secondary phases but falls within a range of values predicted by a composite model, indicating that TM-ESO behaves similarly to conventional composite materials. Changing composition influences the hardness and elastic modulus of as-sintered TM-ESOs due to changes in cation-dislocation and cation-cation interaction energies. Overall, our findings indicate that the room-temperature mechanical behavior of as-sintered and multiphase TM-ESOs is influenced by solid-solution and precipitation strengthening mechanisms, respectively, due to significant dislocation activity, and that the entropic phase transformation can be manipulated to tailor the mechanical properties.

1.4.3 High-temperature deformation of entropy stabilized oxides

There have been limited investigations into the room-temperature mechanical behavior of TM-ESO. In this investigation, we begin to address the high-temperature deformation behavior of TM-ESOs. The microstructure and phase state of TM-ESOs were varied. TM-ESOs with grain sizes of 1 μm (fine-grained) and 20 μm (coarse-grained) were deformed at high temperatures in their single phase and multiphase states. They were deformed at loads of 13 N, 20 N, and 31 N, and at temperatures ranging from 600 °C to 850 °C in 50 °C increments. From these deformation experiments, stress-strain curves were generated from which stress exponents were extracted. The stress exponents for all samples indicate that they were deforming superplastically. The fine-grained samples had stress exponents ranging from 0.1 – 0.4, and the secondary phases did not have a significant effect on the stress exponents. The coarse-grained samples had higher stress exponents until 700 °C, ranging from 0.5 – 1.9. The coarse-grained, multiphase samples generally had higher stress exponents (0.7 – 1.9) than the coarse-grained, single-phase samples (0.5 – 0.7), likely due to grain boundary pinning by the secondary phase particles. For all single-phase and

multiphase coarse-grained samples, the stress exponent drops and becomes similar to those measured for the fine-grained samples deformed at 750 °C. The drop in stress exponent for the coarse-grained samples at higher temperatures indicates a temperature-induced switch in the deformation mechanism from grain boundary sliding to solute-drag creep. Overall, this work demonstrates that microstructure and phase composition of TM-ESO can be used to tailor the high-temperature deformation of TM-ESO.

Chapter 2: *In situ* observation of melt pool evolution in ultrasonic vibration-assisted directed energy deposition

2.1 Background

In casting and other conventional metallurgy processes, dynamic solidification has been utilized to suppress formation of defects and promote nucleation of finer crystals, leading to enhanced mechanical behavior [19]. Dynamic solidification involves forced motion of molten metal ahead of the solidification front, through means such as vibration and electromechanical stirring. Such techniques have been used in metallurgy as early as the 1800s, notably by renowned metallurgist Dmitry Chernov, who reported that vigorously shaking a mold of solidifying steel resulted in a fine crystal structure [19]. Continuing this trend, in recent decades, ultrasonic vibration (UV) has been widely used to assist in casting and welding of metals [20–26]. Ultrasonic waves propagate through solid, liquid, and gas media at frequencies of at least 20 kHz [27]. Due to the nonlinear interactions of ultrasonic waves with molten metal, UV-assisted (UV-A) processing of metals typically leads to fewer defects and finer microstructures, resulting in enhanced mechanical properties [20–26].

Over the last several years, metal additive manufacturing (AM) has gained popularity as a novel molten metal processing technique, with the development of several laser-based techniques such as directed energy deposition (DED) [28, 29]. In DED, a laser creates a melt pool on the surface of a metal substrate, into which metal powders are delivered through a stream of inert gas. The laser incrementally moves up in the z-direction, and either the substrate or the laser raster in the x-y plane. In this fashion, parts are deposited layer-by-layer based on a computer-aided design (CAD) model. DED offers several advantages and capabilities over other conventional and AM techniques, like rapid production time, product repair and performance enhancement, and production of multi-material parts [28, 29].

Analysis of structure-property relationships and optimization of deposition parameters have been carried out for several engineering alloys fabricated via DED, such as Ti-6Al-4V [30, 31], austenitic stainless steels such as AISI 316L [32, 33] and 304L [34, 35], AlSi10Mg [36, 37], and nickel-based superalloys such as Inconel 718 [38, 39] and Inconel 625 [40–42]. These alloys are commonly found in components used in the energy, automotive, and aerospace industries. AISI 316L stainless steel, in particular, is widely used in DED due to its high corrosion resistance and ductility, and low susceptibility to the formation of chromium-rich carbide phases [43–45]. However, DED-fabricated parts are prone to the formation of defects, such as porosity and hot cracking, and irregular microstructures [46–49]. Additionally, due to the presence of extreme temperature gradients within the melt pool, and the stochastic nature of the interactions between the melt pool, laser beam, and powder, DED-fabricated components have a propensity for the formation of and consequential deformation by residual stresses [50, 51]. Therefore, an understanding of melt pool dynamics is critical to improve the performance of DED-fabricated parts.

Recently, several studies have confirmed the feasibility of UV-A DED. The microstructures, defects, and mechanical properties of several alloys deposited with UV-A DED have been characterized. For example, Cong and Ning observed an increase in melt pool dimensions, yield strength, ultimate tensile strength (UTS), microhardness, and ductility, and a decrease in porosity in UV-A DED AISI 630 stainless steel single track thin walls [52]. Ning *et al*. studied the effects of UV on the phase composition, defects, mechanical properties, and melt pool evolution of UV-A DED Inconel 718 parts. They reported a reduction of Laves phases, which are detrimental to the mechanical properties of the Inconel 718 alloy [53]. Additionally, Ning *et al*. reported a decrease in porosity, and an increase in yield strength, ductility, UTS, and microhardness for Inconel 718

[54]. By using an infrared (IR) camera to analyze the melt pool *in situ* during the deposition of 4-layer components, Ning *et al*. demonstrated that UV increases the melt pool temperature and dimensions, and that these changes are amplified at higher frequencies [55]. Todaro *et al*. reported a transition from columnar grains to fine, equiaxed crystals, and an increase in yield strength and tensile strength for UV-A DED-fabricated Ti-6Al-4V bulk parts [56]. Todaro *et al.* also reported a transition from columnar grains to fine, equiaxed crystals of random orientation and a higher density of grains despite a decrease in cooling rate in UV-A DED-fabricated 316L stainless steel parts [57]. These studies show that UV-A DED results in finer microstructures, fewer defects, and improved mechanical properties. These findings are consistent with what is typically observed in conventional UV-A metallurgy processes, and is promising for the future of metal AM. However, little is understood about how UV affects melt pool evolution particularly as the build dimensions increase, which is essential for scaling up the use of UV-A DED to produce components with large or complex geometries.

The current investigation aims to develop an understanding of how the melt pool temperature, geometry, and interactions with powder are impacted during UV-A DED, and more particularly, how these effects evolve with increasing build size. In this study, 316L stainless steel single tracks and cubes were deposited with and without UV by a proprietary DED technology called Laser Engineered Net Shaping® (LENS®). For the first time, high-speed and thermal imaging were used *in situ* to visualize the melt pool surface during UV-A LENS® deposition to track UV effects in large builds. Moreover, these techniques provide an extensive and quantitative dataset to measure key melt pool characteristics and thereby correlate them with observed effects of UV on microstructure and build quality. Post-deposition characterization of defects and microstructures in as-built samples was carried out with optical microscopy, scanning electron microscopy (SEM),

and electron backscatter diffraction (EBSD). We demonstrate a statistically significant correlation between the application of UV and peak melt pool temperature, melt pool size, and particle residence time. Effects on peak melt pool temperature and melt pool size diminish with increasing build size. We further consider the physical mechanisms by which the UV interacts with the melt pool and the build to provide an explanation of the observed behavior. Overall, this study highlights the power of *in situ* imaging to quantitatively characterize the UV-A DED process, as well as the limitations that must be considered for future development of UV-A DED when applied to large and/or complex parts.

2.2 Experimental methods

2.2.1 Sample fabrication & *in situ* experimentation

Samples were deposited in an Optomec LENS® 750 workstation (Optomec, Albuquerque, NM, USA) with and without UV. Gas atomized 316L stainless steel (SLM Solutions, Lübeck, Germany) was used as feedstock powder. The particles were size between 25 – 150 μm in size. The chemical composition of the powder, as provided by the manufacturer, is shown below in Table 2.1.

Table 2.1: Chemical composition (weight %) of 316L stainless steel feedstock powder, as provided by the manufacturer.

Fe	Cr	Ni	Mo	Mn	Si	P	S	C	N
Balance	16.00-18.00	10.00-14.00	2.00-3.00	2.00	1.00	0.045	0.030	0.030	0.10

The samples were deposited onto a 316L stainless steel substrate (McMaster Carr, Elmhurst, IL, USA), with a length and width of 150 mm, and a thickness of 6 mm. A piezoelectric ultrasonic transducer (Beijing Ultrasonic, Beijing, China) was coupled to the bottom-center of the substrate using a high-temperature resistant epoxy (JB Weld, Sulphur Springs, TX, USA), as shown in Fig. 2.1. A dampener (Grainger, Los Angeles, CA, USA) was placed beneath the transducer to

prevent damage to the build plate. The assembly was fastened to the LENS® build plate. The transducer was set to an ultrasonic frequency of 33 kHz and an ultrasonic amplitude of 5 µm.

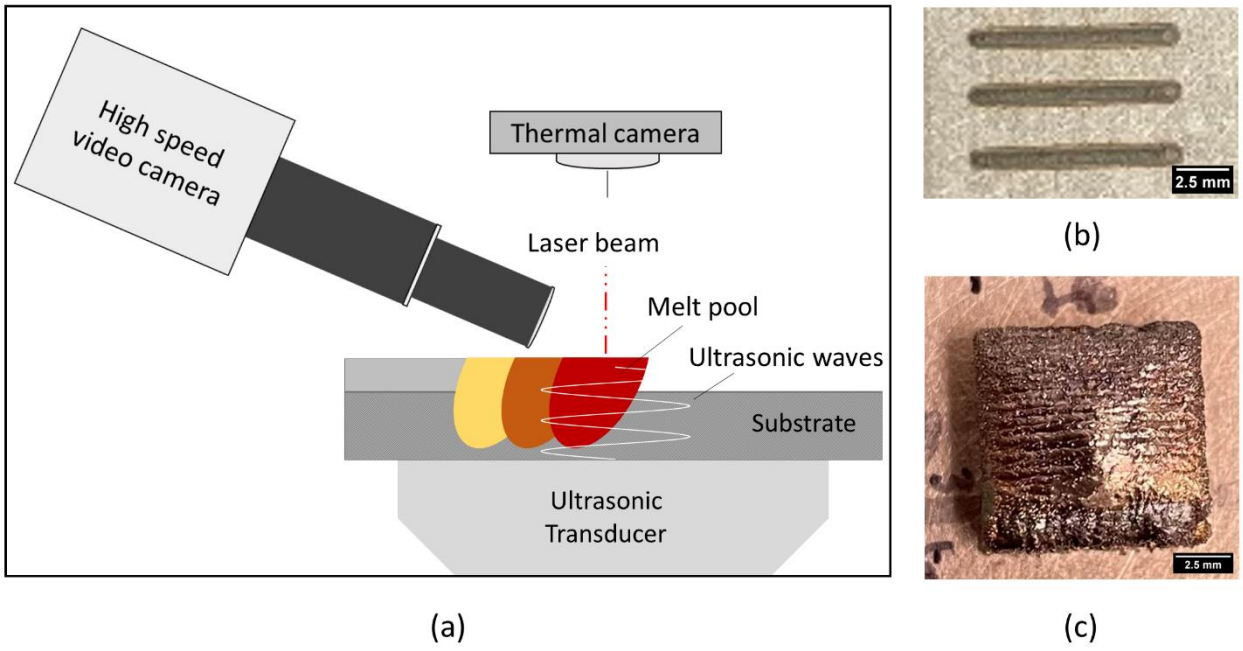

Figure 2.1: Experimental overview showing: a) The experimental set up (not to scale). The ultrasonic transducer is coupled to the bottom of a 316L stainless steel substrate, sending vibration up into the melt pool during deposition. A high-speed video camera films from the side, and a thermal camera films from above; b) As-deposited single tracks; and c) As-deposited cubic sample.

Single tracks were created under an ambient atmosphere. Single tracks were 10 mm long and 1 mm wide. All samples were deposited with a laser power of 390 W, a layer thickness of 0.2 mm, a scan speed of 16.9 mm/s, a hatch spacing of 0.5 mm, and a volumetric energy density (VED) of 228 J/mm^3. The beam diameter is estimated to be 0.84 mm based on previous studies using the same instrumental setup[58]. Volumetric energy density (VED), E_v, was calculated with the following equation [59]:

$$E_v = \frac{P}{v \cdot t \cdot h} \tag{2.1}$$

where P is laser power, v is laser scan speed, t is layer thickness, and h is hatch spacing. The powder feed rate was 22 g/min for single tracks, and 27.5 g/min for cubic samples.

2.2.2 *In situ* analysis

A thermal imaging camera and a high-speed video camera were used *in situ*, as shown in Fig. 2.1, to image the evolution in melt pool temperature and geometry, and the interactions between the melt pool and injected powder particles, respectively, allowing for the collection of detailed, quantitative data on peak melt pool temperature, melt pool geometry and size, and particle residence time for both deposition conditions – with and without UV. Based on these data and additional post-deposition microstructural characterization on grain size and morphology, melt pool depth, dendrite arm spacing, and porosity, the mechanisms governing UV interactions with the melt pool are described below.

A FASTCAM SA-Z 2100K M4 high-speed video camera (Photron USA, Inc., San Diego, CA, USA) was used to record the experiments at a frame rate of 30,000 frames per second. Cubic samples (40-layer, 10 mm x 10 mm) were deposited under an inert argon atmosphere with oxygen maintained at <100 ppm. A charged couple device (CCD) thermal imaging camera was used to capture melt pool thermal profiles at 500 frames per second, from a top-down view of the x-y plane, for all depositions. For the cubes, thermal imaging data were captured every 10 layers, starting at the 5^{th} layer.

High-speed video camera footage of single track depositions was viewed and analyzed with the Photron FASTCAM Viewer 4 software [60]. Analysis of 100 particles that collided and submerged near the center of the melt pool was done for both non-UV-A and UV-A conditions. Particle residence time was calculated by measuring the amount of time between a particle's collision with the melt pool surface, and its submersion into the melt pool. The thermal imaging camera data for the single track and cube depositions were analyzed using Python [61]. A script was written to

conduct statistical analysis on the melt pools' average maximum temperature and surface area. Thermal contour maps and profiles of melt pool surfaces were generated accordingly.

2.2.3 Defect and microstructural characterization

The as-built 316L stainless steel cubes were removed from the substrate and cross-sectioned with a FA20S electrical discharge machine (Mitsubishi, Tokyo, Japan). The samples were hot-mounted in a KonductoMet® conductive mounting compound (Buehler, Lake Bluff, IL, USA), and polished to a 0.05 μm finish using a RotoPol-22 polisher (Struers, Copenhagen, Denmark).

SEM of porosity and microstructures was performed using a field emission (FE) Magellan 400 XHR microscope (FEI, Hillsboro, OR, USA) with an accelerating voltage of 20 kV. Quantitative analysis of images was done using ImageJ software [62]. Statistical analysis of porosity was done by collecting 50 images per non-UV-A and UV-A conditions. Color thresholding was used on porosity to calculate the total percent of the image area attributed to porosity. EBSD was carried out in the FE-SEM equipped with EBSD-symmetry detectors (Oxford Instruments, Abingdon, United Kingdom), with a step size of 1 μm. Oxford AZtec software was used for EBSD data processing and microstructural analysis [63].

The cross-sectioned cubic samples were etched in a solution of HCl and HNO_3 in a 3:1 ratio for 30 seconds. They were immediately rinsed in a cold-water bath to prevent the etchant from reacting further with the sample surfaces. Images of melt pool boundaries were taken with a BX53M optical microscope (Olympus, Tokyo, Japan) at the bottom (nearest the substrate), center, and top of the samples. Melt pool boundaries were traced digitally. Cellular dendritic structures were imaged with SEM. Using ImageJ, melt pool depth and dendritic arm spacing were measured from the optical and SEM micrographs, respectively. Dendritic arm spacing was measured with an

area counting method [64]. Statistical analysis was done on 100 measurements per non-UV-A and UV-A condition. Two-sample t-tests were done in the software R [65].

2.3 Results

2.3.1 Thermal imaging results

Representative melt pool temperature profiles and thermal contour plots, derived from a single frame captured by the thermal imaging camera, for both non-UV-A and UV-A single tracks are shown in Fig. 2.2. The temperature profile for the UV-A single track is wider and taller than the non-UV-A single track, indicating a larger melt pool with a higher peak temperature when UV is applied during DED.

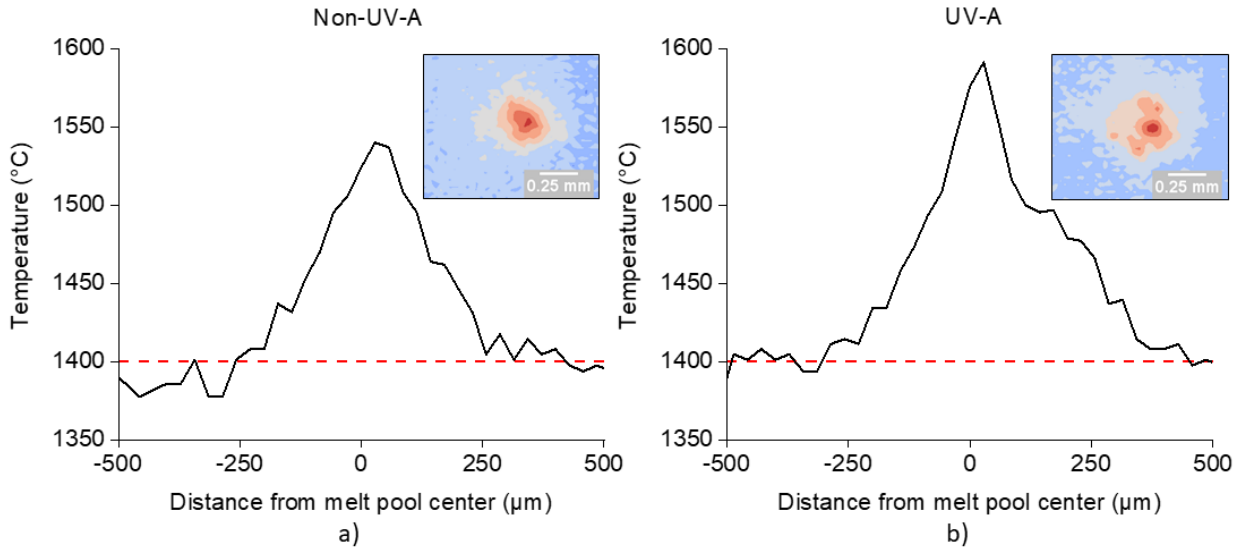

Figure 2.2: Representative single-track temperature profiles derived from thermal imaging camera contour plots: a) non-UV-A condition, with a narrower, shorter profile, and b) UV-A condition, with a wider, taller profile. The red, dashed lines denote the melting temperature of 316L stainless steel, approximately 1400 °C *[43]*. The insets show the corresponding thermal contour plot of the melt pools as determined by thermal imaging.

Average maximum melt pool temperature and average melt pool surface area were calculated from approximately 700 frames for both non-UV-A and UV-A single tracks. For the non-UV-A single track melt pools, the average maximum temperature was 1550 ± 50 °C, and the average surface area was 0.02 ± 0.02 mm^2 (uncertainty values expressed here and elsewhere in this chapter

are standard deviation values). For the UV-A single track melt pools, the average maximum temperature was 1640 ± 90 °C, and the average surface area was 0.05 ± 0.04 mm^2.

The thermal imaging camera was also used to measure the melt pool temperature profile while depositing the DED cubic samples. Results derived from these images for both non-UV-A and UV-A DED conditions are shown in Fig. 2.3. 800 frames were collected at layers 5, 15, 25, and 35 for both non-UV-A and UV-A conditions to estimate how the average peak melt pool temperature and average melt pool surface area evolve with increasing build size. Error bars were calculated from standard deviation values calculated from the 800 collected frames at each layer. The non-UV-A average maximum temperature and average melt pool area consistently increase until they reach an equilibrium state by layer 25. Under the UV-A condition, the average maximum temperature and average melt pool area values are larger at layer 5 but reach a steady state earlier, by layer 15. Statistical analysis shows that the differences in average maximum melt pool temperature and average melt pool surface area were statistically significant between the non-UV-A and UV-A conditions ($p < 1.0 \times 10^{-15}$ for most cases).

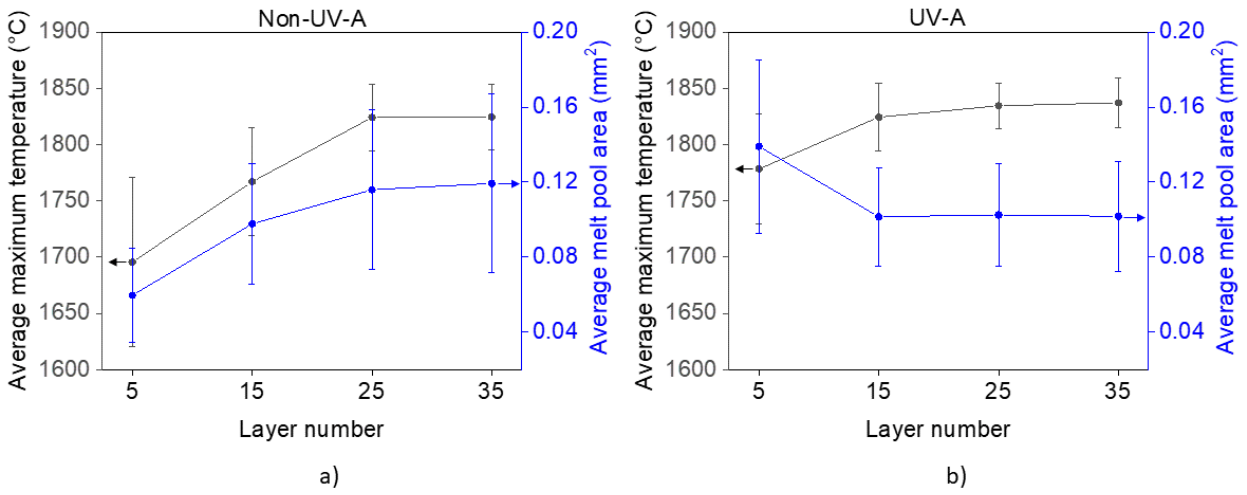

Figure 2.3: Melt pool peak temperatures and dimensions for DED 316L stainless steel cubic samples, as determined from thermal imaging contours. Values for the average maximum temperature and average melt pool area at the 5th, 15th, 25th, and 35th layers are presented for: a) non-UV-A, and b) UV-A conditions. The arrows indicate which axis each dataset corresponds to.

2.3.2 High-speed video results

Representative snapshots from particle collision with the melt pool surface to submersion into the melt pool, and the results for average particle residence time are shown in Fig. 2.4. Shown in Fig. 2.4 are representative snapshots of particle collisions with the melt pool surface (Fig. 2.4a), particle residence on the melt pool surface (Fig. 2.4b), the onset of particle submersion into the melt pool (Fig. 2.4c), and complete particle submersion into the melt pool (Fig. 2.4d). The values for the average particle residence time, calculated from 100 particles for both non-UV-A and UV-A depositions, were 1.3 ± 0.32 ms and 0.7 ± 0.8 ms for the non-UV-A and UV-A deposits, respectively. The difference in particle residence time was shown to be statistically significant

between the two conditions ($p < 1.0 \times 10^{-7}$), demonstrating that UV can effectively decrease particle residence time during DED, suggesting that the melt pool's particle capture rate increases.

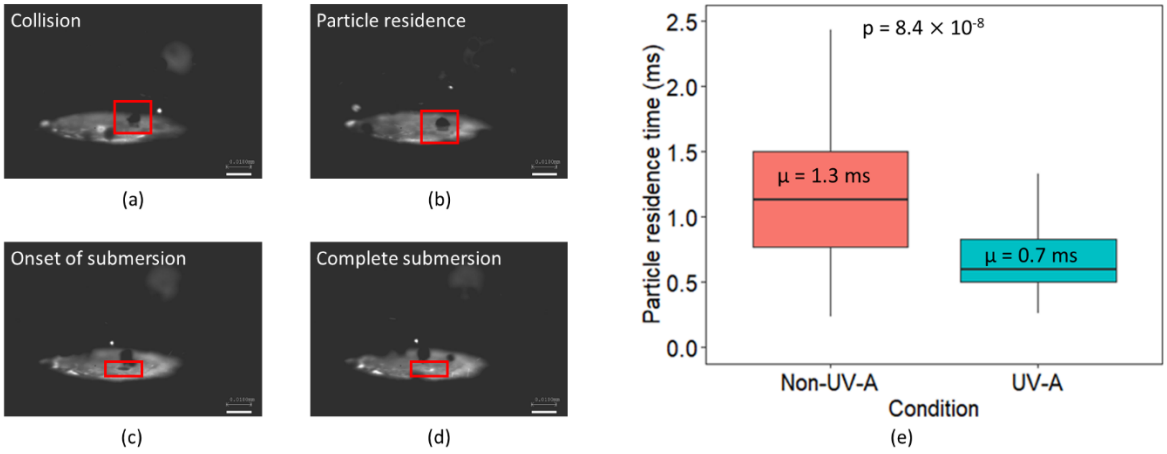

Figure 2.4: Representative images of a) particle collision with melt pool surface, b) particle residence on melt pool surface, c) onset of particle submersion into melt pool, d) particle submersion into the melt pool; and e) particle residence time on the melt pool surface, measured using high-speed video imaging, for non-UV-A and UV-A conditions. The difference in particle residence time between the two conditions is statistically significant ($p < 1.0 \times 10^{-7}$).

2.3.3 As-built microstructures and defects

Measured values for melt pool depth are summarized in Table 2.2. The difference in melt pool depth between non-UV-A and UV-A conditions for regions near the substrate was shown to be statistically significant ($p < 1.0 \times 10^{3}$). However, the difference in melt pool depth near the center and top was not statistically significant between the two conditions ($p > 0.5$).

Table 2.2: Comparison of non-UV-A and UV-A melt pool depth for the as-deposited 316L stainless steel cubic samples.

Location	**Non-UV-A melt pool depth (μm)**	**UV-A melt pool depth (μm)**	**p-value**
Near substrate	190 ± 16	235 ± 16	4.1×10^{-4}
Center	215 ± 35	215 ± 28	0.96
Top	220 ± 33	200 ± 33	0.38

Fig. 2.5 shows EBSD analysis of microstructures of the cubes in the region near the substrate. As shown in Fig. 2.5a, the grains in the non-UV-A sample are columnar and tilted in the direction that the melt pool travels during deposition. Fig. 2.5b shows finer, equiaxed grains located near

the substrate, and a transition to a larger, columnar structure in the UV-A sample. SEM was used to collect images of cellular dendritic structures, and 100 data points per non-UV-A and UV-A conditions were used for statistical analysis. The insets in Fig. 2.5 show that the cellular dendrites are larger in the non-UV-A DED cubic samples than in the UV-A DED cubic samples, with average arm spacings of 2.9 ± 0.5 µm and 1.3 ± 0.3 µm, respectively. Statistical analysis indicates that the difference in average dendritic arm spacing between the non-UV-A and UV-A conditions was statistically significant ($p < 1.0 \times 10^{-15}$).

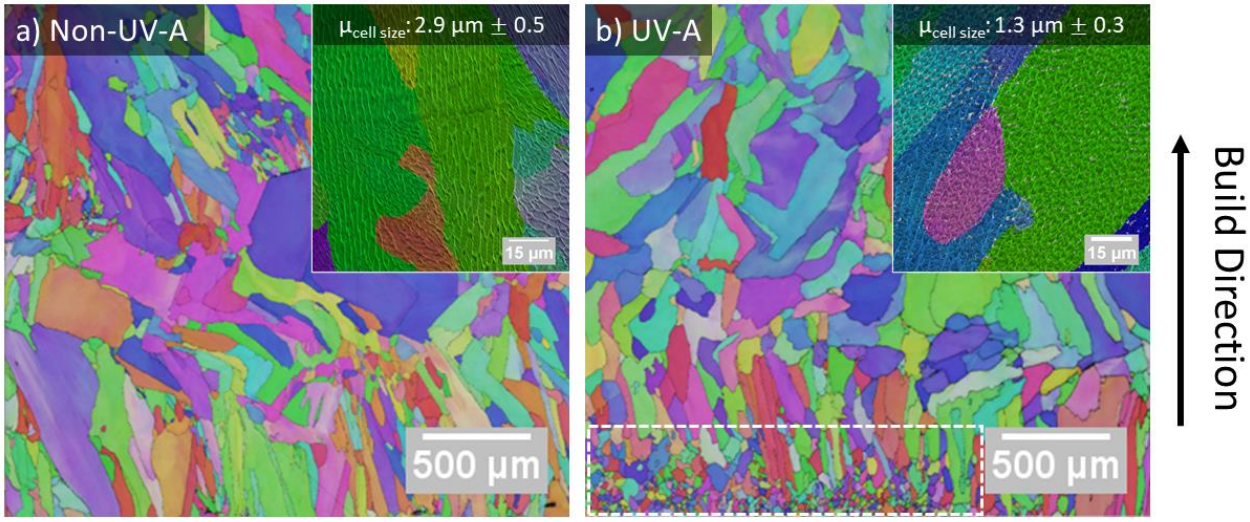

Figure 2.5: Microstructure analysis: Representative EBSD inverse pole figures of the as-deposited 316L stainless steel cubic samples near the substrate, for: a) a non-UV-A sample, and b) a UV-A sample. The insets show cellular dendrites in the non-UV-A and UV-A samples, respectively. The white, dashed box in (b) highlights the fine, equiaxed grains located in the first few layers of deposition.

SEM was used to view and quantify the porosity in cubic samples, shown in Fig. 2.6. For statistical analysis of porosity, 50 data points were collected per non-UV-A and UV-A conditions. The non-UV-A DED cubes demonstrated large, distinct lack-of-fusion pores and small, scattered gas pores, shown in Fig. 2.6a. The average percentage of porosity for the non-UV-A condition was 0.24 % ± 0.35 %. The UV-A DED cube displayed smaller, more scattered gas pores, shown in the inset in Fig. 2.6b. Fine pores, on the order of ~150 nm in diameter, were observed at higher magnifications in the UV-A DED cube. These fine pores were concentrated at grain and cellular

dendrite boundaries and were not observed in the non-UV-A samples. The average percentage of porosity for the UV-A condition was 0.02 % ± 0.02 %. The difference in the average percentage of porosity between the two conditions was statistically significant ($p < 1.0 \times 10^{-4}$).

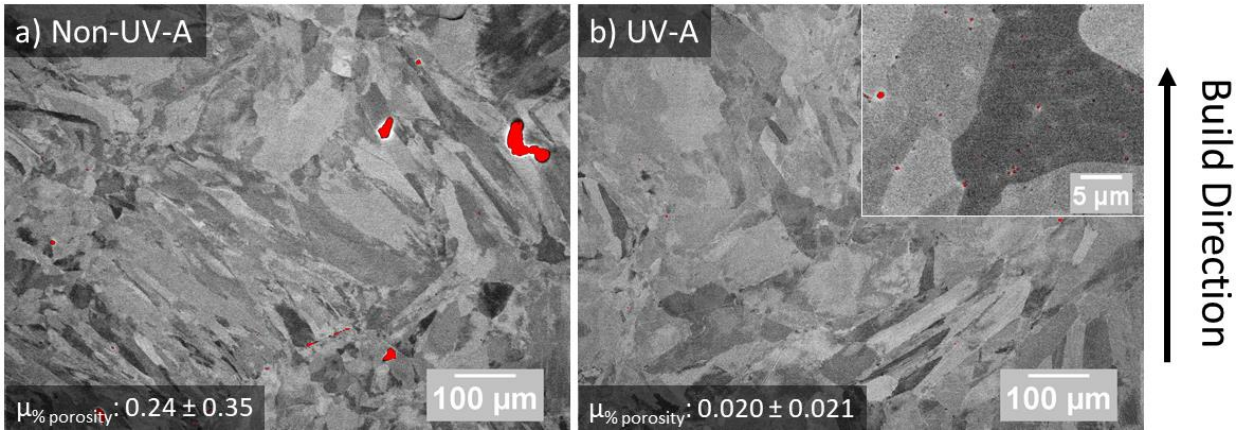

Figure 2.6: Porosity mapping: A comparison of porosity (highlighted in red) between: a) non-UV-A and b) UV-A as-deposited 316L stainless steel cubic samples. The inset in (b) shows evidence of gas porosity, i.e., small gas pores concentrated at grain boundaries.

2.4 Discussion

2.4.1 UV-induced phenomena within the melt pool

In UV-A treatment of molten metal, three phenomena have been reported to occur (Fig. 2.7), which are proposed to contribute to the distribution of excess heat within the melt pool observed in the present investigation (see Fig. 2.2). The first is acoustic cavitation, which is the rapid formation and collapse of gas voids [66]. As vibrational waves propagate through the melt, they form regions of high and low pressure. In the low-pressure regions, voids form and fill with gaseous species saturated in the surrounding melt. The bubbles then collapse. During the collapsing process, the liquid-gas interface implodes and builds inwards inertia, increasing the pressure and temperature within the bubble. Once the bubble collapses, the gaseous species are violently reincorporated into the surrounding liquid, carrying the generated heat with them. The second phenomenon is ultrasound absorption, which occurs as waves impart energy onto the

molecules in the fluid as they pass through [67]. The transfer of energy results in deformation of the fluid during periodic compression and rarefaction. Viscous dissipation occurs, resulting in the transformation of kinetic energy into heat, which is then transmitted through the melt pool, raising its temperature [68]. The last phenomenon is acoustic streaming [27, 69]. As a fluid interacts with acoustic oscillations, a transfer of momentum to the fluid occurs, resulting in steady fluid flow. The resulting fluid flow carries the higher-temperature liquid from the center of the melt pool to its outer edges, thereby improving heat transfer and stabilizing the temperature distribution in the melt pool. The three combined phenomena consequentially result in the observed increase in melt pool temperature and dimensions, as observed in Fig. 2.2.

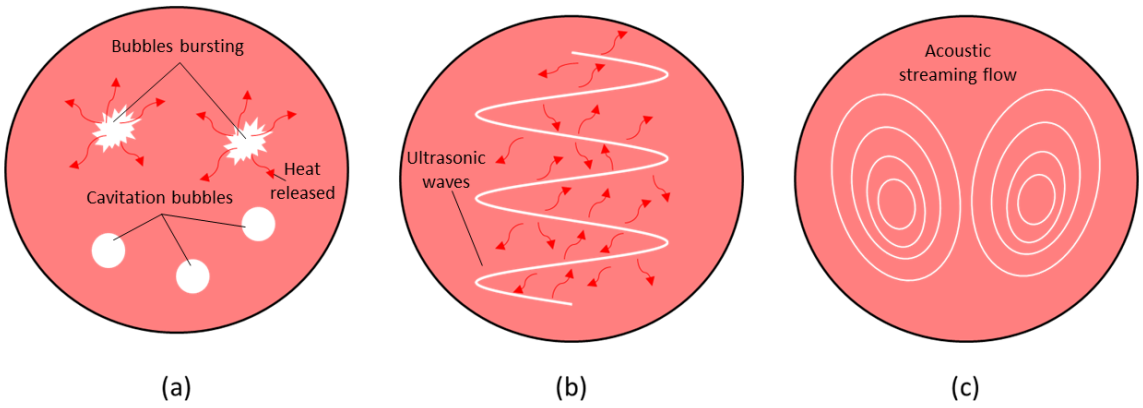

Figure 2.7: Schematic representations of the three UV-induced phenomena: a) acoustic cavitation (i.e., the formation and collapse of cavitation bubbles that release heat into the melt pool), b) ultrasound absorption (i.e., the dissipation of vibrational energy as heat into the melt pool), and c) acoustic streaming (i.e., steady flow in the melt pool).

We propose that combined acoustic cavitation, ultrasound absorption, and acoustic streaming have a direct impact on melt pool evolution during deposition, as observed from the *in situ* single-track results presented in Fig. 2.2. The generation and transmission of heat from acoustic cavitation and ultrasound absorption contribute to the higher overall melt pool temperature of UV-A samples (Fig. 2.2). Furthermore, acoustic streaming and Marangoni flow drive the hotter regions of the molten metal towards areas of high surface tension (in this case, the melt pool

boundaries) [70]. Thus, the solid liquid boundaries grow, and the melt pool dimensions increase (see Fig. 2.2).

2.4.2 Effect of UV on particle interactions with melt pool

The effects of UV on the melt pool temperature (see Figs. 2.2 and 2.3) influence the particle interactions with the melt pool surface. The particle residence time decreased by approximately 50% with UV, as shown in Fig. 2.4. The temperature-dependence of a fluid's surface tension is expressed by the Eötvös rule [71]:

$$\gamma_{lv} V^{\frac{2}{3}} = k(T_C - T) \tag{2.2}$$

where γ_{lv} is the melt pool surface tension, V is the molar volume of the melt, k is a constant, T_C is the critical temperature at which surface tension is 0, and T is the melt pool temperature. As the melt pool temperature increases, γ_{lv} decreases. The decrease in γ_{lv} impacts the contact angle, as demonstrated by Young's equation [72]:

$$\cos\theta = \frac{\gamma_{sv} - \gamma_{sl}}{\gamma_{lv}} \tag{2.3}$$

where θ is the contact angle between the particle and the melt pool surface, γ_{sv} is the particle surface energy, and γ_{sl} is the interfacial energy between the particle and the melt pool surface. As the γ_{lv} decreases, θ decreases. Additionally, due to the increase in melt pool temperature, γ_{sl} decreases, which also contributes to a decrease in θ [73]. Smaller values of θ indicate improved wettability of injected particles with the melt pool surface. Previous modeling by Haley *et al*. has shown that the particle residence time is shorter at smaller values of θ. Haley *et al*. also derived the temperature dependence of the particle residence time [74]:

$$t_{melt} = \frac{1}{4\pi\alpha}\left(\frac{8}{3}\pi {r_p}^3 \frac{T_{0,pool} - T_{0,part}}{T_{0,pool} - T_m}\right)^{2/3} \tag{2.4}$$

where t_{melt} is particle residence time, α is the thermal diffusivity, r_p is the particle radius, $T_{0,pool}$ and $T_{0,part}$ are the initial temperatures of the melt pool and particle respectively, and T_m is the melting temperature of the metal. According to the relationship in Eqn. 2.5, as the melt pool temperature increases, the particle residence time decreases. This relationship is consistent with present findings, shown in Figs. 2.2 and 2.4.

Historically, users have implemented a variety of techniques to improve powder particle wettability during DED processes, such as the addition of surface active elements [75–77], powder surface treatments [78], and powder coatings [79]. In this study, UV is shown to improve the wettability of injected particles with the melt pool surface without prior powder treatment, as indicated by the decrease in particle residence time noted in Fig. 2.4b. Ultimately, UV-A DED may allow users to bypass such techniques to improve wettability.

2.4.3 Ultrasonic attenuation with increasing wave propagation distance

In standard non-UV-A DED, the substrate onto which parts are deposited acts as a heat sink, leading to higher cooling rates within the bottom layers nearest the substrate. At higher layers, the substrate's heat sink effects dissipate and heat accumulates, causing the melt pool to become hotter and larger [80]. The melt pool temperature and dimensions eventually reach a steady state and remain constant with increasing build height [8]. In the UV-A DED cubes, the melt pool reaches this steady state earlier than in the non-UV-A cubes, as indicated by the changes in average maximum melt pool temperature and average melt pool area (see Fig. 2.3). This observed behavior suggests that there is a threshold height by which, for the current configuration, the UV intensity is no longer large enough to activate the key phenomena discussed above that impart thermal energy to the melt pool. By the 25th and 35th layers, the heating effects caused by UV are negligible compared to the heat accumulation that is intrinsic to DED, as shown by the steady-state values

for maximum average temperature and average melt pool surface area (Fig. 2.3), which are comparable to those for the non-UV-A condition.

In UV-A DED, ultrasonic waves are imparted through the melt pool, as well as the surrounding solid and mushy zones. As resonance conditions change, vibrational amplitudes vary with build height z. It is well documented that acoustic waves experience exponential attenuation as they travel through a medium. In polycrystalline solids, this attenuation can occur through several routes. One is ultrasound scattering, where waves are split at the interface between grains or different phases and are either transmitted or reflected. As this occurs, the waves attenuate accordingly [81]. The amount of scattering tends to increase in larger, anisotropic grains [82]. Ultrasonic waves can also attenuate in solids through ultrasound absorption. Similar to ultrasound absorption in fluids (i.e., the melt pool), ultrasonic energy is converted to heat and transmitted throughout the solid [82]. However, absorption in solids occurs through several different mechanisms, such as oscillation of dislocations, thermoelastic effects, and phonon or electron scattering [83]. As the build height increases, the attenuation of ultrasonic waves through scattering and absorption in the build likely increases, due to the presence of more grain boundaries and a larger bulk volume. Ultrasonic waves are also likely scattered at the melt pool boundaries.

The exponential attenuation of acoustic waves can be expressed by the following equation for acoustic intensity [19]:

$$I = I_0 e^{-2\alpha x} \tag{2.5}$$

where I is the ultrasonic wave intensity, I_0 is the ultrasonic wave intensity at z=0, α is the attenuation factor, and x is the wave propagation distance (in this case, z plus the thickness of the substrate). Assuming an attenuation factor of 0.2 for 316L stainless steel [84], by the 15th layer of deposition, the UV intensity is approximately two-thirds of what it was at the first layer, and

continues to decrease as z increases. However, the attenuation factor used in the previous calculation was measured at room temperature. As Wu *et al*. reports, ultrasonic waves experience greater amounts of attenuation at higher temperatures [85]. As the solid surrounding the melt pool experiences high temperatures, and due to thermal accumulation at higher layers, the decrease in intensity is likely greater than what is predicted by Eqn. 2.5. Since a wave's intensity is proportional to the energy it carries, less energy is transferred into the melt pool during the deposition of higher layers. Therefore, the effects of acoustic cavitation, ultrasound absorption in the fluid, and acoustic streaming weaken accordingly, leading to an overall reduction of heat transfer into the melt pool.

This acoustic attenuation presents an interesting challenge that must be addressed going forward in the development of UV-A DED. To maintain a constant ultrasonic wave amplitude with increasing build height, one of two solutions should be considered. The first is to tune the ultrasonic frequency as the build height increases, which can be accomplished with magnetostrictive transducers [86]. The second is to develop a top-down approach to applying vibration to the melt pool, so that the wave propagation distance remains constant during deposition. Additionally, the size and geometry of components should be strongly considered, as large geometries or complex shapes will influence how ultrasonic waves propagate through the build and into the melt pool.

2.4.4 As-built microstructures and defects

The effects of UV on the melt pool's evolution and its interactions with injected particles translate to the final build's properties. Specifically, UV has an influence on solidification during deposition, as evidenced by the as-built microstructures. As shown in Fig. 2.5, fine equiaxed grains form near the substrate due to dendritic fragmentation. The pressure released from the collapse of cavitation bubbles mechanically fragments dendrites. Additionally, acoustic streaming transfers

hot liquid to the dendrites, re-melting them. In this state, the steady flow exerts stress on dendrites and damages them [87–89]. The dendrite fragments thereby act as nucleation sites for fine grains.

A stronger effect of UV was observed on the cellular dendrites. As shown in the insets in Fig. 2.5, a decrease in dendritic arm spacing of nearly 50% occurred near the substrate. It is well documented that dendritic arm spacing decreases with increasing cooling rate [3, 90]. As the cooling rate increases, there is insufficient time for lateral diffusion of rejected solute, thereby suppressing constitutional supercooling and leading to a smaller dendritic arm spacing [91]. It has been reported in casting and welding literature that vibration of molten metal causes a decrease in dendritic arm spacing [92–95]. The combination of acoustic streaming and collapse of cavitation bubbles enhance mixing of fluid, improving heat convection within the melt pool. Additionally, the melt pool growth results in a larger surface area for heat to conduct out of the melt. The enhanced heat transfer out of the melt pool through conduction and convection increases the cooling rate, thereby leading to the decrease in the dendritic arm spacing observed in Fig. 2.5.

Inducing UV within the melt pool is effective for mitigating harmful defects like lack-of-fusion porosity. Lack-of-fusion pores are large, irregularly shaped voids that form when successive melt pool layers fail to overlap one another [96]. The failure to overlap can be due to the improper selection of deposition parameters such as laser power, scan speed, spot size, and hatch spacing [97]; or partial melting of powder particles due to a lack of sufficient laser power for a given layer thickness and hatch spacing [33, 98]. According to Mukherjee and DebRoy [97], 316L stainless steel is particularly susceptible to the formation of lack-of-fusion porosity due to its high density, which results in smaller melt pools. To overcome the formation of such defects, it is recommended to optimize deposition parameters to achieve larger melt pools, a larger heat input into the melt pool, a higher Marangoni number, and a higher peak temperature within the melt pool [97].

Because of the three phenomena shown in Fig. 2.7, the melt pools of UV-A samples become larger and hotter, as observed in Figs. 2.2 and 2.3, leading to a lower average percentage of porosity. Our results indicate that UV-A DED can be used to achieve all four melt pool modifications suggested by Mukherjee and DebRoy [97] without changing deposition parameters, thereby suppressing the formation of such defects. Typically, efforts to mitigate keyholing and lack-of-fusion pores are opposite [3]. UV-A DED provides a unique opportunity to address both defects within the same processing window.

However, UV does not necessarily eliminate all defects from builds. Miniscule pores on the order of ~150 nm in diameter were concentrated at the grain boundaries of the UV-A samples, as shown in the inset in Fig. 2.6. Pores of such a small scale were not present in non-UV-A cubes. These small pores are likely residual cavitation bubbles that were not able to burst before being trapped at grain boundaries during solidification.

2.5 Summary

The effects of UV on melt pool evolution in DED of 316L stainless steel single-tracks and cubes were explored. For the first time, *in situ* high-speed imaging was utilized to analyze particle collisions with the melt pool surface for UV-A and non-UV-A single-track depositions. *In situ* thermal imaging was also used to track the melt pool thermal profiles during UV-A and non-UV-A deposition of higher layers in bulk cubic samples. The use of *in situ* imaging techniques allowed for the collection of robust quantitative data, which were key to elucidating the effects of UV on the thermal and spatial evolution of the melt pool during UV-A DED. Using optical microscopy, SEM, and EBSD, the microstructures and porosity in the as-built bulk samples were extensively characterized. The specific findings of this investigation are as follows:

1. An increase in melt pool temperature and dimensions were observed during UV-A DED due to the combined effects of acoustic cavitation, ultrasound absorption, and acoustic streaming.
2. The particle residence time on the melt pool surface was reduced by approximately half, and wettability of injected particles into the melt pool surface improved, due to a decrease in surface tension caused by UV.
3. The cooling rate increases and dendritic arm spacing decreases during UV-A DED because of enhanced mixing in the melt pool caused by acoustic streaming.
4. Fewer lack-of-fusion pores were observed in UV-A cube samples because of an increase in melt pool dimensions and temperature. However, residual nanoscale acoustic cavitation bubbles are trapped as gas pores at grain boundaries during solidification.
5. An equiaxed-to-columnar grain transition is observed in UV-A cube samples because effects of UV on the melt pool diminish as the build height increases due to the attenuation of ultrasonic waves over an increasing wave propagation distance.

Overall, the findings indicate that the application of UV impacts the melt pool such that it solidifies with refined microstructures and fewer defects during DED processing. However, the UV effects diminish with build height. In the future, these limitations must be considered, as large or complex geometries may reduce the propagation of ultrasonic waves into the melt pool. A means of keeping the wave amplitude constant should be considered, either by tuning the wave frequency *in situ*, or by applying UV with a top-down approach.

Chapter 3: Dislocation-mediated room-temperature mechanical behavior of multiphase entropy stabilized oxides

3.1 Background

As technological needs advance, conventional methods of developing new, suitable materials are falling short [99]. One creative solution was discovered in 2004, when two groups independently developed high entropy alloys (HEAs) [100, 101]. HEAs are composed of five or more elements in approximately equimolar concentrations, and are stabilized by high configurational entropy to form single-phase random solid solutions, as shown schematically in Fig. 3.1a [102]. A material's configurational entropy is maximized by including more components in equiatomic ratios, indicated by Fig. 3.1b [103]. By exploring the sparsely charted central regions of multi-element phase diagrams (shown in red in Fig. 3.1c), an expansive compositional design space is revealed, where entropy, rather than enthalpy, determines phase stability in a phenomenon coined as "entropy stabilization". However, there are concerns about whether HEAs are truly entropy stabilized, due to the presence of intermetallic phases and short-range order [104–107].

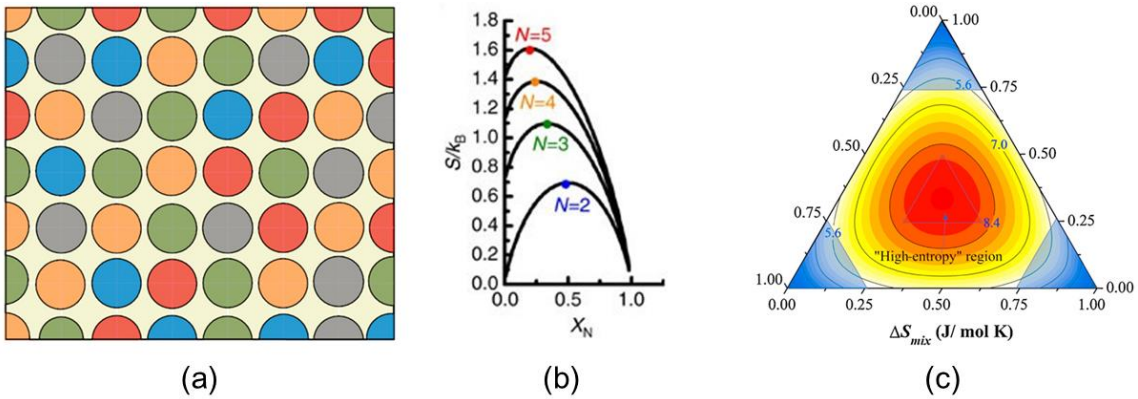

Figure 3.1: (a) The illustrated concept of random mixing of elements, as represented by the circles in different colors, in a multicomponent alloy. With equal atom size and loose atomic packing implicitly assumed, the configuration entropy of mixing of the alloy is equivalent to that of an ideal gas, thus being maximized when the elements are in equimolar amounts [102]; (b) Calculated configurational entropy in an N-component solid solution as a function of mol% of the Nth component [103];(c) The contour plot of ΔS_{mix} (J/mol K) on a schematic ternary alloy system. The blue corner regions indicate the conventional alloys based on one or two principal elements, whereas the red center region indicates the 'high-entropy' region [102].

Entropy stabilization results in the formation of a single-phase, random solid solution by increasing configurational entropy, according to the Gibbs free energy equation [108]:

$$\Delta G = \Delta H - T\Delta S \tag{3.1}$$

where ΔG is the Gibbs free energy, ΔH is enthalpy of formation, T is temperature, and ΔS is configurational entropy. For a material to be entropy stabilized, the Gibbs free energy of the entropy-driven phase state must overcome that the Gibbs free energy of the of the enthalpy-driven phase states [109]. As described by Eqn. 3.1, the role of entropy is regulated by temperature. Thus, a competition takes place between an entropy-stabilized single-phase state and a phase state containing ordered enthalpy-stabilized secondary phases, resulting in a reversible phase transformation. The reversible phase transformation allows the phase state of entropy-stabilized materials to be controlled by heat-treatment temperature.

In 2015, Rost *et al.* introduced entropy stabilized oxides (ESOs), a novel class of mixed oxide ceramics composed of five or more constituent oxides in equimolar ratios. The composition

explored in their study was the (CoCuMgNiZn)O transition metal ESO (hereafter referred to as TM-ESO), which takes on a single-phase rocksalt crystal structure after appropriate processing [103]. Rost et al. performed a series of solid-state reaction experiments, where they incrementally increased the sintering temperature of TM-ESO powders. After each sintering experiment, they used X-ray diffraction (XRD) to explore the phase evolution that occurs during the solid-state reaction of the five constituent oxides, as shown in the lefthand side of Fig. 3.2.

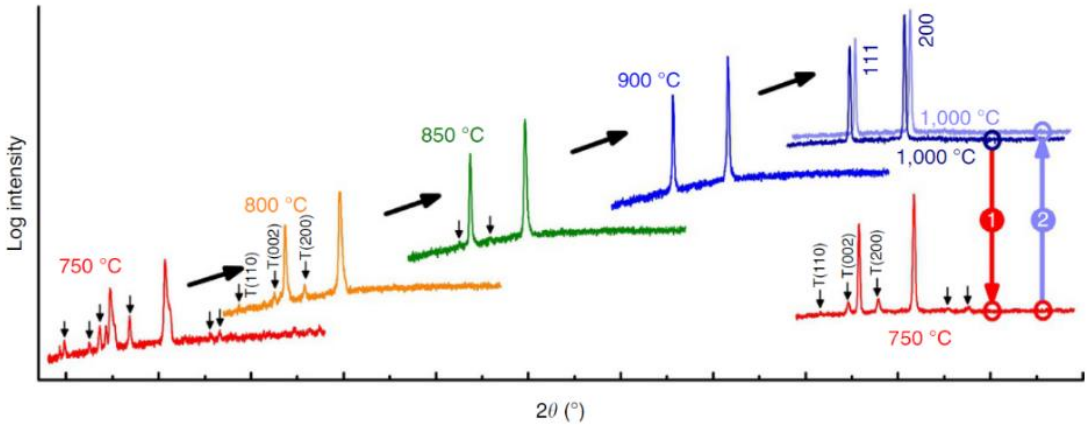

Figure 3.2: X-ray diffraction analysis of heat-treated ESOs: which consists of an equimolar mixture of MgO, NiO, ZnO, CuO and CoO. The patterns were collected from a single pellet. The pellet was equilibrated for 2 h at each temperature in air, then air quenched to room temperature by direct extraction from the furnace. X-ray intensity is plotted on a logarthimic scale and arrows indicate peaks associated with non-rocksalt phases, peaks indexed with (T) correspond to tenorite phases. The two X-ray patterns for 1,000 °C annealed samples are offset in 2θ for clarity [103].

At lower temperatures, the solid-state reaction is incomplete, and the TM-ESO is in a multiphase state, containing a tenorite phase and a rocksalt phase. XRD confirmed the presence of both phases at temperatures ranging from 750 °C to 850 °C. However, at a temperature of 900 °C, the solid-state reaction is complete, and the TM-ESO takes on a single-phase rocksalt crystal structure. Using scanning transmission electron microscope energy dispersive spectroscopy (STEM-EDS), Rost et al. demonstrated that in the single-phase rocksalt state, the cations are uniformly distributed, as shown in Fig. 3.3.

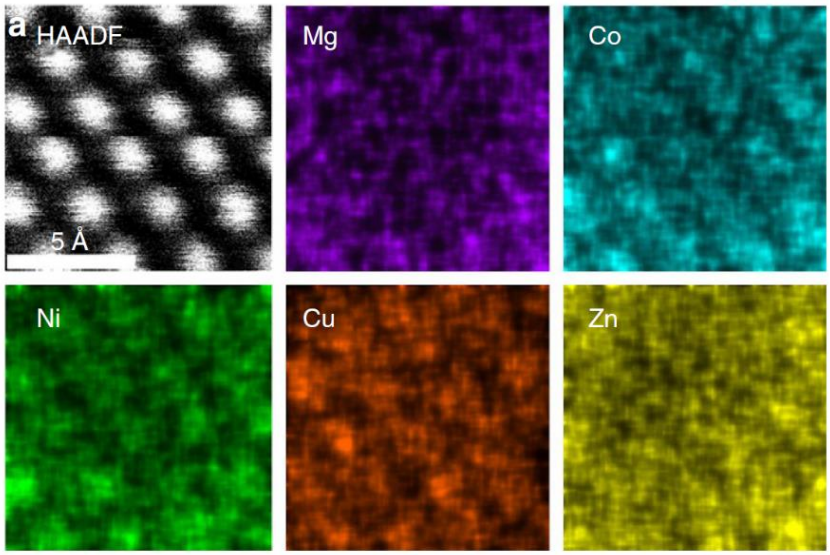

Figure 3.3: High-angle annular dark-field (HAADF) image. Panels labelled as Zn, Ni, Cu, Mg, and Co are intensity maps for the respective characteristic X-rays. The individual EDS maps show uniform spatial distributions for each element and are atomically resolved [103].

The uniform spatial distribution of each element indicates that the rocksalt phase has a random solid-solution structure, stabilized by high entropy of mixing. Rost et al. also observed an entropy-driven reversible phase transformation for TM-ESOs, where the phase state is regulated by temperature, as demonstrated by the reaction sequence on the right-hand side of Fig. 3.2. After heat treatment at 1000 °C, a single-phase rocksalt crystal structure was achieved. The material was once again heat-treated at 750 °C and contained both rocksalt and secondary tenorite phases. After another heat-treatment at 1000 °C, the single-phase rocksalt crystal structure was once again observed, indicating a temperature-dependent reversible phase transformation. The observed reversible phase transformation provides additional evidence that the single-phase state in TM-ESOs is stabilized by entropy. The reversible phase transformation indicates that the TM-ESO can be taken from a single-phase state to a multiphase state through simple heat-treatment, indicating that its mechanical behavior could potentially be tailored.

Rost et al. also did a series of experiments to confirm the influence of composition on maximizing entropy in TM-ESOs, as shown in Fig. 3.4. Removing any component from the system

causes a decline in configurational entropy, resulting in a departure from the single-phase rocksalt crystal structure, as shown in Fig. 3.4a. Additionally, altering the composition to be non-equiatomic increases the temperature at which the material transitions to a single-phase structure, as shown in Fig. 3.2c-g. Both experiments confirm that the phase transformation to a single-phase rocksalt crystal structure is driven by maximized configurational entropy.

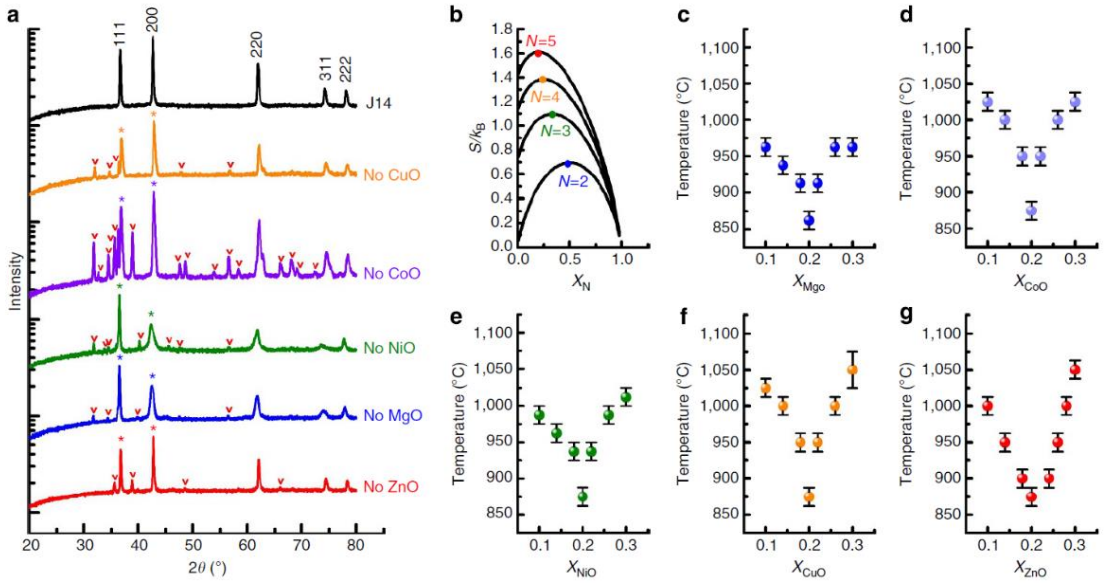

Figure 3.4: ESO Compositional Analysis: a) X-ray diffraction analysis for a series of ESOs where individual components are removed, heat-treated at conditions needed to produce a solid solution. Asterisks indicate rocksalt peaks, and carrots indicate other secondary phases; b) Calculated configurational entropy in an N-component solid solution as a function of mol% of the Nth component, and (c-g) partial phase diagrams showing transition temperatures to single phase as a function of composition in the intervals. Each phase diagram varies with the concentration of one element *[103]*.

The TM-ESO is hypothesized to be truly entropy stabilized, as demonstrated by a reversible phase transformation and maximized configurational entropy, shown in Figs. 3.2 and 3.3. Further investigation into TM-ESOs has revealed the interesting nature of the entropic phase transformation. In 2019, Dupuy *et al.* demonstrated that the reversible phase transformation in TM-ESOs is influenced by heat treatment conditions [110]. Dupuy *et al.* varied the heat treatment time and temperature of TM-ESOs and used X-ray diffraction (XRD) to explore the evolution of the secondary phases. Rietveld refinement was used to quantitatively analyze XRD data to estimate

the amount of secondary phase that formed for each heat treatment condition. Their results indicated that the secondary phases form in a temperature window of 650 – 850 °C, with the amount of secondary phase being maximized at a heat treatment temperature of 700 °C [111]. Using energy dispersive spectroscopy (EDS), Dupuy *et al.* demonstrated that the secondary phases that form during heat treatment are a Cu-rich tenorite phase and a Co-rich spinel phase, which coexist with the primary rocksalt phase [110]. Dupuy *et al.* also determined that the Cu-rich tenorite and Co-rich spinel secondary phases are multicomponent (i.e., all five cations are present in the secondary phase particles) but enriched in Cu and Co, respectively [112].

Since the publication of Rost's foundational paper in 2015, the field of high entropy ceramics has rapidly expanded. The concept of entropy stabilization has been applied to other ceramic systems, such as carbides [113, 114], borides [115], nitrides [116], sulfides [117], and fluorites [118]. Additionally, recent investigations into ESOs of various compositions have demonstrated that they display promising functional properties [119–121] and thermomechanical behavior [122–124], making them potential candidates for high-temperature applications like thermal barrier coatings, thermoelectric power generation, catalysts, and solid oxide fuel cells.

Although the field of entropy stabilized ceramics has rapidly expanded in recent years, an examination of the literature shows only a few studies investigating the mechanical behavior of TM-ESOs, and all are focused on single-phase TM-ESOs. For instance, Braun *et al.* used atomic force microscopy (AFM) on single-phase TM-ESO thin films and determined that the elastic modulus was 152.0 ± 10.6 GPa [122]. Pitike *et al.* used density functional theory (DFT) and nanoindentation to determine that single-phase TM-ESOs exhibit mechanical anisotropy due to local structure and magnetic configuration and that the elastic modulus ranges from 212-228 GPa [125]. Hong *et al.* varied the sintering temperature of single-phase TM-ESOs in 50 °C increments

from 800 °C to 1000 °C, and measured the grain size, relative density, bending strength, and elastic modulus of as-sintered samples. They reported that grain size and relative density increase with increasing sintering temperature, but that bending strength and elastic modulus peak at a sintering temperature of 900 °C, having values of 323 ± 19 MPa and 108 ± 5 GPa, respectively [126]. Wang *et al*. investigated the room-temperature mechanical deformation of single-phase TM-ESOs using nano-scratch tests, and found a high level of dislocation activity in the region of deformation [127].

Notably, the influence of the entropic phase transformation on the mechanical behavior of TM-ESOs, including hardness and elastic modulus, remains unexplored. Additionally, little is understood about how the presence of dislocations and their interactions with secondary phase particles influences the mechanical response in multiphase TM-ESOs. Previous studies on other multiphase ceramics demonstrate that secondary phases can influence their mechanical behavior. For example, Mayrhofer *et al.* reported an increase in hardness in heat-treated $Ti_{1-x}Al_xN$ ceramics due to the formation of a two-phase microstructure from spinodal decomposition [128]. Spinodal decomposition of yttria-stabilized zirconia (YSZ) also results in an increase in hardness [129].

Given recent investigations into the entropic phase transformations in TM-ESOs [110, 112] and the known influence of secondary phases on the mechanical response of ceramics [128, 129], as described above, the current investigation aims to develop an understanding of how room temperature mechanical properties, specifically hardness and elastic modulus, are influenced by the presence of secondary phases within multiphase TM-ESOs. TM-ESOs of various compositions were fabricated and heat treated at different time increments to form different quantities of secondary phases. The phase transformation was characterized using scanning electron microscopy (SEM), EDS, and XRD. Room-temperature Vickers hardness testing and nanoindentation were used to measure the hardness and elastic modulus, respectively, for each

processing condition. Scanning transmission electron microscopy (STEM) was used to analyze the interactions between dislocations and secondary phase particles inside and outside of the deformation region. Mechanisms that lead to the observed variations in hardness and elastic modulus were evaluated.

3.2 Experimental methosd

3.2.1 Selection of material composition

Three different TM-ESO compositions were selected: equimolar TM-ESO (CoCuMgNiZn)O), a Co-deficient composition with the chemical formula of $(CuMgNiZn)_{0.9}Co_{0.1}O$, and a Cu-deficient composition with a formula of $(CoMgNiZn)_{0.9}Cu_{0.1}O$. We hypothesize that by introducing a deficiency of Co and Cu, we can isolate the Cu-rich tenorite and Co-rich spinel secondary phases, respectively, to analyze their role on the mechanical behavior independently. The predicted theoretical densities and predicted secondary phases for each TM-ESO composition are provided in Table 3.1.

Table 3.1: Calculated theoretical densities and predicted secondary phases for each composition of TM-ESO.

TM-ESO Composition	**Chemical Formula**	**Theoretical density (g/cm^3)**	**Predicted Secondary Phases**
Equimolar	(CoCuMgNiZn)O	5.70	Cu-rich tenorite, Co-rich spinel
Co-deficient	$(CuMgNiZn)_{0.9}Co_{0.1}O$	5.61	Cu-rich tenorite
Cu-deficient	$(CoMgNiZn)_{0.9}Cu_{0.1}O$	5.67	Co-rich spinel

3.2.2 Powder preparation and fabrication of ESOs

TM-ESO powders for each composition were prepared through solid-state synthesis. A powder blend of constituent oxides was created from CoO, CuO, MgO, NiO, and ZnO oxide nanopowders (50 nm, 25 – 55 nm, 50 nm, 18 nm, 18 nm, respectively), which were all at least 99.7% pure (US Research Nanomaterials, Houston, TX, USA). These five oxide powders were blended with a

mortar and pestle, then placed in a Si_3N_4 planetary ball mill (PBM) jar with isopropyl alcohol and milled for 3 hr at 300 RPM in a Pulverisette 7 PBM instrument (Fritsch, Idar-Oberstein, Germany). The powder slurries were extracted from the PBM jar and boiled at 100 °C for 12 hr to evaporate the isopropyl alcohol. The dried powder was ground in a mortar and pestle to remove agglomerates. Bulk samples of each composition were consolidated using conventional sintering. Compacted green bodies were placed in an elevator furnace (CM Furnaces Inc. Bloomfield, NJ, USA) and conventionally sintered at 1100 °C for 12 hr to form fully dense, single-phase samples. After 12 hr, the samples were quenched in air to preserve the single-phase state.

The density of the as-sintered single-phase samples was measured using the Archimedes method [130] and compared to the theoretical density values provided in Table 3.1. Fracture surfaces were prepared for SEM analysis by sputter coating with 3 nm of iridium using an ACE600 sputter coating machine (Leica Microsystems, Wetzlar, Germany). The fracture surfaces were imaged with a Magellan 400 XHR SEM (FEI, Hillsboro, OR, USA), using an accelerating voltage of 5 kV and a current of 50 pA. The average grain size was calculated from the fracture surface micrographs by measuring the diameter of approximately 500 grains with the FIJI/ImageJ software [62].

3.2.3 Heat treatment and characterization of secondary phases

Previous work has demonstrated that heat treatments within a particular temperature window can stimulate the formation of secondary phases in TM-ESO [110]. In the current study, the single-phase samples were heat treated in the elevator furnace for either 2 or 12 hr to form secondary phases. The equimolar and Co-deficient compositions were heat treated at 700 °C, and the Cu-deficient composition was heat treated at 600 °C. For each composition, these temperatures were found to be the ones at which the most secondary phase forms upon heat treatment. The

samples were air quenched at the end of each heat treatment. The bulk samples were polished with 800 grit and 1200 grit SiC pads (Allied High-Tech Products, Inc., Compton, CA, USA), then with 6 μm and 1 μm diamond suspensions (PACE Technologies, Tucson, AZ, USA). XRD analysis was conducted with a SmartLab X-ray Diffractometer (Rigaku, Tokyo, Japan), at a 2θ range of 30° to 80°. Rietveld refinement was performed on the acquired XRD data using the Maud software [131] to estimate the relative atomic fractions of the primary rocksalt, Cu-rich tenorite, and Co-rich spinel phases for each heat treatment condition for the three compositions.

The polished equimolar and Co-deficient samples were mounted onto SEM stubs with colloidal silver paste (Ted Pella Inc., Redding, CA, USA) and sputter coated with 3 nm of iridium. EDS was performed in a GAIA3 SEM-FIB microscope (Tescan, Brno, Czechia) using a silicon drift detector with an area of 150 mm^2 (Oxford Instruments, Abingdon, UK). A working distance of 5 mm and an accelerating voltage of 5 kV were used. Our previous work has demonstrated that performing EDS with low accelerating voltages is useful for resolving the fine secondary phase features found in TM-ESO [110].

3.2.4 Room-temperature Vickers hardness testing

Vickers hardness indentation experiments were performed at room temperature on single-phase and multiphase samples. Samples were first mounted in Konductomet mounting media (Buehler, Lake Bluff, IL, USA) and polished down to a 1 μm finish. Vickers hardness indentation measurements were done with a Wilson VH3300 indenter (Buehler, Lake Bluff, IL, USA) with a load of 100 g and a dwell time of 10 s. Fifteen measurements were taken per sample. Depth profiles from corner to corner for each indent were collected with a LEXTTM OLS5100 3D Laser Scanning Microscope (Olympus, Tokyo, Japan) to get accurate measurements of indent

dimensions to estimate hardness values. Indent dimensions were used to determine the Vickers hardness values, *H*, for each sample using the following equation [132]:

$$H = 1.854\frac{F}{(2a)^2} \tag{3.2}$$

where *F* is the load (kg) and *a* is the indent half diagonal (m).

Electron transparent lamella samples were prepared for STEM experiments using focused ion beam (FIB) milling. Lamella samples were prepared using FIB lift-out techniques from two regions of an equimolar sample that was heat treated for 12 hr at 700 °C: both inside and outside the plastic deformation zone created by the Vickers hardness indentation. The lamella samples were each 10 μm long, 5 μm wide, and 100 nm thick. The lamella sample from inside the plastic deformation zone was lifted out from underneath the Vickers indent, along its diagonal. The lamella sample from outside the deformation zone was lifted from a region of the sample far from the cluster of indents to ensure that it was not affected by the deformation zone below the indents, a distance more than 10 times the size of the indent [133, 134]. A JEOL 2800 TEM/STEM (JEOL Ltd., Tokyo, Japan) was used at 200 kV with a Gatan OneView Camera (AMETEK, Berwyn, PA, USA) to observe dislocations and secondary phase morphology.

3.2.5 Room-temperature nanoindentation

Nanoindentation experiments were performed at room temperature with a Hysitron PI-85 system (Bruker, Billerica, MA, USA) to measure elastic modulus. Samples were first polished to a 1 μm finish and mounted to a sample holder with silver paste. A Berkovich tip was used to apply a load of 5 mN at a load rate of 1 mN/s and a hold time of 2 s. Fifty measurements were taken per sample, and elastic modulus values were calculated by a proprietary Bruker software.

3.3 Results

3.3.1 Microstructures and secondary phase evolution

The as-sintered samples had a relative density of 99%. Representative micrographs depicting the microstructure of the three different compositions in their as-sintered state are displayed in Fig. 3.5. The grains take on an equiaxed structure in all compositions. The equimolar TM-ESO has the largest grain size (12.1 ± 4.8 μm), followed by the Co-deficient TM-ESO (7.6 ± 3.1 μm), and the Cu-deficient TM-ESO (4.0 ± 1.3 μm).

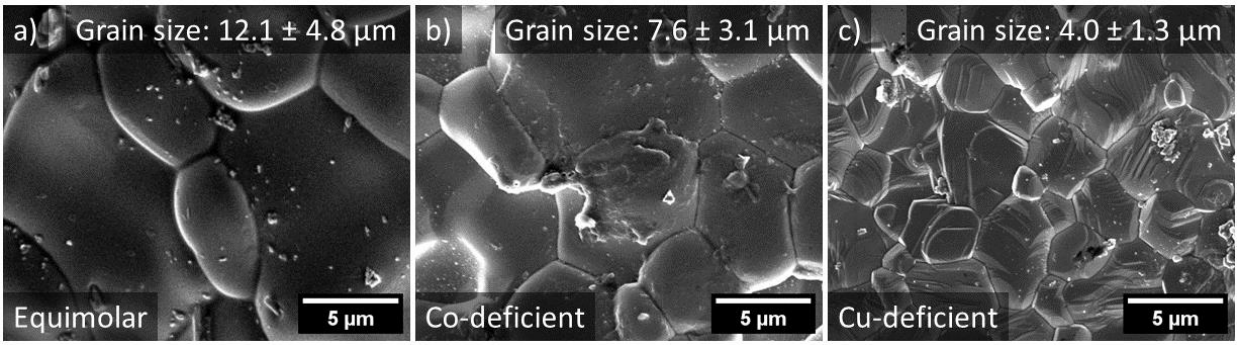

Figure 3.5: Fracture surfaces of as-sintered TM-ESO with: a) equimolar composition, b) Co-deficient composition, and c) Cu-deficient composition. Average grain size values are provided for each.

XRD results are shown in Fig. 3.6. For all three compositions, the XRD spectra corresponding to the as-sintered state (0 hr heat treatment, shown in black) indicate a single-phase rocksalt crystal structure, with no sign of any extraneous peaks or secondary phases. After 2 hr of heat treatment, peaks corresponding to Cu-rich tenorite and Co-rich spinel secondary phases appear for the equimolar composition. For the Co-deficient composition, peaks corresponding to the Cu-rich tenorite appear. The Cu-deficient composition remained in a single-phase state. As the heat treatment time increases to 12 hr, the peaks corresponding to the secondary phases become more prominent for the equimolar and Co-deficient compositions, indicating that the secondary phases increased in concentration. Peaks corresponding to the Co-rich spinel phase appear for the Cu-deficient composition after 12 hr of heat treatment.

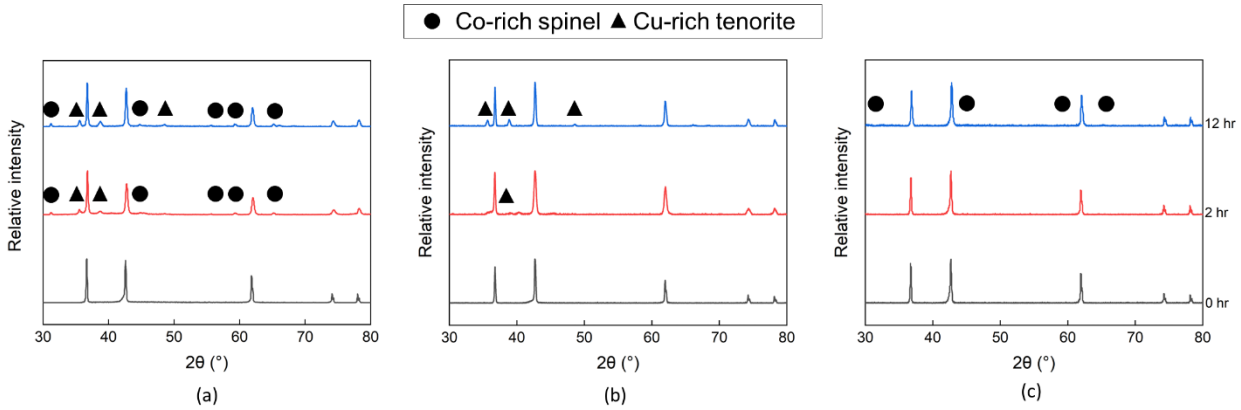

Figure 3.6: X-ray diffraction spectra showing the phase evolution for TM-ESO heat treated for 0, 2, and 12 hr time intervals; a) equimolar composition, b) Co-deficient composition, and c) Cu-deficient composition. The as-sintered samples are single phase, and the heat-treated samples are multiphase.

Rietveld refinement results for quantification of the atomic fraction (at %) of secondary phases are summarized in Table 3.2. For the equimolar composition, after 2 hr of heat treatment, there is an equal amount of the Co-rich spinel and Cu-rich tenorite secondary phases (6 at % each). After 12 hr of heat treatment, there is more Cu-rich tenorite (14 at %) than Co-rich spinel (10 at %). For the Co-deficient composition, as the heat treatment time increases from 2 to 12 hr, the concentration of Cu-rich tenorite increases from approximately 5 at % to 16 at %. For the Cu-deficient compositions, after 12 hr of heat treatment, there is 8 at % Co-rich spinel.

Table 3.2: Concentration of primary (rocksalt) and secondary (Cu-rich tenorite and Co-rich spinel) phases as a function of heat treatment time and TM-ESO composition.

TM-ESO Composition	**Heat Treatment Time (hr)**	**Rocksalt (at %)**	**Cu-rich Tenorite (at %)**	**Co-rich Spinel (at %)**
Equimolar	0	100	0	0
	2	88	6	6
	12	76	14	10
Co-deficient	0	100	0	0
	2	95	5	0
	12	84	16	0
Cu-deficient	0	100	0	0
	2	100	0	0
	12	92	0	8

Secondary electron (SE) images and the corresponding Cu composition maps captured through

EDS are shown in Fig. 3.7. For the equimolar sample, the Cu-rich tenorite particles take on a needle-like morphology after 2 hr of heat treatment, as shown in Fig. 3.7a & b. After 12 hr of heat treatment, these Cu-rich particles coarsen and adopt a slight curvature, shown in Fig. 3.7c & d. In the Co-deficient composition, after 2 hr of heat treatment, the Cu-rich needles are well-formed, straight, and more elongated than the equimolar composition, as shown in Fig. 3.7e & f. After 12 hr of heat treatment, the Cu-rich needles coarsen, but maintain their straight morphology, shown in Fig. 3.7g & h. The images captured of the Cu-rich tenorite particles were used to determine their variations in size and spacing as the heat treatment time increases.

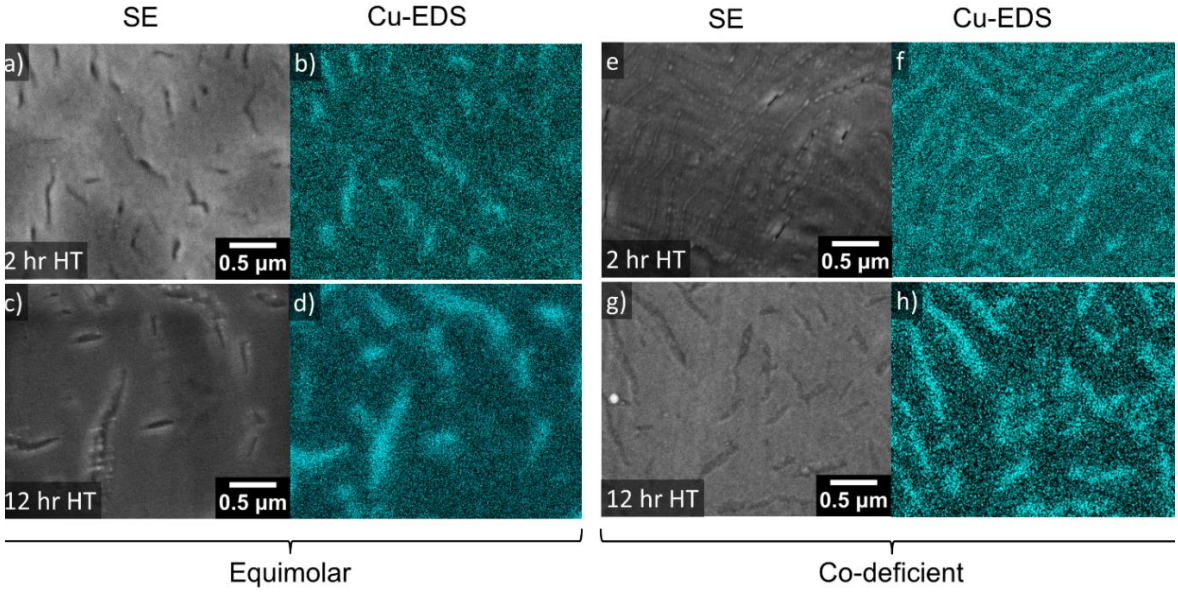

Figure 3.7: Secondary electron (SE) SEM and corresponding Cu-EDS maps of Cu-rich tenorite phases in (a) – (b) equimolar, 2 hr heat treatment; (c) – (d) equimolar, 12 hr heat treatment; (e) – (f) Co-deficient, 2 hr heat treatment; (g) – (h) Co-deficient, 12 hr heat treatment. HT refers to heat treatment.

3.3.2 Hardness results and dislocation activity in multiphase TM-ESO

Vickers hardness test results are shown in Fig. 3.8. Values range from 3700 ± 120 MPa to 6400 ± 190 MPa, depending on composition and heat treatment conditions. For the equimolar and Co-deficient composition, the hardness initially increases from the as-sintered single-phase state to the 2 hr heat-treated state. After 12 hr of heat treatment, the hardness decreases. For the

equimolar composition, the hardness decreases until it is lower than it was in the single-phase state. For the Co-deficient composition, the hardness decreases until it reaches a level very similar to its single-phase state. The hardness test results for the equimolar and Co-deficient TM-ESO compositions indicate that as the amount of secondary phase increases, the TM-ESO hardens then softens. The Cu-deficient composition continuously increases in hardness as heat treatment time increases and the secondary phase starts to form. In addition to the influence of heat treatment time, composition also plays a role in hardness. The Co-deficient composition has the highest overall hardness, and the Cu-deficient composition has the lowest overall hardness, regardless of heat treatment condition.

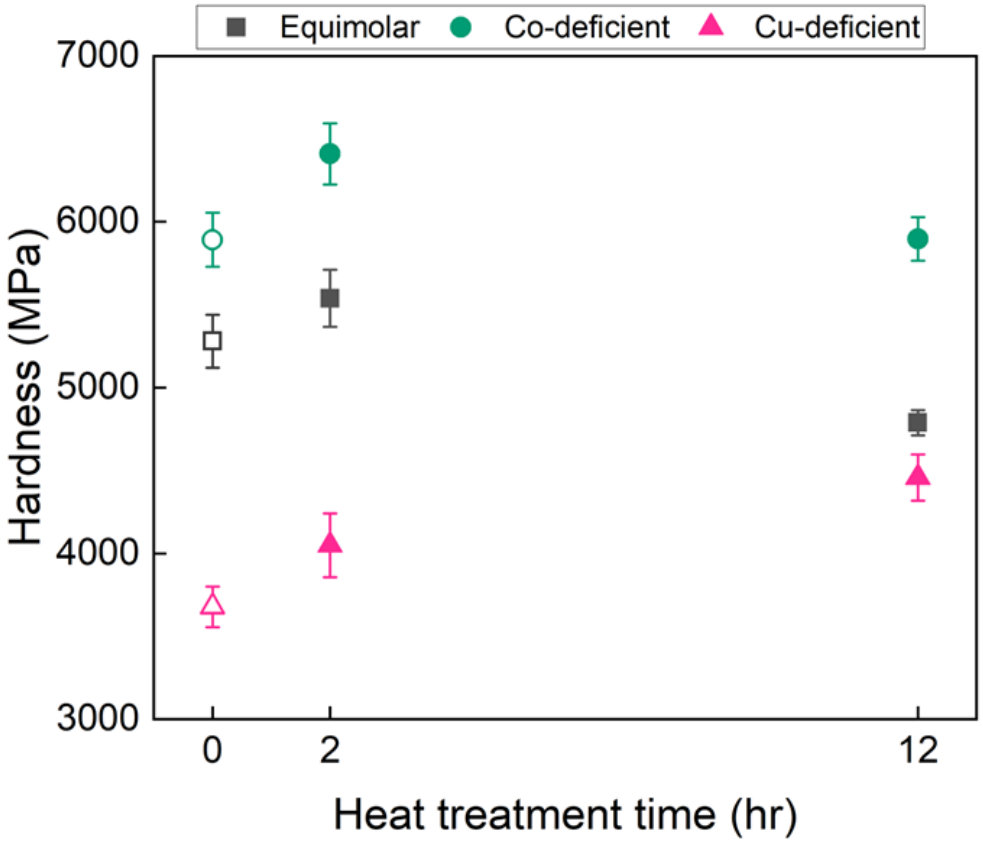

Figure 3.8: Room-temperature Vickers hardness results for equimolar, Co-deficient, and Cu-deficient TM-ESOs: as-sintered, heat treated for 2 hr, and heat treated for 12 hr. The as-sintered samples are single-phase (represented by the open symbols at 0 hr), and the heat-treated samples are multiphase (represented by closed symbols at 2 hr and 12 hr), as summarized in Table 3.2.

Fig. 3.9 shows dislocation activity in an equimolar TM-ESO sample that was heat treated for 12 hours. A TEM bright field micrograph of a region outside of the plastic deformation zone (i.e., away from the Vickers indent) is shown in Fig. 3.9a. The dark regions are Cu-rich tenorite secondary phase particles. In this region, there is little to no dislocation activity outside of the plastic deformation zone, indicating that TM-ESO does not have a meaningful concentration of dislocations prior to deformation. Fig. 3.9b shows a STEM dark field micrograph taken from directly underneath the indent. The bright regions are the Cu-rich tenorite secondary phase particles, and the dark regions are dislocation clouds. After deformation, there is significant

dislocation activity in the deformation zone. Additionally, the dislocations pile up near the Cu-rich tenorite particles, indicating that they interact directly with these secondary phase particles.

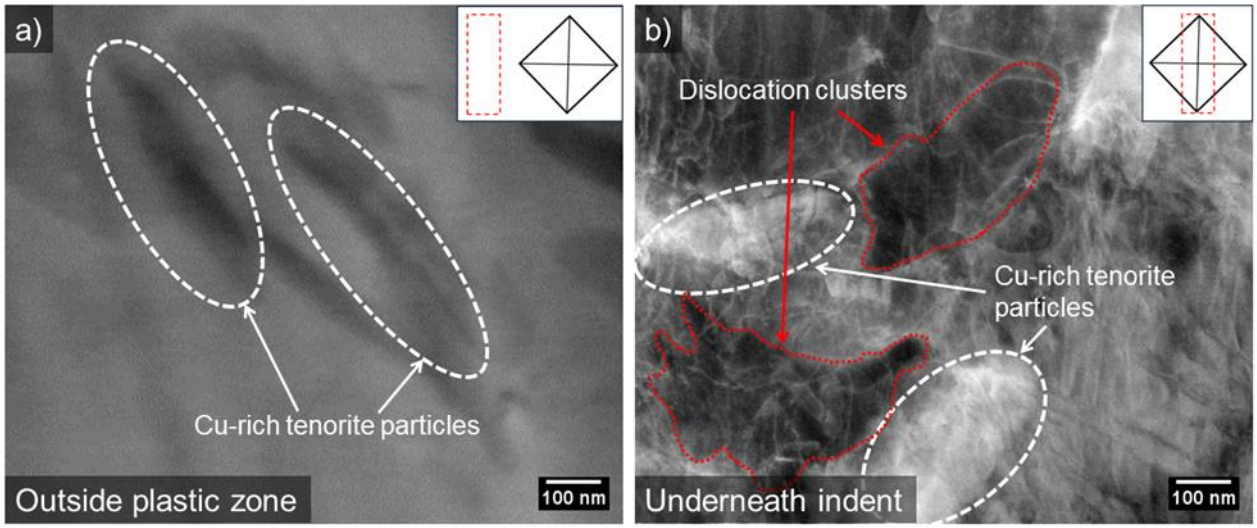

Figure 3.9: TEM micrographs taken from an equimolar TM-ESO sample that was heat treated at 700°C for 12hr showing: a) A TEM bright field image from outside the plastic deformation zone far from the Vickers indents, and b) a STEM dark field micrograph from inside the plastic deformation zone located underneath the Vickers indent. Cu-rich tenorite secondary phase particles are highlighted in white and dislocation clusters are highlighted in red. The inset schematics indicate the location of the lift-outs relative to the indent (note: these are not to scale).

3.3.3 Elastic modulus results in multiphase TM-ESO

Nanoindentation was performed to acquire elastic modulus values. No noticeable pop-in effects were observed in the load vs. displacement curves for each heat treatment condition across all compositions. Representative load vs. displacement curves are shown in Fig. A.1 in Appendix A. The results from elastic modulus measurements are shown in Fig. 3.10. Values range from 140 ± 5 GPa to 170 ± 6 GPa, depending on composition and heat treatment conditions. The elastic modulus for the equimolar composition increases as heat treatment time increases and more secondary phases form. For the Co-deficient and Cu-deficient compositions, the elastic modulus varies with the secondary phase composition.

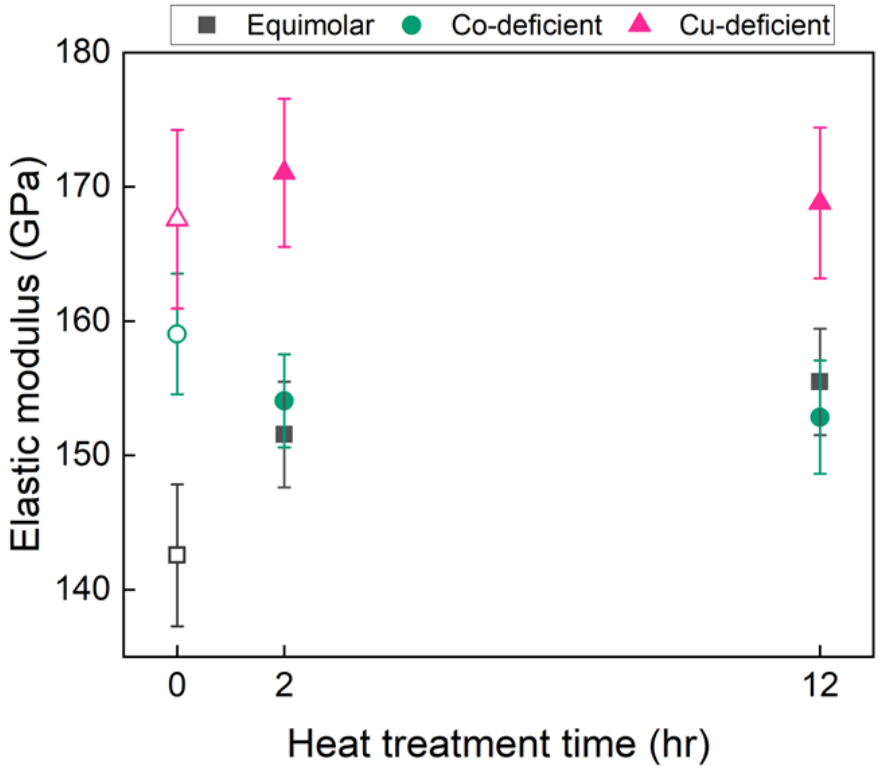

Figure 3.10: Room-temperature elastic modulus results for the equimolar, Co-deficient, and Cu-deficient TM-ESO after heat treating for 0 hr, 2 hr, and 12 hr. As-sintered samples are single phase (represented by open symbols at 0 hr), and heat-treated samples are multiphase (represented by closed symbols at 2 hr and 12 hr), as summarized in Table 3.2.

3.4 Discussion

3.4.1 Room-temperature hardness trends in multiphase TM-ESO

Mechanical properties such as hardness and strength are influenced by several mechanisms, such as dislocation activity. Dislocation activity is not typically prescribed as a dominant influence in the deformation behavior of ceramics, which are more likely to deform in a brittle manner, as their slip systems are difficult to activate [135]. Notably, unusually high dislocation activity has been previously observed in ESOs [127, 136]. The TEM micrographs in Fig. 3.9 show that dislocations are present in the deformation region but are not observed outside of that region, indicating that the dislocations are not intrinsic to the TM-ESO but were introduced during the

room-temperature indentation experiments. Additionally, Fig. 3.9b shows that dislocations interact directly with secondary phase particles. Based on the previous literature and our observations of dislocation activity in this investigation, we hypothesize that dislocations play a significant role in the room-temperature mechanical behavior of TM-ESOs. As such, the ensuing discussion is interpreted through the lens of classical dislocation phenomena, more specifically, precipitation strengthening.

Precipitation strengthening accounts for several strengthening mechanisms caused by the interactions of moving dislocations with precipitates or secondary phase particles [15]. Precipitation strengthening is commonly observed in metals, where slip systems are readily activated and dislocations move easily [135]. Notably, precipitation strengthening has also been observed in ceramic systems, such as $MgAl_2O_4$ spinel [137]. Precipitation strengthening mechanisms can be categorized depending on how moving dislocations interact with secondary phase particles [138, 139]. The first category is by shearing, where dislocations directly cut through the particle. Shearing mechanisms typically dominate when particles are small and coherent with their surroundings (e.g., early-stage precipitation). The second category is bypassing, where dislocations pass the particle rather than shear directly through. Bypassing mechanisms typically dominate when the size of the secondary phase particle exceeds a critical value (e.g., late-stage precipitation) or when particles are incoherent with their surroundings. Shearing and bypassing mechanisms occur simultaneously and independently of each other. Additionally, each mechanism contributes a specific strengthening increment. Whichever mechanism has the smallest strengthening increment value is the mechanism that is easiest to activate, meaning that this "softer" mechanism initiates and controls plastic deformation [138, 139].

To explore the potential strengthening mechanisms in multiphase TM-ESO materials, three specific hardening mechanisms are evaluated: coherency hardening, modulus hardening, and Orowan hardening. Coherency hardening and modulus hardening are shearing mechanisms, while Orowan hardening is a bypassing mechanism. Coherency hardening occurs when the coherency of the secondary phase particles with the primary phase leads to internal lattice strain, resulting in associated stress fields that draw or repel dislocations to or away from the particle [15]. The value of the strengthening increment, τ_{coh}, due to coherency hardening can be estimated with the following equation [15]:

$$\tau_{coh} \cong 7|\varepsilon_{coh}|^{3/2} G \left(\frac{rf}{b}\right)^{1/2} \tag{3.3}$$

where r is the secondary phase particle radius, f is the volume fraction of particles, G is the shear modulus of the secondary phase particle, and b is the magnitude of the Burger's vector in the primary phase (the rocksalt phase). ε_{coh} can be expressed by the following equation [15]:

$$\varepsilon_{coh} = \frac{a_p - a_m}{a_m} \tag{3.4}$$

where a_p is the lattice parameter of the secondary phase particle and a_m is the lattice parameter of the surrounding primary phase.

Modulus hardening occurs when a dislocation enters a secondary phase particle that has a different shear modulus than that of the surrounding primary phase, altering the dislocation line tension [15]. The strengthening increment, τ_{Gp}, caused by modulus hardening can be estimated with the following equation [15]:

$$\tau_{Gp} \cong 0.01 G {\varepsilon_{Gp}}^{3/2} \left(\frac{rf}{b}\right)^{1/2} \tag{3.5}$$

ε_{Gp} can be expressed with the following equation:

$$\varepsilon_{Gp} = \frac{G - G_m}{G_m} \tag{3.6}$$

where G_m is the shear modulus of the surrounding primary phase.

Orowan hardening occurs when a dislocation approaches a secondary phase particle, bows around it, and forms a loop before eventually continuing through the primary phase [15]. The strengthening increment, τ_B, due to Orowan hardening can be estimated with the following equation [15]:

$$\tau_B \cong \frac{Gb}{(L - 2r)} \tag{3.7}$$

where L is the mean spacing between secondary phase particles.

Estimated results for coherency hardening, modulus hardening, and Orowan hardening strengthening increments are listed in Table 3.3. Values for f, b, a_m, and a_p were collected from XRD data (see Fig. 3.6 and Table 3.2). Values for r and L for the Cu-rich tenorite secondary phase particles were approximated from SEM and EDS images (see Fig. 3.7). Values for r and L for the Co-rich spinel phase were approximated from the literature [112]. Shear modulus data for the secondary phases were collected from the literature [125, 140]. All values used for these calculations are tabulated in Tables A.2-A.4 in Appendix A.

Table 3.3: Estimated strengthening increment values for coherency hardening, modulus hardening, and Orowan hardening for multiphase equimolar, Co-deficient, and Cu-deficient TM-ESO. The bolded values represent the controlling mechanism. Rows are highlighted to guide the reader's eyes across, rather than down columns.

TM-ESO Composition	**Heat Treatment Time (hr)**	**Hardening Mechanism**		
		Coherency (GPa)	**Modulus (GPa)**	**Orowan (GPa)**
Equimolar	2	8.6	**0.1**	1.8
	12	11.7	0.12	**0.10**
Co-deficient	2	7.2	**0.1**	0.3
	12	7.8	0.081	**0.078**
Cu-deficient	2	**0.01**	0.04	67.8
	12	8.6	**0.1**	1.8

As shown in Table 3.3, the equimolar samples experience a change in the controlling hardening mechanism from modulus hardening (with a strengthening increment of 0.1 GPa) after 2 hr of heat treatment to Orowan hardening (with a strengthening increment of 0.1 GPa) after 12 hr of heat treatment. Similarly, the Co-deficient samples experience a transition from modulus hardening (with a strengthening increment of 0.081 GPa) after 2 hr of heat treatment to Orowan hardening (with a strengthening increment of 0.078 GPa) after 12 hr of heat treatment. As shown in Fig. 3.8, the equimolar and Co-deficient compositions initially harden after 2 hr of heat treatment, and then soften after 12 hr of heat treatment. Such a trend in hardness increasing then decreasing with heat treatment is attributed to a change in the controlling hardening mechanism from a shearing mechanism to a bypassing mechanism. As the heat treatment time increases, the secondary phase particles coarsen and the particle spacing increases, as shown in Fig. 3.7, due to copper diffusion from the primary phase into the Cu-rich tenorite secondary phase, causing it to be more energetically favorable for dislocations to bow around secondary phase particles rather than shear directly through them [15]. Additionally, as the secondary phase particles further coarsen and particle spacing increases with longer heat treatment time, the stress associated with dislocation bowing decreases, meaning that less energy is imparted during bowing [15]. These

secondary-phase particle coarsening effects are reflected in the observed trends for equimolar and Co-deficient TM-ESOs by the decrease in hardness with longer heat treatment time. Overall, this transition from a shearing mechanism to a bypassing mechanism, and consequential increase and decrease in room-temperature hardness, is similar to hardening trends observed in Ni-Al alloys [15, 141] and age-hardened Al-Cu alloys [108, 142].

A different trend is observed in the hardness data for the Cu-deficient composition. As shown in Fig. 3.8, the Cu-deficient samples initially strengthen after 2 hr of heat treatment, although no Co-rich spinel formed at this stage according to XRD results shown in Fig. 3.6. Dupuy *et al.* has shown that Co-rich spinel and Cu-rich tenorite secondary phases form through the nucleation and growth of nanoparticle precursor phases, and their eventual transition into their respective secondary phases [112]. According to Dupuy *et al.*, these nanoparticle precursor phases have distorted rocksalt lattice structures. Though distorted, these nanoparticle precursor phases are coherent with the primary rocksalt phase, likely contributing to coherency hardening as the controlling hardening mechanism with a strengthening increment of 0.01 GPa, as shown in Table 3.3. This phenomenon is similar to the role of GP-zones in age-hardened Al-Cu alloys, which cause lattice distortions while maintaining coherency with their surroundings, causing hardening to occur at shorter ageing times [108, 142]. After 12 hr of heat treatment, Co-rich spinel secondary phase particles have formed. Notably, the Cu-deficient samples harden further – they do not soften as is observed for the equimolar and Co-deficient compositions. As shown in Table 3.3, the change in strengthening increment values from 0.01 GPa for coherency hardening at 2 hr heat treatment to 0.1 GPa for modulus hardening at 12 hr heat treatment indicates a transition from coherency hardening to modulus hardening. At this stage, the observed increased in hardness is likely due to a change in dislocation line tension as dislocations shear directly through the newly formed Co-rich

spinel secondary phase particles, which have a different shear modulus than the surrounding primary rocksalt phase. We propose here that the strengthening trend observed for the Cu-deficient composition is caused by a transition from coherency hardening due to the distortion of the lattice by coherent nanoparticle precursor phases, to modulus hardening upon complete formation of the Co-rich spinel secondary phase particles. The overall hardening trends and associated strengthening mechanisms are summarized in Fig. 3.11.

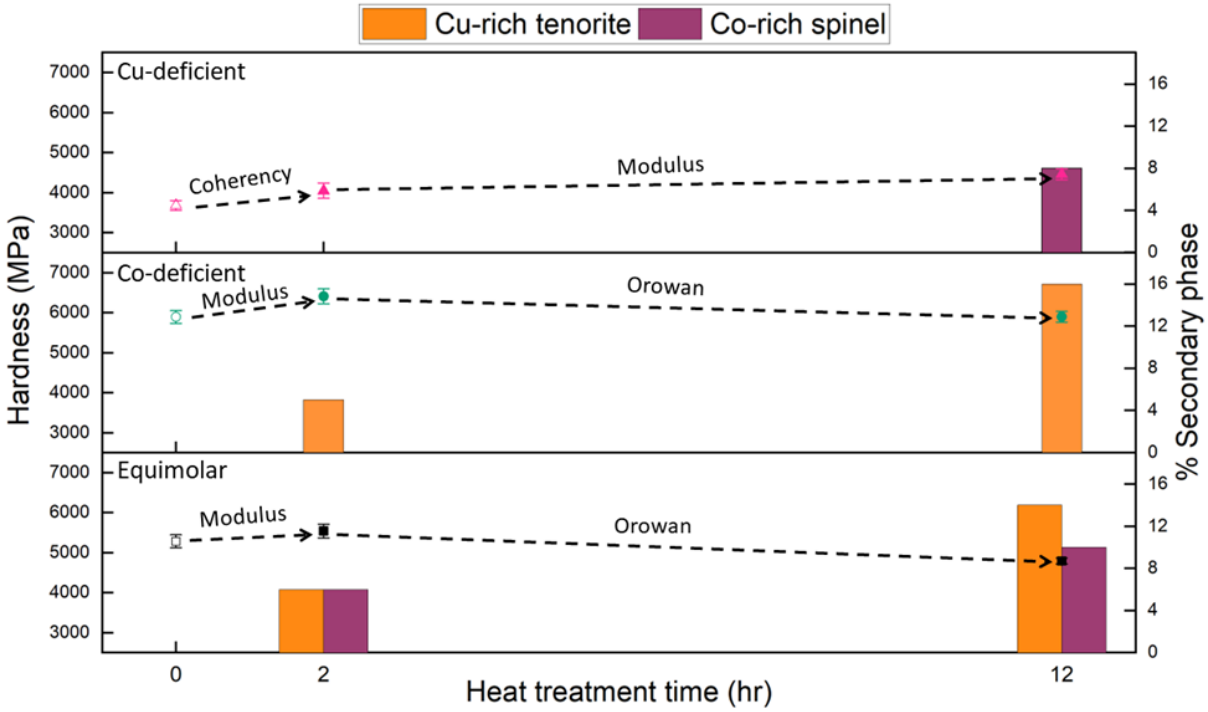

Figure 3.11: A schematic summarizing the room-temperature hardening trends observed in equimolar, Co-deficient, and Cu-deficient TM-ESO with increasing amounts of secondary phase due to longer heat treatments and associated strengthening mechanisms. The as-sintered samples are single-phase (as represented by the open symbols at 0 hr), and heat treated sampled are multiphase (as represented by the closed symbols at 2 hr and 12 hr), as summarized in Table 3.2.

3.4.2 Room-temperature elastic modulus trends in multiphase TM-ESO

Some studies suggest that the elastic modulus of a multiphase material is influenced by the elastic moduli and concentration of the secondary phase particles, if the elastic moduli of secondary phase particles are significantly different than that of the surrounding primary phase [143, 144]. This behavior is consistent with conventional composite materials, where an applied

load is transferred from a matrix phase to the embedded fibers [145]. The TM-ESO samples in this study were fully dense and had similar microstructures across all compositions (Fig. 3.5), eliminating density and microstructure as influences on elastic modulus. As such, we hypothesize that the variations in elastic modulus observed in this study (Fig. 3.10) are due to the formation of secondary phases and that the behavior is similar to that of conventional composite materials. Thus, we applied the Voigt model to estimate elastic modulus as a weighted average of the elastic moduli values of the primary rocksalt phase, and the secondary Cu-rich tenorite and Co-rich spinel phases. The Voigt model was selected as it is a simple approximation that can be used to estimate the elastic modulus of a material containing more than two phases. The equation for the Voigt model is [146]:

$$E = \sum v_i \cdot E_n \tag{3.8}$$

where v_i is the volume fraction of each respective phase, and E_n is the modulus of each respective phase. Lower and upper bound elastic modulus values found in literature for the secondary phases, listed in Table A.5 in Appendix A, were used to estimate a range of expected elastic modulus values for the equimolar, Co-deficient, and Cu-deficient TM-ESOs. The experimental elastic modulus values are plotted together with this range of expected values estimated with the Voigt model in Fig. 3.12.

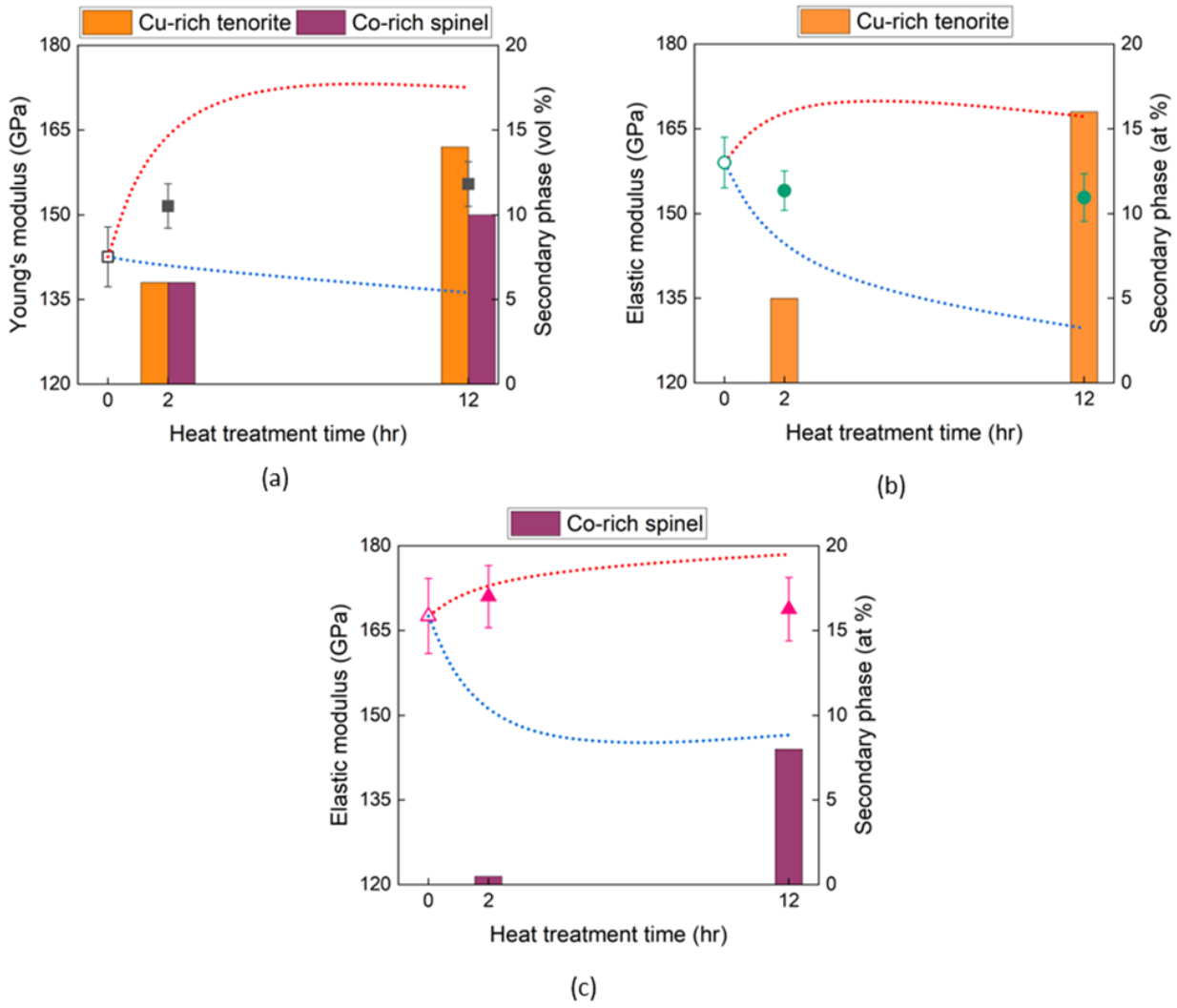

Figure 3.12: Graphs showing room-temperature elastic modulus values and where they fall within the range of expected elastic modulus values estimated by the Voigt composite model (red dotted lines and blue dotted lines, respectively) for: a) equimolar, b) Co-deficient, and c) Cu-deficient TM-ESO. As-sintered samples are single-phase (as represented by the open symbols at 0 hr), and heat-treated samples are multiphase (as represented by the closed symbols at 2 hr and 12 hr), as summarized in Table 3.2.

The room-temperature elastic modulus values for all three compositions fall within the range of expected values calculated with the Voigt model, as shown in Fig. 3.12. While this range of values is not intended to explain the cause for the change in elastic modulus observed experimentally as more secondary phases form, it does provide an indication of how reasonable the experimentally measured values are for the multiphase TM-ESO materials, relative to what has

been previously reported in literature for elastic modulus values for CuO tenorite and Co_3O_4 spinel. The room-temperature elastic modulus values for the equimolar and Co-deficient compositions fall approximately in the middle of the expected range. In contrast, the measured values for the Cu-deficient composition skew towards the higher values, indicating that the Co-rich spinel elastic modulus is likely closer to the upper bound elastic modulus value for Co_3O_4 spinel, as shown in table A.5 in Appendix A.

3.4.3 Influence of composition on room-temperature mechanical behavior of single-phase TM-ESO

Composition significantly influences the overall room-temperature hardness and elastic modulus of the TM-ESO materials in this study, even in the as-sintered single-phase state. As shown in Figs. 3.8 and 3.10, the single-phase equimolar, Co-deficient, and Cu-deficient TM-ESOs have room-temperature hardness values of approximately 5300 MPa, 5900 MPa, and 3700 MPa, respectively, and room-temperature elastic modulus values of approximately 140 GPa, 160 GPa, and 170 GPa, respectively. Similar changes in mechanical behavior with changes in composition have also been observed experimentally in HEAs [147, 148]. Such changes in mechanical properties are often attributed to changes in lattice distortion and solute configuration with changes in composition [147, 148]. As a result, the energy associated with two types of interactions changes: cation-dislocation interactions, and cation-cation interactions, which cause an elastic effect and a chemical effect, respectively [147, 148].

The elastic effect refers to changes in the energy associated with cation-dislocation interactions, which influence hardness and strength. As the composition of the TM-ESO changes, the location of cations, relative to dislocations, changes. Thus, the energy needed for a dislocation to travel through the lattice changes accordingly [147], resulting in an effect similar to solid-solution

strengthening [15]. To estimate if the variations in hardness caused by changes in composition can be caused by the elastic effect, solid-solution strengthening increment values were calculated using the following equation [139]:

$$\Delta\tau_{ss} = MGB\varepsilon_{ss}^{3/2}\sqrt{c} \quad (3.9)$$

where M is the mean orientation factor (3.06 for FCC solids such as the primary rocksalt phase), ε_{ss} is a structural parameter that factors in changes in lattice parameter and shear modulus, and c is solute concentration, expressed in atomic fraction. The strengthening increment values predicted by Eqn. 3.9 are listed and compared to the experimentally measured increment values, as shown in Table 3.4. The predicted and experimental strengthening increment values are within an order of magnitude of each other. Thus, we propose that changes in cation-dislocation interaction energies caused by changes in composition lead to solid-solution strengthening, which contributes to the observed changes in hardness of the single-phase samples as a function of composition.

Table 3.4: Predicted and experimental strengthening increment values for solid-solution strengthening of single-phase TM-ESOs. The increment values represent the change in hardness from the baseline equimolar composition.

TM-ESO Composition	**Predicted Increment (MPa)**	**Experimental Increment (MPa)**
Cu-deficient	-830	-1600
Co-deficient	410	612

In addition to the elastic effect described above, there is an additional chemical effect caused by changes in energy associated with cation-cation interactions, which correlate with changes in elastic modulus [148]. This energy depends on the crystallographic configuration (i.e., nearest neighbors). As the composition changes, crystallographic configurations change, causing bond lengths, and thus, bond energies, to change accordingly. The elastic modulus is strongly associated with bond energy, which can be approximated through bond length [149]. A longer bond length corresponds to a lower bond energy, and vice versa. In the case of a crystalline random solid

solution such as the TM-ESO, the bond length can be approximated by lattice parameter. We used lattice parameters estimated by Rietveld refinement to analyze the changes in the room-temperature elastic modulus for the single-phase equimolar, Co-deficient, and Cu-deficient TM-ESO compositions, as listed in Table 3.5. The elastic modulus increases as the lattice parameter decreases, indicating that a chemical effect contributes to the changes in elastic modulus values as a function of composition observed for the single-phase samples.

Table 3.5: Room-temperature elastic modulus values and corresponding lattice parameters for single-phase equimolar, Co-deficient, and Cu-deficient TM-ESO.

TM-ESO Composition	Elastic Modulus (GPa)	Lattice Parameter (Å)
Equimolar	140	4.2326
Co-deficient	160	4.2312
Cu-deficient	170	4.2307

3.5 Summary

The influence of the entropic phase transformation on the room-temperature mechanical behavior of multiphase TM-ESOs was investigated. Single-phase equimolar samples were prepared through conventional sintering and were heat treated to form Cu-rich tenorite and Co-rich spinel secondary phases. Single-phase Co-deficient and Cu-deficient compositions were also prepared and heat treated to isolate the Cu-rich tenorite and Co-rich spinel secondary phases, respectively, and to study the influence of these secondary phases on mechanical behavior independent of one another. SEM, EDS, and XRD were used to characterize the secondary phase composition, morphology, and distribution in multiphase TM-ESO samples. STEM was used to study how dislocations interact with secondary phase particles inside and outside the deformation zone in multiphase equimolar TM-ESO. Hardness and elastic modulus were measured at room temperature with microindentation and nanoindentation, respectively. The key findings of this investigation are as follows:

1. Equimolar and Co-deficient samples experience an increase in room-temperature hardness after 2 hr of heat treatment and a decrease in hardness after 12 hr of heat treatment. This change in hardness is attributed to a switch in the controlling strengthening mechanism from modulus hardening to Orowan hardening as the Cu-rich tenorite secondary phase particles grow and coarsen.
2. Cu-deficient samples experience a gradual increase in room-temperature hardness from 2 hr to 12 hr of heat treatment, due to a change in the controlling strengthening mechanism from coherency hardening to modulus hardening. This change is attributed to the formation of Co-rich spinel secondary phase particles through the nucleation of nanoparticle precursor phases and eventual transformation into secondary phase particles.
3. The amount of secondary phase influences the room-temperature elastic modulus of TM-ESO, similar to conventional composite materials.
4. Changing the composition influences the room-temperature hardness and elastic modulus of single-phase TM-ESO due to changes in cation-dislocation and cation-cation interaction energies, respectively.

Overall, the entropic phase transformation, which controls the formation of secondary phases, influences the room-temperature mechanical behavior of TM-ESOs. The interactions between dislocations and secondary phase particles play a significant role in the hardness of TM-ESOs. Our analysis of hardness trends indicates that the mechanical behavior of single-phase and multiphase TM-ESO is influenced by solid-solution and precipitation strengthening mechanisms, respectively. Additionally, lattice parameter and cation configuration within the crystal structure influence the elastic modulus of single-phase and multiphase TM-ESOs, respectively. As the phase

transformation of TM-ESOs is reversible, this study shows that the microstructure can be manipulated to tailor the mechanical behavior of TM-ESOs through simple heat treatment.

Chapter 4: High-temperature deformation behavior of entropy stabilized oxides

4.1 Background

At elevated temperatures, crystalline materials exhibit different mechanical behavior than at lower temperatures. To design for use of materials in high-temperature applications, such as thermal barrier coatings or gas turbine engines, their mechanical behavior in such environments must be well understood. Materials often exhibit time-dependent deformation at high temperatures, otherwise known as creep. There are several mechanisms for creep, such as Nabarro-Herring creep, Coble creep, and solute-drag creep. Nabarro-Herring creep is achieved through diffusional mass transport that is driven by a vacancy concentration gradient. Vacancies typically diffuse from areas of high chemical potential to areas of low chemical potential [15]. Nabarro-Herring creep typically dominates at low stress levels and higher temperatures, and results in a change in grain shape, as shown in Fig. 4.1 [15].

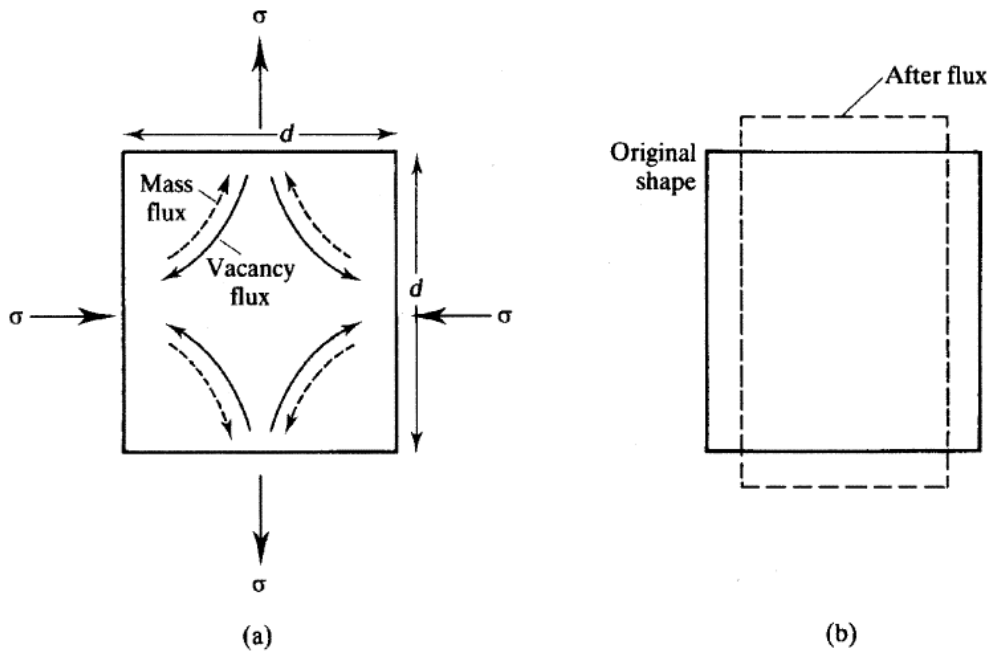

Figure 4.1: Schematic illustrating a) diffusion of vacancies in Nabarro-Herring creep, and b) the resultant grain shape change [15].

Coble creep is also achieved through diffusional mass transport driven by a vacancy concentration gradient, but occurs by diffusion along grain boundaries, as shown in Fig. 4.2 [15]. Coble creep is typically followed by grain boundary sliding, and typically dominates at smaller grain sizes [15].

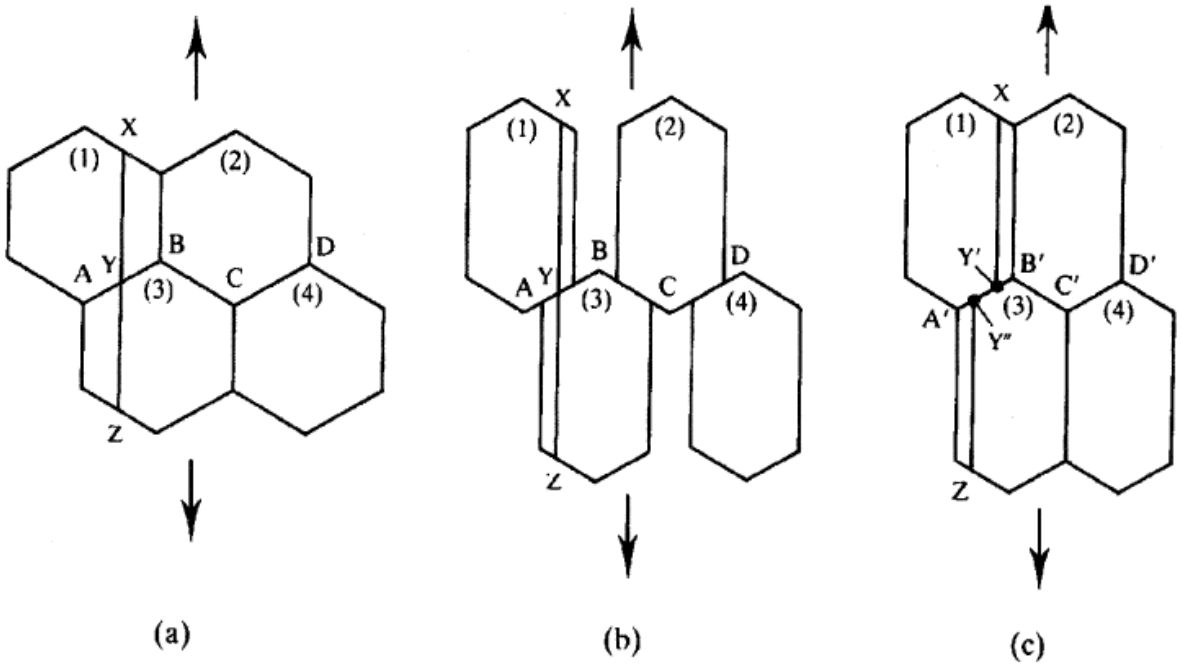

Figure 4.2: Schematic illustrating Coble creep, showing a) four grains prior to Coble creep, b) the shape change of grains in one dimension followed by void formation between grains, and c) the movement of grains by grain boundary sliding [15].

Solute-drag creep is a result of a size misfit between solute atoms and edge dislocations. At high temperatures, when solutes are mobile, they "drag" the dislocations with them. The amount of drag depends on the misfit parameter, solute diffusivity, and solute atom concentration [15].

In addition to creep, a phenomenon known as superplasticity can occur at high temperatures. Superplasticity is a mechanical phenomenon where tensile specimens are capable of elongations on the order of hundreds to thousands percent [150]. Superplastic deformation has many potential applications, such as net shape forming and improved recyclability of materials [150]. Superplasticity is more readily observed in metals and alloy systems but can also occur in ceramics.

In 1986, Wakai *et al*. demonstrated that yttria-stabilized zirconia (YSZ) could be elongated to more than 100% in length at high temperatures, as shown in Fig. 4.3 [151].

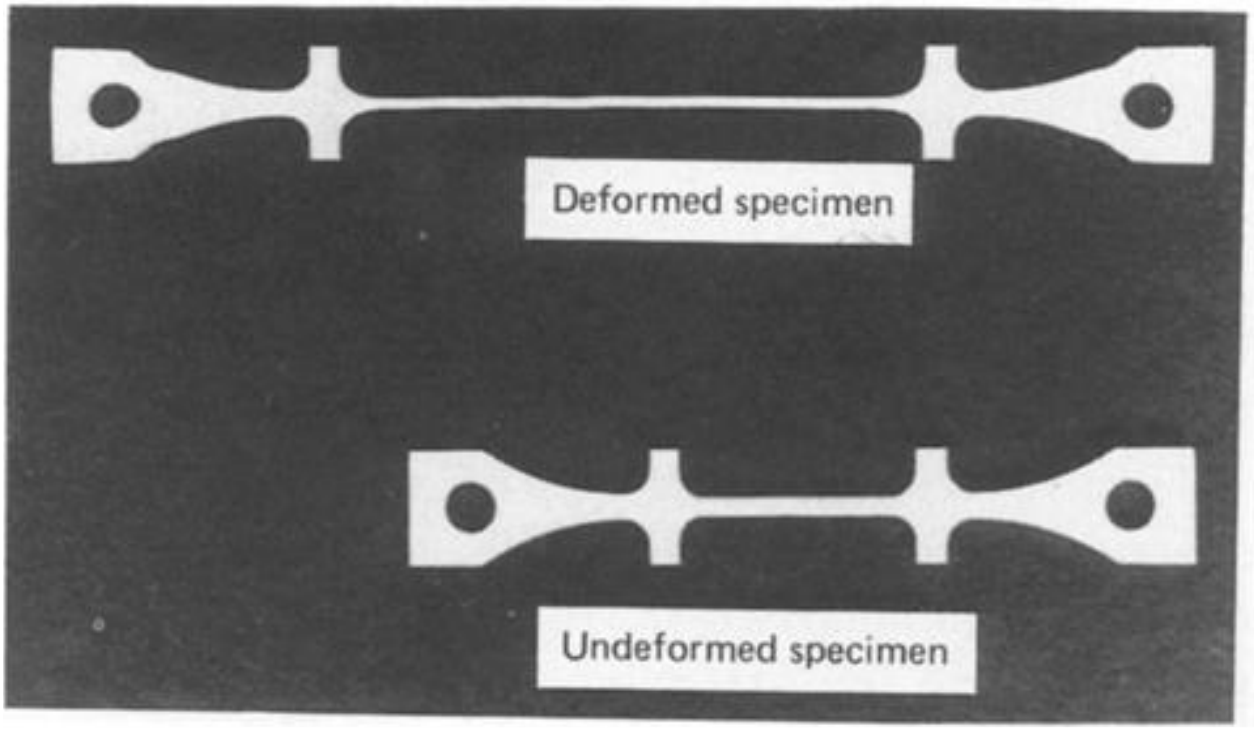

Figure 4.3: Superplastically elongated specimen of yttria-stabilized zirconia, deformed at 1450 °C [151].

Superplastic net shaping of ceramics has also been achieved, as shown in Fig. 4.4 [152].

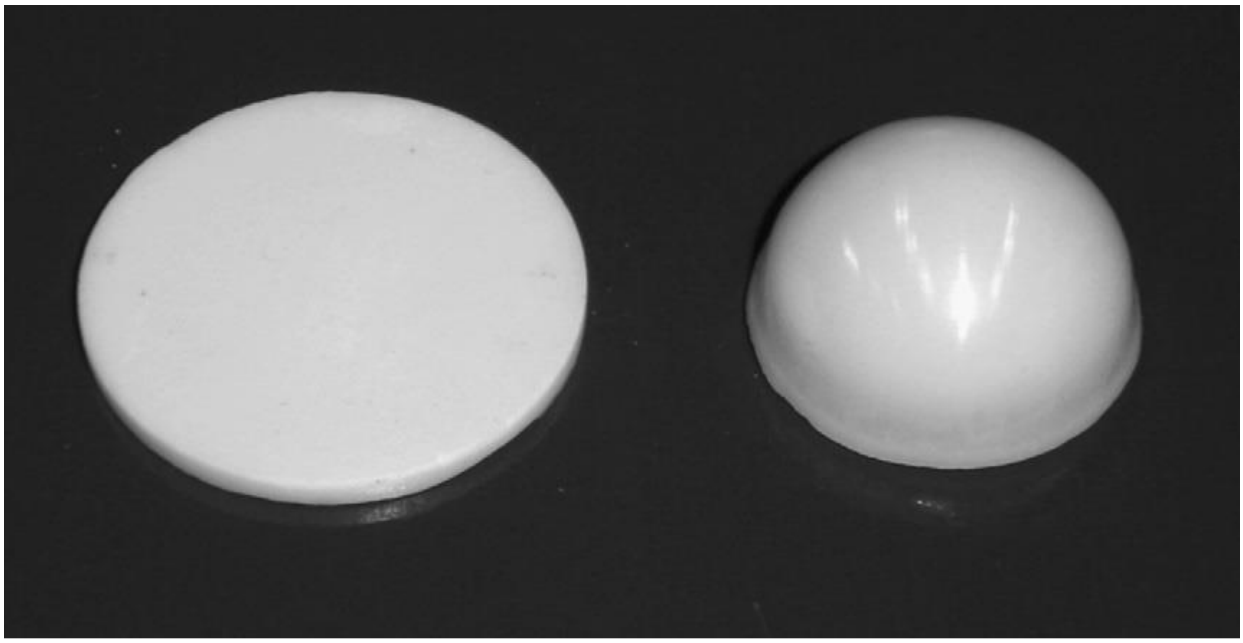

Figure 4.4: Examples of superplastic net-shaped domes of Al^{3+}-doped yttria-stabilized zirconia [152].

The mechanism for superplastic deformation is commonly attributed to grain boundary sliding (GBS), accommodated by diffusion, as proposed by Gifkins and illustrated in Fig. 4.5 [153].

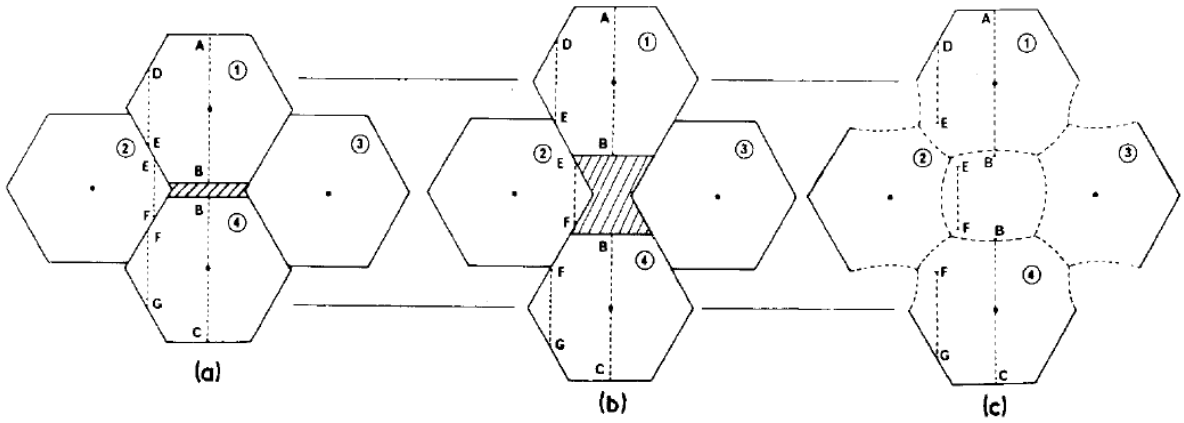

Figure 4.5: Specimen elongation by grain boundary sliding and accommodating of movement of grains from one layer to the next – "emerging grains". (a) After a small amount of deformation, a small, narrow fissure forms; (b) the gap is enlarged and filled by an emerging grain; (c) the grain boundary network adjusts to maintain correct dihedral angles [153].

In this model, as grains slide past one another, a fissure opens, where a grain from the next lower layer slides up to fill that spot. After the grains slide past one another, diffusion occurs at the grain

boundaries and they become curved to maintain dihedral angles, as illustrated in Fig. 4.5c. In an ideal scenario, superplastic deformation is described with the following equation [152]:

$$\dot{\varepsilon} = A\sigma^{n}d^{-p}e^{\left(-Q/RT\right)} \tag{4.1}$$

where $\dot{\varepsilon}$ is strain rate, A is a material constant, σ is applied stress, n is the stress exponent, d is grain size, p is grain size sensitivity, Q is activation energy, T is temperature during deformation, and R is the universal gas constant. Eqn. 4.1 highlights significant relationships in superplastic deformation. Firstly, as grain size decreases, the strain rate increases. Additionally, a decrease in activation energy or an increase in forming temperature also correspond to an increase in the strain rate. The stress exponent n is the inverse of strain rate sensitivity, m, and can be used to quantify a material's resistance to strain localization. Ceramics are considered superplastic at stress exponent values ≤ 3 [152].

The entropic phase transformation in TM-ESOs has several significant features, including reversibility, a wide temperature range, and a dependence on starting microstructure [103, 110]. The reversible phase transformation may allow for reliable, cyclic forming of TM-ESO. The wide temperature range may allow for more controlled forming to achieve desired microstructures. Although the room-temperature mechanical properties of single-phase and multiphase TM-ESO have been investigated (see Chapter 3 and references [127, 154–156]), their high-temperature mechanical behavior has not been analyzed. The objectives of the experiments described in this chapter are to understand the mechanisms for high-temperature deformation of TM-ESO, and to elucidate the role that microstructure and phase composition play in controlling these deformation mechanisms.

4.2 Experimental methods

4.2.1 Synthesis of pre-deformation TM-ESO samples

Equimolar TM-ESO samples were fabricated through solid-state synthesis. Samples were prepared with a range of grain sizes (coarse, fine, and nanocrystalline) and phase states (single-phase, intermediate multiphase, and multiphase), as described below.

For the coarse-grained (target grain size of ~20 μm) and fine-grained (target grain size of ~1 μm) samples, the following procedures were used. The five binary oxide powders of CoO (50 nm, 99.7 wt% purity), CuO (25 – 55 nm, 99.95%), MgO (50 nm, 99.95%), NiO (18 nm, 99.98%), and ZnO (18 nm, 99.95%) (US Research Nanomaterials, Houston, TX, USA) were blended in equimolar amounts in a mortar and pestle. The blended powders were placed in a jar with isopropyl alcohol and ball milled for 12 hr to refine the powders. The powder slurry was extracted from the jar and boiled at 100 °C for 12 hr to evaporate the isopropyl alcohol. The dried powder was ground in a mortar and pestle to remove agglomerates. Spark plasma sintering (SPS) was used to consolidate cylindrical samples that were approximately 14 mm in diameter and 2 mm in height. Two different sintering routes were used to achieve two different grain sizes. For the fine-grained samples, the powder was heated at 900 °C for 10 minutes with a heating rate of 200 °C/min in the SPS. For the coarse-grained samples, the powder was first consolidated in the SPS with the same method, then conventionally sintered in an elevator furnace at 1100 °C for 12 hr and quenched in air. Both processing routes yielded samples that were fully dense and single-phase. Fine-grained samples were heat treated at 700 °C for 2 hr and 12 hr to create intermediate multiphase and multiphase samples, respectively. Coarse-grained samples were heat treated at 700 °C for 12 hr to create multiphase samples.

To produce nanocrystalline samples, the five binary oxide powders were first blended with a mortar and pestle. The powders were then placed in a Pulverisette 7 planetary ball mill (PBM, Fritsch, Idar-Oberstein, Germany) with isopropyl alcohol, and milled for 3 hr. The powder slurry was extracted from the PBM jar and boiled at 100 °C to evaporate the isopropyl alcohol. The dried powder was reacted in an elevator furnace at 900 °C for 20 min to create a powder that was uniformly single-phase. The powder was once again milled in the PBM for 12 hr and flash boiled at 100 °C. The nanocrystalline samples were consolidated through SPS to create cylindrical samples that were 14 mm in diameter and 2 mm in height. To achieve a nanocrystalline grain size of approximately 500 nm, the samples were heated at 700 °C for 10 min with a heating rate of 200 °C in the SPS. Table 4.1 summarizes the different samples prepared for high-temperature compression tests.

Table 4.1: TM-ESO samples for high-temperature compression tests

Sample ID	Grain size	Phase state	Tenorite (at %)	Spinel (at %)
A	Nanocrystalline	Single-phase	0	0
B	Fine-grained	Single-phase	0	0
C	Fine-grained	Intermediate multiphase	6	6
D	Fine-grained	Multiphase	14	10
E	Coarse-grained	Single-phase	0	0
F	Coarse-grained	Multiphase	14	10

4.2.2 High-temperature compression experiments

To carry out high-temperature compression experiments, a custom-built high-temperature mechanical testing system was constructed inside an Instron load frame. Custom compression rods were machined out of Inconel 718. A clamshell furnace was used to heat the samples, and the compression rods and Instron load frame were kept cool through two water-cooled adapters that attached to the compression rods. A thermocouple was inserted into the center of the furnace to

track the temperature during the compression experiments. The custom high-temperature mechanical testing system is shown in Fig. 4.6.

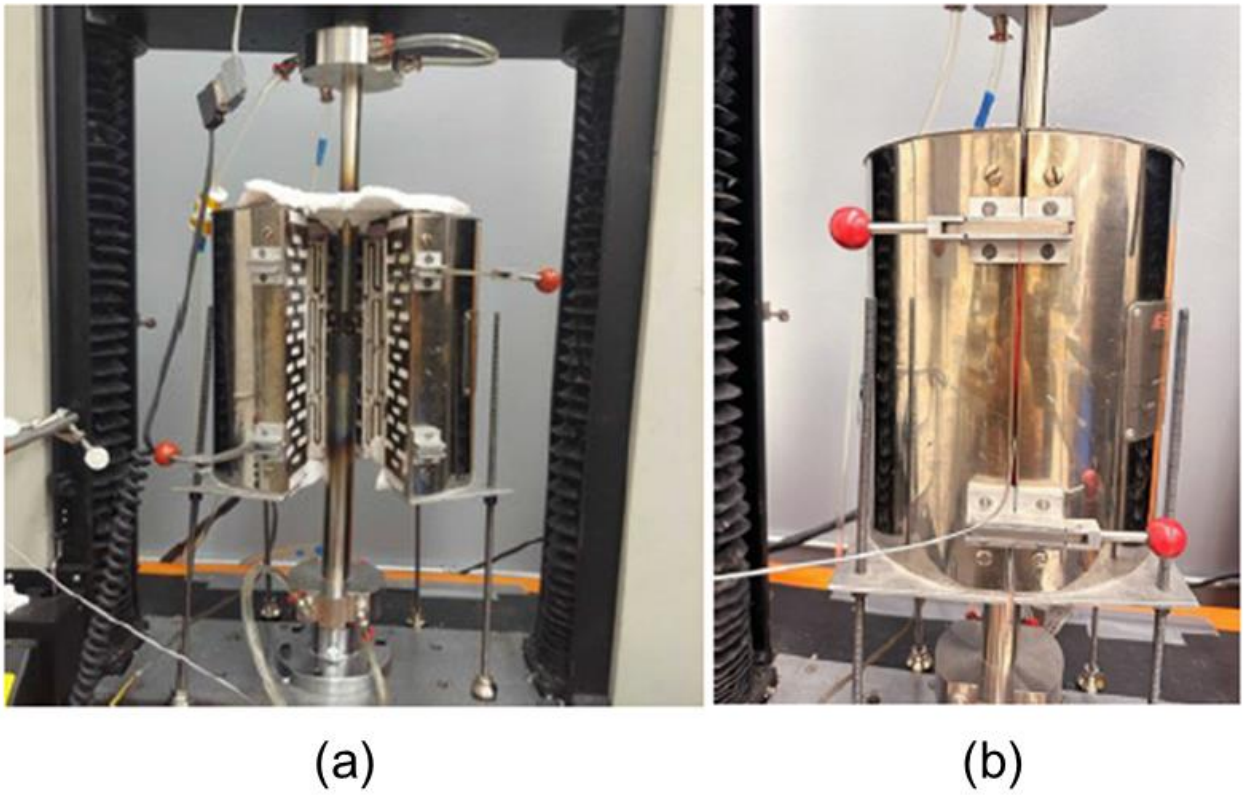

Figure 4.6: Photographs of the custom-built high-temperature mechanical testing system: a) The system at room temperature being prepared for an experiment; b) The system during an experiment at 700 °C. Note the thermocouple inserted into the furnace.

Single-phase and multiphase samples were each compressed at fixed deformation temperatures ranging from 600 °C to 850 °C in 50 °C increments at loads of 13, 20, and 31 N (with the exception of Sample A, which was deformed at temperatures up to 700 °C to avoid grain growth at high temperatures). Samples were held at each load for 10 min. The samples were deformed continuously with increasing loads to generate a strain-time curve for each compression experiment, as shown in Fig. 4.7a. The curves generated during each compression experiment can be found in Appendix B.

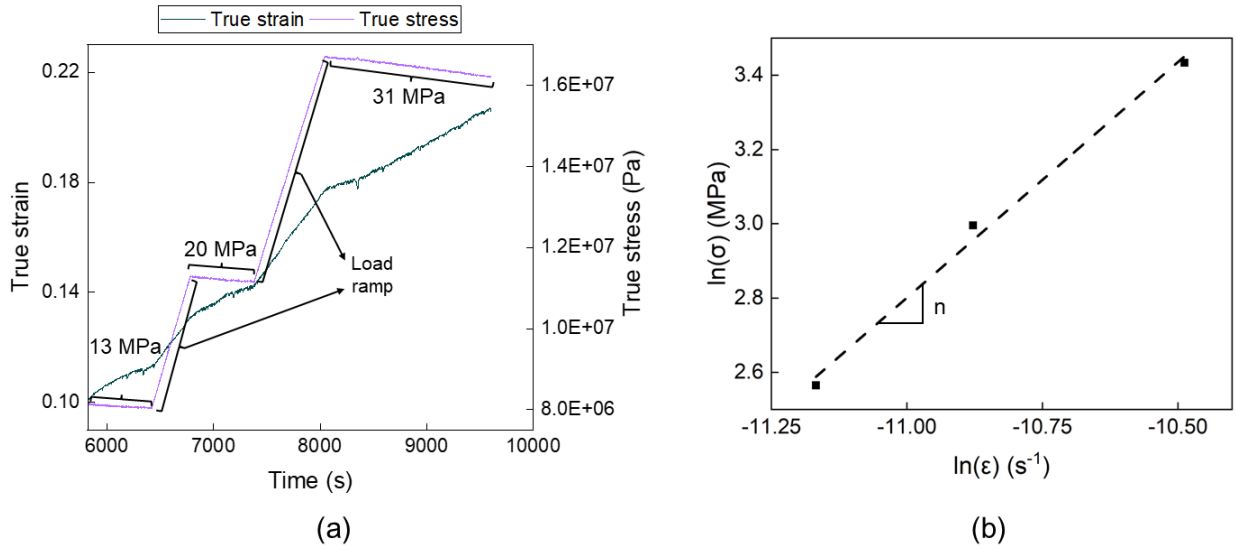

Figure 4.7: a) A representative true strain vs. time graph that was generated during high-temperature compression experiments; b) A representative plot of $\ln(\sigma)$ vs. $\ln(\dot{\varepsilon})$ that was used to generate the stress exponent n. The line represents the linear best fit from which the slope was extracted.

For each experiment, strain rates were measured for each load and used to calculate the stress exponent. Measured strain rates can be found in Appendix B. As deformation temperature and grain size were held constant for each set of high-temperature compression experiments, Eqn. 4.1 can be simplified as follows to calculate the stress exponent [150]:

$$\dot{\varepsilon} = A\sigma^n \tag{4.2}$$

where $\dot{\varepsilon}$ is the strain rate, A is a constant, σ is the applied stress, and n is the stress exponent. Values of $n \leq 3$ indicate superplastic deformation, while $n < 1$ indicates viscous-like flow. Evaluation of n is critical for determining the nature of the deformation behavior and whether a material deforms superplastically. The stress exponent was calculated by taking the slope of $\ln(\dot{\varepsilon})$ vs $\ln(\sigma)$, as shown in Fig. 4.7b.

4.2.3 Characterization of grain size and secondary phases

Samples B, C, and D were characterized with SEM, XRD, and EDS before and after deformation at 700 °C. The deformation temperature of 700 °C was selected for characterization

as that is the temperature at which the highest amount of secondary phase is expected to form for TM-ESO. The fine-grained samples were selected for characterization because the secondary phase formation has not been previously studied in detail for this grain size, whereas for nanocrystalline and coarse-grained samples, secondary phase composition, crystal structure, concentration, and morphology have been previously well documented (see Chapter 3, and references [110, 112, 156, 157]).

SEM was used to observe fracture surfaces of the samples to understand how deformation affected the grain morphology. Fracture surfaces were prepared for SEM analysis by sputter coating with 3 nm of iridium using an ACE600 sputter coating machine (Leica Microsystems, Wetzlar, Germany). The fracture surfaces were imaged with a Magellan 400 XHR SEM (FEI, Hillsboro, OR, USA), using an accelerating voltage of 5 kV and a current of 50 pA. The average grain size was calculated from the fracture surface micrographs by measuring the diameter of approximately 250 grains with the FIJI/ImageJ software [62].

XRD and Rietveld refinement were used to determine if a phase transformation occurred during high-temperature deformation, and how much secondary phase formed during the high-temperature deformation experiments. XRD was performed with a SmartLab X-ray Diffractometer (Rigaku, Tokyo, Japan), with a 2θ range of 30° to 80°. Rietveld refinement was performed on the acquired XRD data using the Maud software [131] to estimate the relative atomic fraction of the primary rocksalt, Cu-rich tenorite, and Co-rich spinel phases for each test condition.

EDS mapping was used to observe the morphology of the secondary phases in the fine-grained TM-ESO before and after high-temperature deformation. Samples were prepared for EDS analysis by polishing with 800 grit and 1200 grit SiC pads (Allied High-Tech Products, Inc; Compton, CA, USA), then with 6 μm and 1 μm diamond suspensions (PACE Technologies, Tucson, AZ, USA).

The polished samples were mounted onto SEM stubs with colloidal silver paste (Ted Pella Inc., Redding, CA, USA) and sputter coated with 3 nm of iridium. EDS was performed in a GAIA SEM-FIB microscope (Tescan, Brno, Czechia) using a silicon drift detector with an area of 150 mm^2 (Oxford Instruments, Abingdon, UK). A working distance of 5 mm and an accelerating voltage of 5 kV were used.

4.3 Results

4.3.1 Microstructure and secondary phase evolution

Samples B – D all experienced negligible grain growth during high-temperature deformation at 700 °C, as seen in Fig. 4.8, with average grain sizes ranging from 0.9 to 1.3 μm before deformation, and from 1.2 to 1.5 μm after deformation. Additionally, the grains maintained an equiaxed microstructure both before and after deformation.

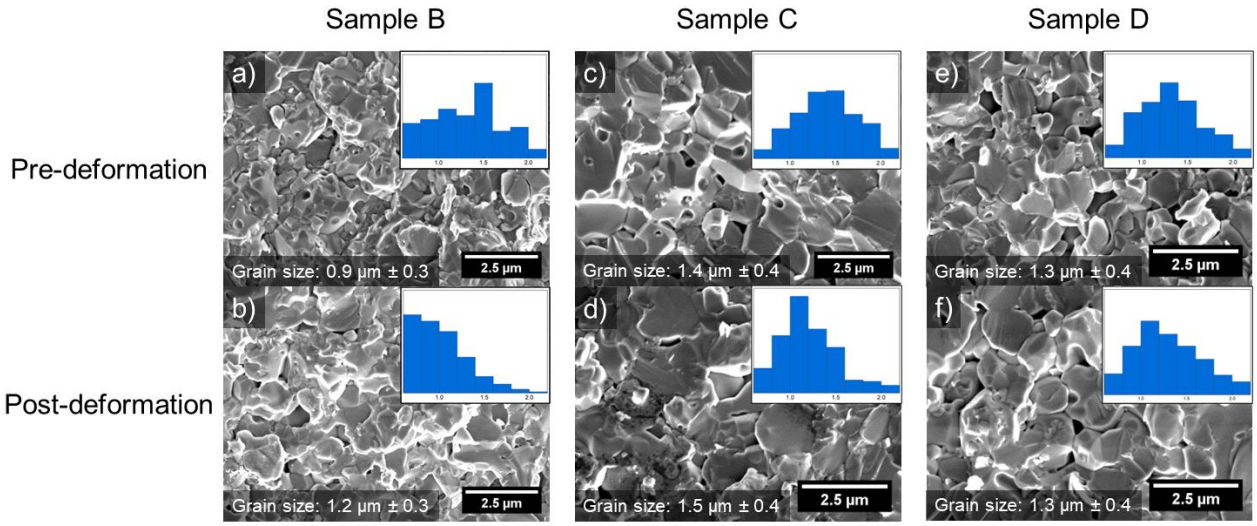

Figure 4.8: Fracture surfaces and grain size for fine-grained samples: (a) – (b) Sample B before and after deformation, (c) – (d) Sample C before and after deformation, and (e) – (f) Sample D before and after deformation. The insets are histograms of the grain size distribution for each sample, ranging from 0.6 μm to 2.2 μm, with counts up to 80. The samples were deformed at 700 °C.

XRD results, shown in Fig. 4.9, indicate that some phase transformation does occur during the high-temperature deformation process. For Sample B, Cu-rich tenorite forms during

high-temperature deformation. For Sample C, more Cu-rich tenorite formed during high-temperature deformation. For Sample D, additional Cu-rich tenorite and Co-rich spinel formed during high-temperature deformation as indicated by the increase in prominence and additional formation of peaks. In previous literature, it has been assumed that the maximum amount of secondary phase forms after 12 hr of heat treatment [110]. Notably, additional secondary phases formed when a load was applied to Sample D at elevated temperatures, as shown in Fig. 4.9. Rietveld refinement results shown in Table 4.2 support the findings in Fig. 4.9. This formation of additional secondary phase(s) under an applied load is significant because the mechanical behavior of TM-ESO could potentially change as the phase transformation occurs when used in high-pressure, high-temperature applications.

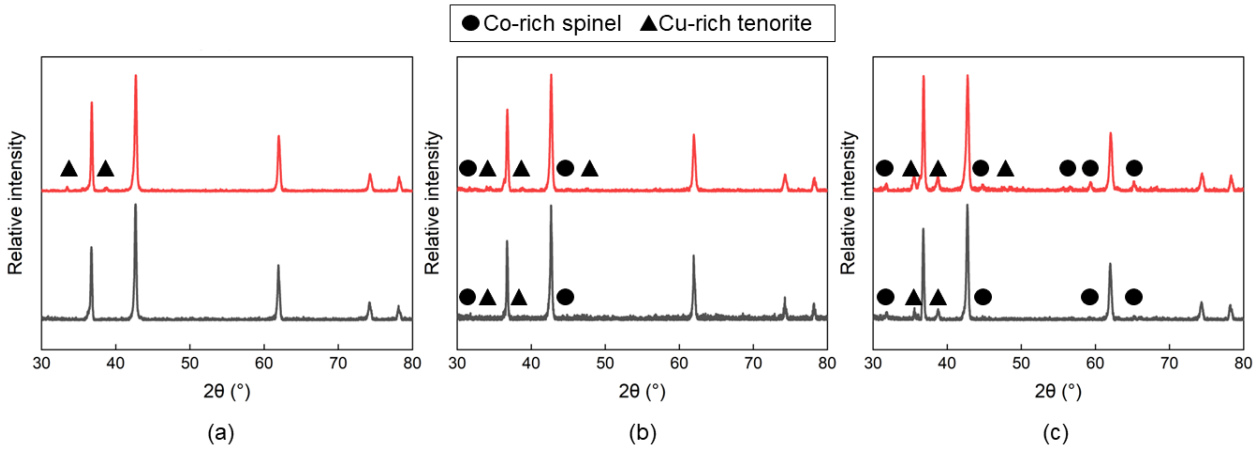

Figure 4.9: XRD results for fine-grained TM-ESO samples that were: a) single-phase (Sample B), b) heat-treated for 2 hr (Sample C), and c) heat-treated for 12 hr (Sample D), both before and after high-temperature deformation (deformation temperature of 700 °C). In all plots, the bottom black spectra represent the pre-deformed condition, and the top red spectra represent the post-deformed condition.

Table 4.2: Rietveld refinement results for atomic fraction of secondary phases that formed in fine-grained TM-ESO (Samples B, C, and D) before and after deformation at 700 °C.

Sample ID	Cu-rich Tenorite (at %)		Co-rich Spinel (at %)	
	Pre-deformation	Post-deformation	Pre-deformation	Post-deformation
B	0	2	0	0
C	6	7	6	6
D	14	16	10	11

As shown in the EDS maps in Fig. 4.10, in the fine-grained TM-ESO samples, the Cu-rich tenorite secondary phase forms a layer around the grains at the grain boundaries. In contrast, in the coarse-grained samples, the Cu-rich tenorite secondary phase forms as needles in the grain and at the grain boundary, as shown previously in Chapter 3 (see Fig. 3.3). In nanocrystalline samples, the Cu-rich tenorite secondary phase encompasses entire grains [110].

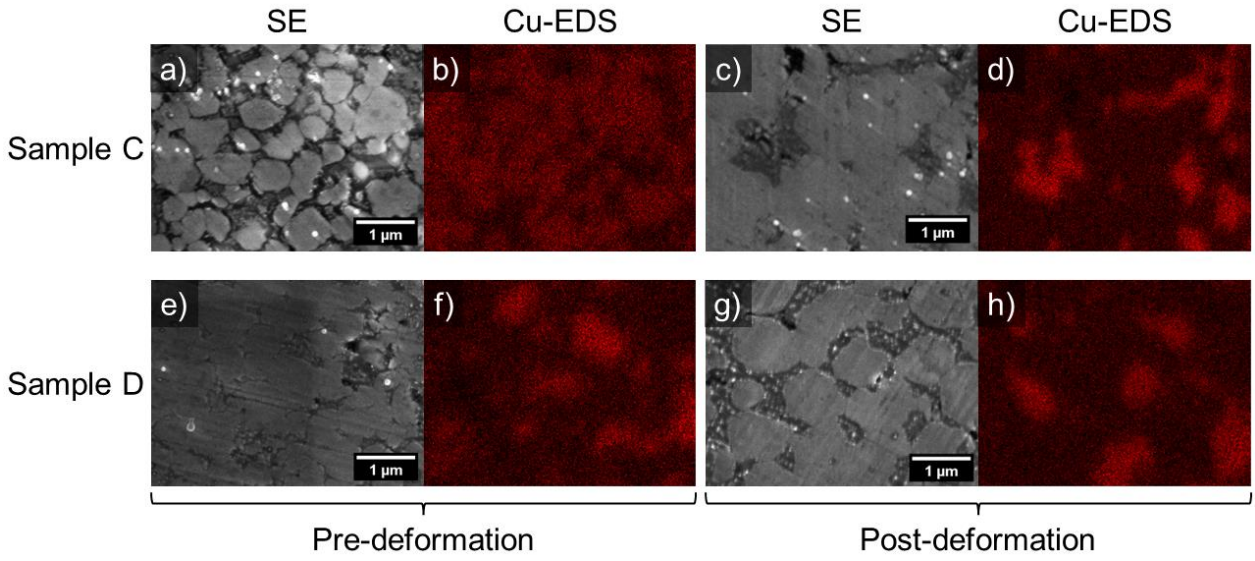

Figure 4.10: Secondary electron images and Cu-EDS maps of fine-grained samples: (a) – (b) Sample C before deformation, (c) – (d) Sample C after deformation, (e) – (f) Sample D before deformation, and (g) – (h) Sample D after deformation. All samples were deformed at 700 °C.

4.3.2 Stress exponent calculations

The calculated stress exponent values for Samples A–F, after high-temperature deformation testing at select temperatures in the range of 600 °C to 850 °C are shown in Fig. 4.11.

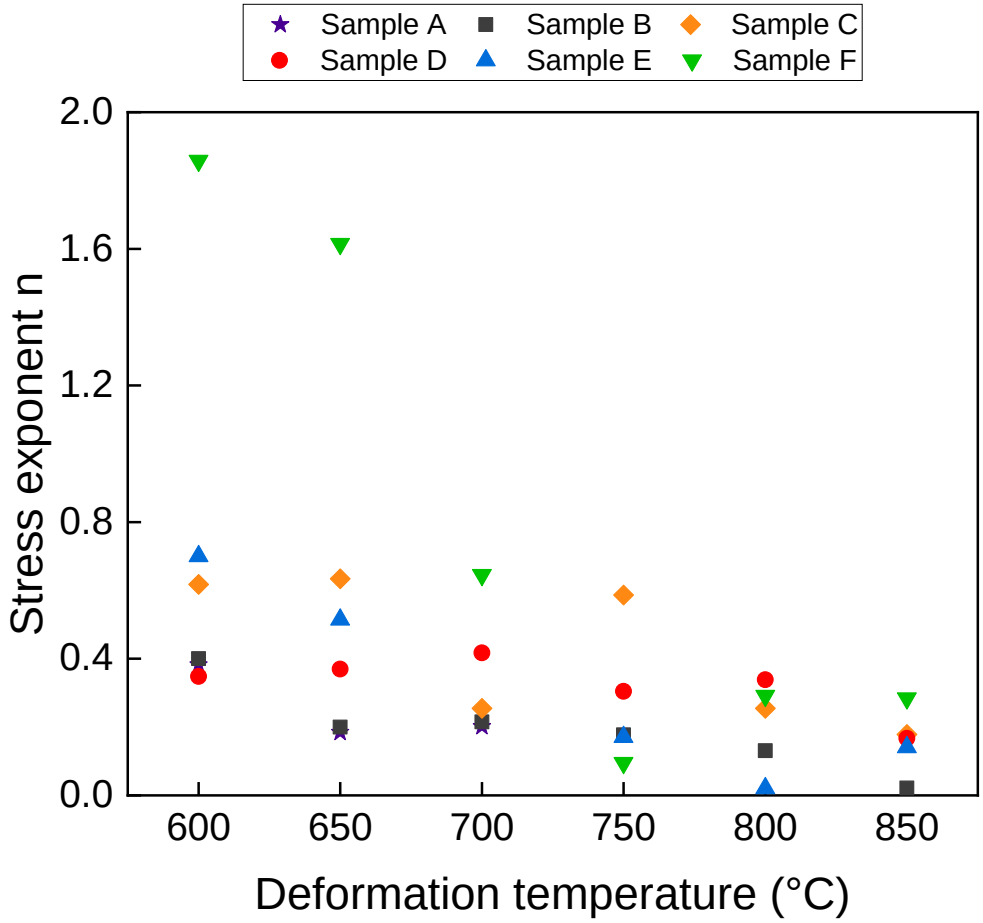

Figure 4.11: Calculated stress exponent values for nanocrystalline (Sample A), fine-grained (Samples B, C, and D), and coarse-grained (Samples E and F) samples deformed over a range of temperatures.

The calculated stress exponents for fine-grained materials, Sample B (single-phase) and Sample D (multiphase), after high-temperature deformation at select temperatures in the range of 600 °C and 850 °C are shown in Fig. 4.12. The stress exponent values shown in Fig. 4.12 fall below 0.4, indicating superplastic deformation with viscous-like flow [158].

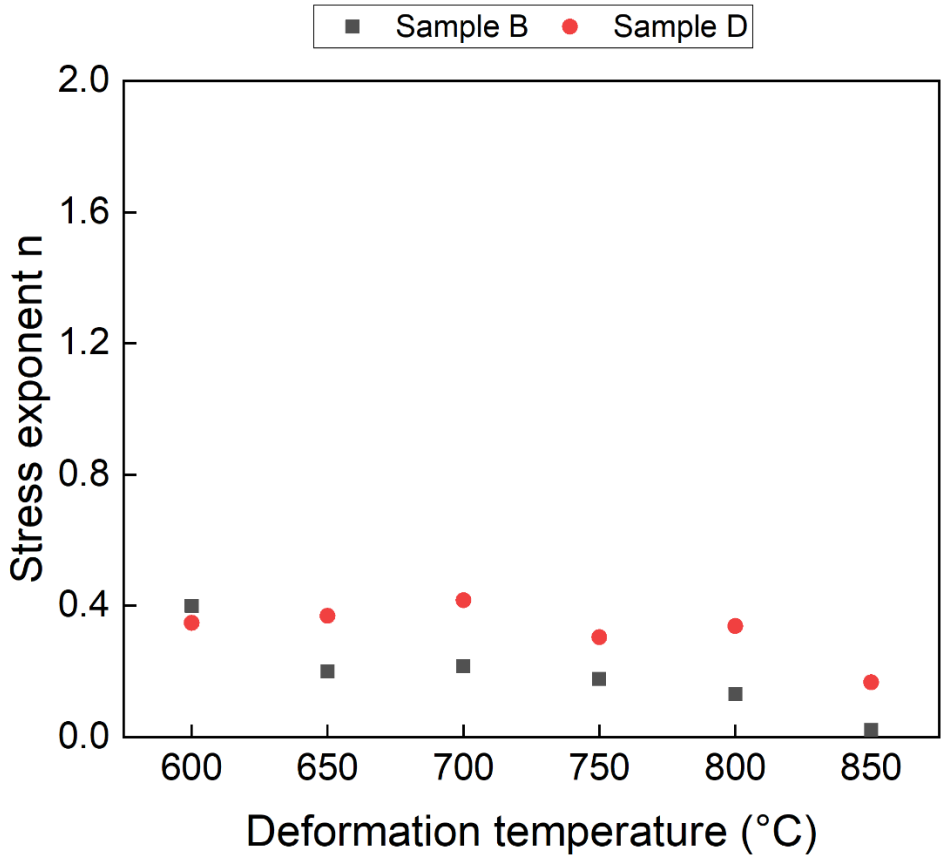

Figure 4.12: Calculated stress exponent values for fine-grained TM-ESOs (Samples B and D) deformed over a range of deformation temperatures.

The calculated stress exponent values for coarse-grained materials, Sample E (single-phase) and Sample F (multiphase), after high-temperature deformation at select temperatures in the range of 600 °C to 850 °C are shown in Fig. 4.13.

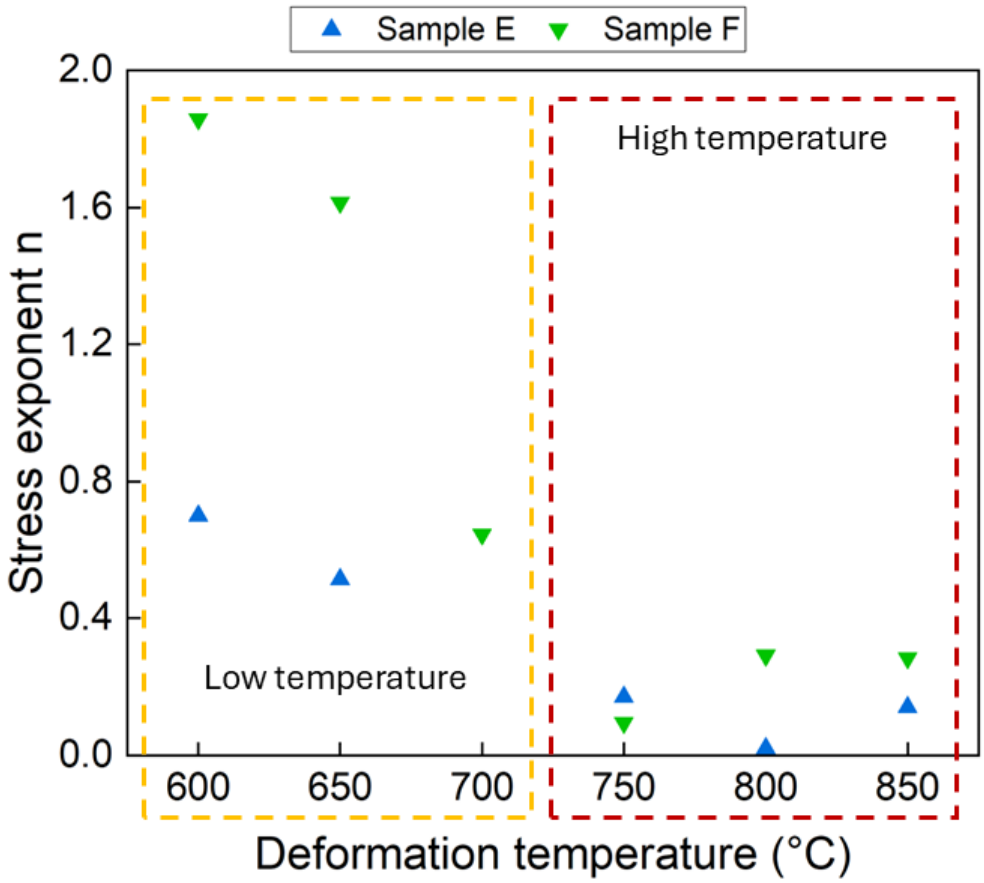

Figure 4.13: Stress exponent values calculated for coarse-grained TM-ESO (Samples E and F). The graph has been split into two deformation temperature regimes: low temperature (ranging from 600 – 700 °C), and high temperature (ranging from 750 – 850 °C).

Overall, the stress-exponent values shown in Fig. 4.13 are less than 2, indicating superplastic deformation. Notably, the stress exponent values differ from the low-temperature regime to the high-temperature regime. It is also noted that the-coarse-grained TM-ESOs have higher overall stress exponent values (Fig. 4.13) than the fine-grained TM-ESOs (Fig. 4.12).

4.4 Discussion

As shown in Fig. 4.11, the results for Sample A (nanocrystalline) closely resemble those for Sample B. Additionally, Sample A was only tested at 3 temperatures, and its grain size sensitivity is very similar to those for Samples B, C, and D (Fig. B.4 in Appendix B). To simplify analysis and explanation of possible high-temperature deformation mechanisms, and given its similarity in

behavior to Sample B, Sample A is excluded from the following discussion. Sample C, with an intermediate concentration of secondary phases, is also excluded to simplify the comparison between single-phase and multiphase samples. Thus, the samples discussed below are Sample B (fine-grained, single-phase), Sample D (fine-grained, multiphase), Sample E (coarse-grained, single-phase), and Sample F (coarse-grained, multiphase). The following discussion is also limited to the stress exponent. Analysis of variables such as activation energy and grain size sensitivity can be found in Appendix B, as well as data from additional experiments at higher load and for longer times, which were deemed outside the scope of this analysis.

4.4.1 High-temperature deformation of fine-grained TM-ESO

As shown in Fig. 4.9, the lack of grain growth and change in grain shape in fine-grained TM-ESO indicate that creep mechanisms like Nabarro-Herring creep and Coble creep do not take place during the deformation of fine-grained TM-ESO, as both mechanisms involve a change in the grain shape [15]. Thus, the dominant mechanism for deformation in the fine-grained TM-ESO appears to be grain boundary sliding, leading to the superplastic deformation indicated by the low stress exponent values. Sample D has slightly higher stress exponents than Sample B (greater by approximately 0.02 across the range of deformation temperatures), likely due to the presence of secondary phases at the grain boundaries [159–161]. For Samples B and D, there is a slight decrease in stress exponent as the deformation temperature increases. The slight decrease in stress exponent with the increase in deformation temperature is likely due to an enhancement in grain boundary sliding at the deformation temperature increases [158]. Lastly, the stress exponents for fine-grained samples (Fig. 412) are smaller than those of the coarse-grained samples in the low-temperature regime (Fig. 4.13). This is likely because as grain size decreases, grain boundary sliding is enhanced due to the presence of overall greater grain boundary area [158].

4.4.2 High-temperature deformation of coarse-grained TM-ESO

In the low-temperature regime, Sample F has higher stress exponent values than Sample E. The increase in stress exponent in the multiphase sample is likely due to the presence of secondary phase particles at the grain boundary. Dupuy *et al*. has previously shown with FIB-tomography that in coarse-grained TM-ESOs, Cu-rich tenorite and Co-rich spinel secondary phases form networks of needles and platelets at grain boundaries, as shown in Fig. 4.14 [157].

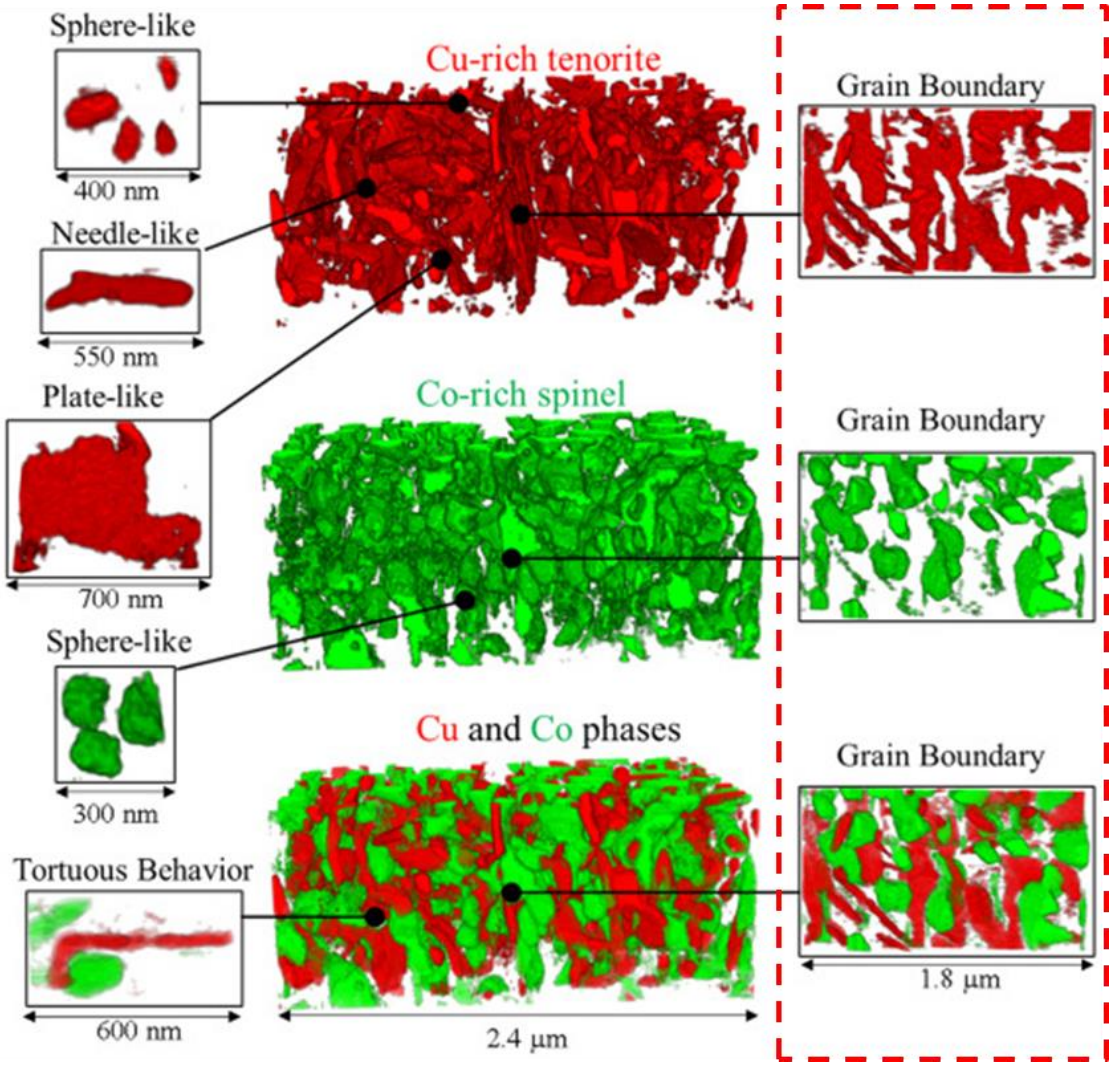

Figure 4.14: FIB-tomography results showing secondary phase particles in coarse-grained TM-ESOs. The red particles represent the Cu-rich tenorite, and the green particles represent the Co-rich spinel. The section on the right highlight in the red box indicates the secondary phase morphology in the grain boundary. Figure adapted from [157]

The presence of secondary phases at the grain boundaries of the coarse-grained TM-ESO likely causes a grain boundary pinning mechanism. Grain boundary pinning is a phenomenon where precipitates or particles at grain boundaries can pin them, effectively inhibiting their motion [162]. The pinning effect can prevent grain growth from occurring and inhibit grain boundary sliding. There are two mechanisms for how grain boundary pinning can occur. The first is a pass-through mechanism, where the grain boundary goes directly through the particle [163]. The second is an enveloping mechanism, where the grain boundary bends around and envelops the particle, eventually bypassing it [164]. Both mechanisms require an energy contribution for the grain boundary to bypass the particle.

There is a limit to the effectiveness of particles at pinning grain boundaries. Typically, the larger the particle, the less effective it is at pinning grain boundaries. Past a critical particle size, the particle will no longer be able to pin the grain boundaries. The critical particle size can be determined with the following equation [165]:

$$r = \frac{D \cdot f^{1/3}}{3.6} \tag{4.3}$$

where r is the size of secondary phase particles, D is the average grain size, and f is the volume fraction of secondary phase. For a grain size of 20 μm, the $r_{tenorite}$ is approximately 2.9 μm, and r_{spinel} is approximately 2.6 μm. The particle radius of both Cu-rich tenorite and Co-rich spinel in coarse-grained TM-ESO are on the order of 0.5 – 1 μm and 0.3 μm, respectively [110, 112]. Both particle radius values fall below the critical particle radius for their respective secondary phases, indicating that they should be effective in pinning grain boundaries in coarse-grained TM-ESO, thereby limiting grain boundary sliding and causing an increase in the stress exponent values.

Although Sample D has slightly higher stress exponent values than Sample B, the difference between the stress exponent values for Samples E and F is more exaggerated. This difference in

stress exponent between fine-grained and coarse-grained samples is likely because the secondary phases take on discrete particle shapes in the coarse-grained samples, instead of forming layers at the grain boundaries, as observed in the fine-grained samples.

In the high-temperature regime shown in Fig. 4.13, the stress exponent values for both Samples E and F drop to below 0.4 and remain constant, in a state very similar to that for the stress exponent values of Samples B and D. At these higher deformation temperatures, it is likely that a creep mechanism is activated, assisting the grain boundary sliding. Two creep mechanisms were considered: Nabarro-Herring creep (which is common at high temperatures), and solute-drag creep (which is caused by dislocation motion) [15]. The strain rate for each creep mechanism was calculated and compared to the strain rates of $10^{-6} - 10^{-5}$ s^{-1} that were measured for the coarse-grained TM-ESOs in the high-temperature regime. Strain rates of $10^{-6} - 10^{-5}$ measured for TM-ESOs under high-temperature compression are on the same order of magnitude as those for Al_2O_3 [166], YSZ [166], and MgO [167] deformed under similar conditions. The following equation was used to calculate the strain rate $\dot{\varepsilon}_{NH}$ for Nabarro-Herring creep [15]:

$$\dot{\varepsilon}_{NH} = A_{NH}\left(\frac{D_L}{d^2}\right)\left(\frac{\sigma\Omega}{kT}\right) \tag{4.4}$$

where A_{NH} is a constant, D_L is the diffusivity coefficient (m^2/s), d is grain size (m), σ is load (J/m^3), Ω is atomic volume (m^3/mol), k is the Boltzmann's constant (J/mol·K), and T is deformation temperature (K). The strain rates calculated for Nabarro-Herring creep are on the order of 10^{-8} -10^{-7} s^{-1}. The following equation was used to calculate strain rate $\dot{\varepsilon}_{SD}$ for solute-drag creep [15]:

$$\dot{\varepsilon}_{SD} = A_{SD}\left(\frac{D_{sol}}{b^2}\right)\left(\frac{\sigma\Omega}{kT}\right)\left(\frac{\sigma}{G}\right)^2 \tag{4.5}$$

where A_{SD} is a constant, D_{sol} is a diffusivity coefficient (m^2/s), b is the Burger's vector (m), and G is the shear modulus (J/m^3). The strain rates calculated for solute-drag creep were on the order of $10^{-6} – 10^{-5}$ s^{-1}, which roughly matches the strain rates measured for coarse-grained TM-ESOs in the high-temperature regime (Fig. 4.13) and other oxide ceramics [166, 167]. Given the significant dislocation activity that occurs in coarse-grained TM-ESOs (see Chapter 3, and references [127, 154–156]), it is likely that during high-temperature deformation of coarse-grained TM-ESOs in the high-temperature regime, solute-drag creep is activated and accommodates grain boundary sliding that is otherwise inhibited by grain boundary pinning by secondary phase particles [127].

4.4 Summary

The influence of deformation temperature, microstructure, and phase state on the high-temperature deformation of TM-ESO was investigated. Single-phase and multiphase fine-grained and coarse-grained TM-ESO samples were prepared through spark plasma sintering and heat treatment. High-temperature compression experiments were conducted with applied loads of 13 N, 20 N, and 31 N at fixed deformation temperatures ranging from 600 °C to 850 °C in 50 °C increments. XRD, SEM, and EDS were used to analyze the microstructure and phase composition of fine-grained single-phase and multiphase TM-ESOs before deformation, and after deformation at 700 °C. Stress exponents were extracted from the strain-time curves that were generated during high-temperature deformation experiments. The key findings of this investigation are as follows:

1. During high-temperature compression of fine-grained TM-ESOs, grain size and morphology do not change, yet additional formation of secondary phases is observed.
2. The secondary phase in fine-grained TM-ESO forms a layer around the grain, as opposed to discrete particles within the particle, and in the grain boundaries in coarse-grained TM-ESO.

3. The single-phase and multiphase fine-grained TM-ESO samples had stress exponent values in the range between 0.1 and 0.4, with a slight decrease in stress exponent value as the deformation temperature increased, likely due to an enhancement in grain boundary sliding. The low stress exponent values indicate superplastic deformation.
4. At lower deformation temperatures (e.g., between 600 °C and 700 °C), the multiphase TM-ESO had stress exponent values between 0.7 and 1.8, and the single-phase TM-ESO had stress exponent values between 0.5 and 0.8. The increase in stress exponent value with the presence of secondary phases is likely due to grain boundary pinning by secondary phase particles at the grain boundary, which inhibits grain boundary sliding.
5. At higher deformation temperatures (e.g., between 750 °C and 850 °C), the multiphase and single-phase TM-ESO stress exponent values decrease and remain relatively constant, likely due to the activation of solute-drag creep.

Fine-grained TM-ESOs deform superplastically across a wide temperature range. In coarse-grained TM-ESOs, secondary phases can be used to pin grain boundaries and inhibit deformation of the TM-ESOs up to a certain temperature. Overall, this work demonstrates that the microstructure and phase composition can be manipulated to control the high-temperature deformation behavior of TM-ESOs.

Chapter 5: Conclusions and recommendations for future work

The experiments summarized in this dissertation demonstrate that unconventional methods of designing microstructures can be used to tailor the mechanical behavior of polycrystalline metal and ceramic materials to control their mechanical deformation behavior. Each chapter is summarized below, along with recommendations for future work.

5.1 Conclusions to Chapter 2

The effects of ultrasonic vibration (UV) on melt pool evolution in directed energy deposition (DED) of 316L stainless steel single-tracks and cubes were explored. For the first time, *in situ* high-speed imaging was utilized to analyze particle collisions with the melt pool surface for ultrasonic vibration-assisted (UV-A) and non-UV-A single-track depositions. *In situ* thermal imaging was also used to track the melt pool thermal profiles during UV-A and non-UV-A deposition of higher layers in bulk cubic samples. The use of *in situ* imaging techniques allowed for the collection of robust quantitative data, which were key to elucidating the effects of UV on the thermal and spatial evolution of the melt pool during UV-A DED. Using optical microscopy, SEM, and EBSD, the microstructures and porosity in the as-built bulk samples were extensively characterized. The specific findings of this investigation are as follows:

1. An increase in melt pool temperature and dimensions were observed during UV-A DED due to the combined effects of acoustic cavitation, ultrasound absorption, and acoustic streaming.
2. The particle residence time on the melt pool surface was reduced by approximately half, and wettability of injected particles into the melt pool surface improved, due to a decrease in surface tension caused by UV.

3. The cooling rate increases and dendritic arm spacing decreases during UV-A DED because of enhanced mixing in the melt pool caused by acoustic streaming.
4. Fewer lack-of-fusion pores were observed in UV-A cube samples because of an increase in melt pool dimensions and temperature. However, residual nanoscale acoustic cavitation bubbles are trapped as gas pores at grain boundaries during solidification.
5. An equiaxed-to-columnar grain transition is observed in UV-A cube samples because effects of UV on the melt pool diminish as the build height increases due to the attenuation of ultrasonic waves over an increasing wave propagation distance.

Overall, the findings indicate that the application of UV impacts the melt pool such that it solidifies with refined microstructures and fewer defects during DED processing. However, the UV effects diminish with build height. In the future, these limitations must be considered, as large or complex geometries may reduce the propagation of ultrasonic waves into the melt pool. A means of keeping the wave amplitude constant should be considered, either by tuning the wave frequency *in situ*, or by applying UV with a top-down approach.

5.2 Conclusions to Chapter 3

The influence of the entropic phase transformation on the room-temperature mechanical behavior of multiphase transition metal entropy stabilized oxides (TM-ESOs) was investigated. Single-phase equimolar samples were prepared through conventional sintering and were heat treated to form Cu-rich tenorite and Co-rich spinel secondary phases. Single-phase Co-deficient and Cu-deficient compositions were also prepared and heat treated to isolate the Cu-rich tenorite and Co-rich spinel secondary phases, respectively, and to study the influence of these secondary phases on mechanical behavior independent of one another. Scanning electron microscopy (SEM), energy dispersive spectroscopy (EDS), and X-ray diffraction (XRD) were used to characterize the

secondary phase composition, morphology, and distribution in multiphase TM-ESO samples. STEM was used to study how dislocations interact with secondary phase particles inside and outside the deformation zone in multiphase equimolar TM-ESO. Hardness and elastic modulus were measured at room temperature with microindentation and nanoindentation, respectively. The key findings of this investigation are as follows:

1. Equimolar and Co-deficient samples experience an increase in room-temperature hardness after 2 hours of heat treatment and a decrease in hardness after 12 hours of heat treatment. This change in hardness is attributed to a switch in the controlling strengthening mechanism from modulus hardening to Orowan hardening as the Cu-rich tenorite secondary phase particles grow and coarsen.
2. Cu-deficient samples experience a gradual increase in room-temperature hardness from 2 hours to 12 hours of heat treatment, due to a change in the controlling strengthening mechanism from coherency hardening to modulus hardening. This change is attributed to the formation of Co-rich spinel secondary phase particles through the nucleation of nanoparticle precursor phases and eventual transformation into secondary phase particles.
3. The amount of secondary phase influences the room-temperature elastic modulus of TM-ESO, similar to conventional composite materials.
4. Changing the composition influences the room-temperature hardness and elastic modulus of single-phase TM-ESO due to changes in cation-dislocation and cation-cation interaction energies, respectively.

Overall, the entropic phase transformation, which controls the formation of secondary phases, influences the room-temperature mechanical behavior of TM-ESOs. The interactions between dislocations and secondary phase particles play a significant role in the hardness of TM-ESOs. Our

analysis of hardness trends indicates that the mechanical behavior of single-phase and multiphase TM-ESO is influenced by solid-solution and precipitation strengthening mechanisms, respectively. Additionally, lattice parameter and cation configuration within the crystal structure influence the elastic modulus of single-phase and multiphase TM-ESOs, respectively. As the phase transformation of TM-ESOs is reversible, this study shows that the microstructure can be manipulated to tailor the mechanical behavior of TM-ESOs through simple heat treatment.

5.3 Conclusions to Chapter 4

The influence of deformation temperature, microstructure, and phase state on the high-temperature deformation of TM-ESO was investigated. Single-phase and multiphase fine-grained and coarse-grained TM-ESO samples were prepared through spark plasma sintering and heat treatment. High-temperature compression experiments were conducted with applied loads of 13 N, 20 N, and 31 N at fixed deformation temperatures ranging from 600 °C to 850 °C in 50 °C increments. XRD, SEM, and EDS were used to analyze the microstructure and phase composition of fine-grained single-phase and multiphase TM-ESOs before deformation, and after deformation at 700 °C. Stress exponents were extracted from the strain-time curves that were generated during high-temperature deformation experiments. The key findings of this investigation are as follows:

1. During high-temperature compression of fine-grained TM-ESOs, grain size and morphology do not change, yet additional formation of secondary phases is observed.
2. The secondary phase in fine-grained TM-ESO forms a layer around the grain, as opposed to discrete particles within the particle, and in the grain boundaries in coarse-grained TM-ESO.
3. The single-phase and multiphase fine-grained TM-ESO samples had stress exponent values in the range between 0.1 and 0.4, with a slight decrease in stress exponent value as the

deformation temperature increased, likely due to an enhancement in grain boundary sliding. The low stress exponent values indicate superplastic deformation.

4. At lower deformation temperatures (e.g., between 600 °C and 700 °C), the multiphase TM-ESO had stress exponent values between 0.7 and 1.8, and the single-phase TM-ESO had stress exponent values between 0.5 and 0.8. The increase in stress exponent value with the presence of secondary phases is likely due to grain boundary pinning by secondary phase particles at the grain boundary, which inhibits grain boundary sliding.
5. At higher deformation temperatures (e.g., between 750 °C and 850 °C), the multiphase and single-phase TM-ESO stress exponent values decrease and remain relatively constant, likely due to the activation of solute-drag creep.

Fine-grained TM-ESOs deform superplastically across a wide temperature range. In coarse-grained TM-ESOs, secondary phases can be used to pin grain boundaries and inhibit deformation of the TM-ESOs up to a certain temperature. Overall, this work demonstrates that the microstructure and phase composition can be manipulated to control the high-temperature deformation behavior of TM-ESOs.

5.4 Recommendations for future work

Given the acoustic attenuation that occurs during UV-A DED of large build geometries, it is recommended to seek out some method of tuning the wave frequency during deposition to keep the amplitude constant. This could be achieved by using a different type of ultrasonic transducer, such as a magnetostrictive transducer, or by applying the UV from the top down.

Given the reversible phase transformation in TM-ESOs, there are several studies that would provide valuable insights to the experiments laid out in this dissertation. As the morphology of secondary phases is different at smaller grain sizes, it would be insightful to understand how

nanocrystalline TM-ESO behaves mechanically at room temperature. Additionally, it would be insightful to understand how modifying the composition of TM-ESO influences the kinetics of the phase transformation. By using atomic force microscopy (AFM), it is also possible to get measurements of the stiffness of individual secondary phase particles, which would be insightful to understanding how their presence influences the overall elastic modulus of TM-ESO.

References

[1] J. Pelleg, *Mechanical Properties of Materials*. Dordrecht New York: Springer, 2013.

[2] W. D. Callister, *Materials Science and Engineering: An Introduction*, 7th ed. New York: John Wiley & Sons, 2007.

[3] T. DebRoy, H. L. Wei, J. S. Zuback, T. Mukherjee, J. W. Elmer, J. O. Milewski, A. M. Beese, A. Wilson-Heid, A. De, and W. Zhang, "Additive manufacturing of metallic components – Process, structure and properties," *Progress in Materials Science*, vol. 92, pp. 112–224, Mar. 2018, doi: 10.1016/j.pmatsci.2017.10.001.

[4] F. Arias-González, A. Rodríguez-Contreras, M. Punset, J. M. Manero, Ó. Barro, M. Fernández-Arias, F. Lusquiños, F. J. Gil, and J. Pou, "In-Situ Laser Directed Energy Deposition of Biomedical Ti-Nb and Ti-Zr-Nb Alloys from Elemental Powders," *Metals*, vol. 11, no. 8, p. 1205, Jul. 2021, doi: 10.3390/met11081205.

[5] T. G. Spears and S. A. Gold, "In-process sensing in selective laser melting (SLM) additive manufacturing," *Integrating Materials and Manufacturing Innovation*, vol. 5, no. 1, pp. 16–40, Dec. 2016, doi: 10.1186/s40192-016-0045-4.

[6] S. A. Bansal, V. Khanna, and P. Gupta, *Metal Matrix Composites: Fabrication, Production, and 3D Printing (Vol. 1)*, 1st ed. Boca Raton: CRC Press, 2022. doi: 10.1201/9781003194897.

[7] J. Xiong, Y. Li, R. Li, and Z. Yin, "Influences of process parameters on surface roughness of multi-layer single-pass thin-walled parts in GMAW-based additive manufacturing," *Journal of Materials Processing Technology*, vol. 252, pp. 128–136, Feb. 2018, doi: 10.1016/j.jmatprotec.2017.09.020.

[8] Y. Xiong, W. H. Hofmeister, Z. Cheng, J. E. Smugeresky, E. J. Lavernia, and J. M. Schoenung, "In situ thermal imaging and three-dimensional finite element modeling of tungsten carbide–cobalt during laser deposition," *Acta Materialia*, vol. 57, no. 18, pp. 5419–5429, Oct. 2009, doi: 10.1016/j.actamat.2009.07.038.

[9] B. Davoren, N. Sacks, and M. Theron, "Laser engineered net shaping of WC-9.2wt%Ni alloys: A feasibility study," *International Journal of Refractory Metals and Hard Materials*, vol. 86, p. 105136, Jan. 2020, doi: 10.1016/j.ijrmhm.2019.105136.

[10] L. F. Francis, *Materials Processing*. Elsevier, 2016.

[11] R. M. German, *Fundamentals of Sintering. In: Engineered Materials Handbook*, vol. 4. ASM International, Engineered Materials Handbook, 1991.

[12] M. R. Mazlan, N. H. Jamadon, A. Rajabi, A. B. Sulong, I. F. Mohamed, F. Yusof, and N. A. Jamal, "Necking mechanism under various sintering process parameters – A review," *Journal of Materials Research and Technology*, vol. 23, pp. 2189–2201, Mar. 2023, doi: 10.1016/j.jmrt.2023.01.013.

[13] U. Techakijkajorn, W. J. Frederick, and H. N. Tran, "Sintering and densification of recovery boiler deposits: Laboratory data and a rate model," *Journal of Pulp and Paper Science*, vol. 25, no. 3, pp. 73–80, 1999.

[14] J. E. Garay, "Current-Activated, Pressure-Assisted Densification of Materials," *Annual Review of Materials Research*, vol. 40, no. 1, pp. 445–468, Jun. 2010, doi: 10.1146/annurev-matsci-070909-104433.

[15] T. H. Courtney, *Mechanical Behavior of Materials*. Waveland Press, Incorporated, 2005.

[16] A. M. Okoro, R. Machaka, S. S. Lephuthing, S. R. Oke, M. A. Awotunde, and P. A. Olubambi, "Nanoindentation studies of the mechanical behaviours of spark plasma sintered multiwall

carbon nanotubes reinforced Ti6Al4V nanocomposites," *Materials Science and Engineering: A*, vol. 765, p. 138320, Sep. 2019, doi: 10.1016/j.msea.2019.138320.

[17] H. K. Sharma, "A review of nanoindentation and related cathodoluminescence studies on semiconductor materials," *Journal of Materials Science: Materials in Electronics*, 2022.

[18] D. Adamovic and F. Zivic, "Hardness and Non-Destructive Testing (NDT) of Ceramic Matrix Composites (CMCs)," in *Encyclopedia of Materials: Composites*, vol. 2, 2021, pp. 183–201.

[19] G. I. Eskin and D. G. Eskin, *Ultrasonic Treatment of Light Alloy Melts*, 2nd ed. Boca Raton, FL: Taylor & Francis Group, 2015.

[20] H. Liu, X. Qiao, Z. Chen, R. Jiang, and X. Li, "Effect of ultrasonic vibration during casting on microstructures and properties of 7050 aluminum alloy," *Journal of Materials Science*, vol. 46, no. 11, pp. 3923–3927, Jun. 2011, doi: 10.1007/s10853-011-5316-z.

[21] G. Chen, M. Yang, Y. Jin, H. Zhang, F. Han, Q. Chen, and Z. Zhao, "Ultrasonic assisted squeeze casting of a wrought aluminum alloy," *Journal of Materials Processing Technology*, vol. 266, pp. 19–25, Apr. 2019, doi: 10.1016/j.jmatprotec.2018.10.032.

[22] A. H. Idrisi and A.-H. I. Mourad, "Conventional stir casting versus ultrasonic assisted stir casting process: Mechanical and physical characteristics of AMCs," *Journal of Alloys and Compounds*, vol. 805, pp. 502–508, Oct. 2019, doi: 10.1016/j.jallcom.2019.07.076.

[23] X. J. Wang, N. Z. Wang, L. Y. Wang, X. S. Hu, K. Wu, Y. Q. Wang, and Y. D. Huang, "Processing, microstructure and mechanical properties of micro-SiC particles reinforced magnesium matrix composites fabricated by stir casting assisted by ultrasonic treatment processing," *Materials & Design*, vol. 57, pp. 638–645, May 2014, doi: 10.1016/j.matdes.2014.01.022.

[24] L. Wang, C. Zhang, and C. Wu, “Experimental study on controlled pulse keyholing plasma arc welding assisted by ultrasonic vibration,” *The International Journal of Advanced Manufacturing Technology*, vol. 107, no. 11–12, pp. 4995–5009, Apr. 2020, doi: 10.1007/s00170-020-05384-w.

[25] S. Kumar, C. S. Wu, G. K. Padhy, and W. Ding, “Application of ultrasonic vibrations in welding and metal processing: A status review,” *Journal of Manufacturing Processes*, vol. 26, pp. 295–322, Apr. 2017, doi: 10.1016/j.jmapro.2017.02.027.

[26] G. Wagner, F. Balle, and D. Eifler, “Ultrasonic Welding of Hybrid Joints,” *JOM*, vol. 64, no. 3, pp. 401–406, Mar. 2012, doi: 10.1007/s11837-012-0269-5.

[27] J. A. Gallego-Juárez and K. F. Graff, *Power Ultrasonics: Applications of High Intensity Ultrasound*, 1st ed. Elsevier, 2015.

[28] I. Gibson, D. Rosen, and B. Stucker, *Additive Manufacturing Technologies*. New York, NY: Springer New York, 2015. doi: 10.1007/978-1-4939-2113-3.

[29] D. Svetlizky, M. Das, B. Zheng, A. L. Vyatskikh, S. Bose, A. Bandyopadhyay, J. M. Schoenung, E. J. Lavernia, and N. Eliaz, “Directed energy deposition (DED) additive manufacturing: Physical characteristics, defects, challenges and applications,” *Materials Today*, p. S1369702121001139, Jun. 2021, doi: 10.1016/j.mattod.2021.03.020.

[30] J. Yu, M. Rombouts, G. Maes, and F. Motmans, “Material Properties of Ti6Al4V Parts Produced by Laser Metal Deposition,” *Physics Procedia*, vol. 39, pp. 416–424, 2012, doi: 10.1016/j.phpro.2012.10.056.

[31] P. L. Narayana, S. Lee, S.-W. Choi, C.-L. Li, C. H. Park, J.-T. Yeom, N. S. Reddy, and J.-K. Hong, “Microstructural response of β-stabilized Ti–6Al–4V manufactured by direct energy

deposition," *Journal of Alloys and Compounds*, vol. 811, p. 152021, Nov. 2019, doi: 10.1016/j.jallcom.2019.152021.

[32] A. Saboori, F. Bosio, E. Librera, M. de Chirico, S. Biamino, M. Lombardi, and P. Fino, "Accelerated Process Parameter Optimization for Directed Energy Deposition of 316L Stainless Steel," in *Euro PM2018 Proceedings USB*, Bilbao, Spain, Oct. 2018, p. 7.

[33] B. Zheng, J. C. Haley, N. Yang, J. Yee, K. W. Terrassa, Y. Zhou, E. J. Lavernia, and J. M. Schoenung, "On the evolution of microstructure and defect control in 316L SS components fabricated via directed energy deposition," *Materials Science and Engineering: A*, vol. 764, p. 138243, Sep. 2019, doi: 10.1016/j.msea.2019.138243.

[34] M. A. Melia, H.-D. A. Nguyen, J. M. Rodelas, and E. J. Schindelholz, "Corrosion properties of 304L stainless steel made by directed energy deposition additive manufacturing," *Corrosion Science*, vol. 152, pp. 20–30, May 2019, doi: 10.1016/j.corsci.2019.02.029.

[35] Z. Wang, T. A. Palmer, and A. M. Beese, "Effect of processing parameters on microstructure and tensile properties of austenitic stainless steel 304L made by directed energy deposition additive manufacturing," *Acta Materialia*, vol. 110, pp. 226–235, May 2016, doi: 10.1016/j.actamat.2016.03.019.

[36] M. Javidani, J. Arreguin-Zavala, J. Danovitch, Y. Tian, and M. Brochu, "Additive Manufacturing of AlSi10Mg Alloy Using Direct Energy Deposition: Microstructure and Hardness Characterization," *Journal of Thermal Spray Technology*, vol. 26, no. 4, pp. 587–597, Apr. 2017, doi: 10.1007/s11666-016-0495-4.

[37] P. Kiani, A. D. Dupuy, K. Ma, and J. M. Schoenung, "Directed energy deposition of AlSi10Mg: Single track nonscalability and bulk properties," *Materials & Design*, vol. 194, p. 108847, Sep. 2020, doi: 10.1016/j.matdes.2020.108847.

[38] L. L. Parimi, R. G. A., D. Clark, and M. M. Attallah, “Microstructural and texture development in direct laser fabricated IN718,” *Materials Characterization*, vol. 89, pp. 102–111, Mar. 2014, doi: 10.1016/j.matchar.2013.12.012.

[39] P. D. Nezhadfar, A. S. Johnson, and N. Shamsaei, “Fatigue behavior and microstructural evolution of additively manufactured Inconel 718 under cyclic loading at elevated temperature,” *International Journal of Fatigue*, vol. 136, p. 105598, Jul. 2020, doi: 10.1016/j.ijfatigue.2020.105598.

[40] D. Ma, A. D. Stoica, Z. Wang, and A. M. Beese, “Crystallographic texture in an additively manufactured nickel-base superalloy,” *Materials Science and Engineering: A*, vol. 684, pp. 47–53, Jan. 2017, doi: 10.1016/j.msea.2016.12.028.

[41] M. J. Kim and C. Saldana, “Thin wall deposition of IN625 using directed energy deposition,” *Journal of Manufacturing Processes*, vol. 56, pp. 1366–1373, Aug. 2020, doi: 10.1016/j.jmapro.2020.04.032.

[42] D. Bourell, J. P. Kruth, M. Leu, G. Levy, D. Rosen, A. M. Beese, and A. Clare, “Materials for additive manufacturing,” *CIRP Annals*, vol. 66, no. 2, pp. 659–681, 2017, doi: 10.1016/j.cirp.2017.05.009.

[43] *Design Guidelines for the Selection and Use of Stainless Steels -- A Designer’s Handbook Series*. Nickel Institute, 2020.

[44] P. S. Korinko and S. H. Malene, “Considerations for the weldability of types 304L and 316L stainless steel,” *Practical Failure Analysis*, vol. 1, no. 4, pp. 61–68, Aug. 2001, doi: 10.1007/BF02715336.

[45] A. L. Vyatskikh, T. B. Slagle, S. Jiang, S. A. El-Azab, U. S. Bertoli, L. Valdevit, E. J. Lavernia, and J. M. Schoenung, “Thickness-Dependent Microstructure in Additively

Manufactured Stainless Steel," *Journal of Materials Engineering and Performance*, vol. 30, no. 9, pp. 6606–6617, Sep. 2021, doi: 10.1007/s11665-021-05931-w.

[46] W. J. Sames, F. A. List, S. Pannala, R. R. Dehoff, and S. S. Babu, "The metallurgy and processing science of metal additive manufacturing," *International Materials Reviews*, vol. 61, no. 5, pp. 315–360, Jul. 2016, doi: 10.1080/09506608.2015.1116649.

[47] G. Tapia, A. H. Elwany, and H. Sang, "Prediction of porosity in metal-based additive manufacturing using spatial Gaussian process models," *Additive Manufacturing*, vol. 12, pp. 282–290, Oct. 2016, doi: 10.1016/j.addma.2016.05.009.

[48] T. Mukherjee, J. S. Zuback, A. De, and T. DebRoy, "Printability of alloys for additive manufacturing," *Scientific Reports*, vol. 6, no. 1, p. 19717, Apr. 2016, doi: 10.1038/srep19717.

[49] N. Lu, Z. Lei, K. Hu, X. Yu, P. Li, J. Bi, S. Wu, and Y. Chen, "Hot cracking behavior and mechanism of a third-generation Ni-based single-crystal superalloy during directed energy deposition," *Additive Manufacturing*, vol. 34, p. 101228, Aug. 2020, doi: 10.1016/j.addma.2020.101228.

[50] X. Lu, M. Chiumenti, M. Cervera, J. Li, X. Lin, L. Ma, G. Zhang, and E. Liang, "Substrate design to minimize residual stresses in Directed Energy Deposition AM processes," *Materials & Design*, vol. 202, p. 109525, Apr. 2021, doi: 10.1016/j.matdes.2021.109525.

[51] X. Lu, X. Lin, M. Chiumenti, M. Cervera, Y. Hu, X. Ji, L. Ma, H. Yang, and W. Huang, "Residual stress and distortion of rectangular and S-shaped Ti-6Al-4V parts by Directed Energy Deposition: Modelling and experimental calibration," *Additive Manufacturing*, vol. 26, pp. 166–179, Mar. 2019, doi: 10.1016/j.addma.2019.02.001.

[52] W. Cong and F. Ning, “A fundamental investigation on ultrasonic vibration-assisted laser engineered net shaping of stainless steel,” *International Journal of Machine Tools and Manufacture*, vol. 121, pp. 61–69, Oct. 2017, doi: 10.1016/j.ijmachtools.2017.04.008.

[53] F. Ning, Y. Hu, Z. Liu, W. Cong, Y. Li, and X. Wang, “Ultrasonic Vibration-Assisted Laser Engineered Net Shaping of Inconel 718 Parts: A Feasibility Study,” *Procedia Manufacturing*, vol. 10, pp. 771–778, 2017, doi: 10.1016/j.promfg.2017.07.074.

[54] F. Ning, Y. Hu, Z. Liu, X. Wang, Y. Li, and W. Cong, “Ultrasonic Vibration-Assisted Laser Engineered Net Shaping of Inconel 718 Parts: Microstructural and Mechanical Characterization,” *Journal of Manufacturing Science and Engineering*, vol. 140, no. 6, p. 061012, Jun. 2018, doi: 10.1115/1.4039441.

[55] F. Ning, D. Jiang, Z. Liu, H. Wang, and W. Cong, “Ultrasonic Frequency Effects on the Melt Pool Formation, Porosity, and Thermal-Dependent Property of Inconel 718 Fabricated by Ultrasonic Vibration-Assisted Directed Energy Deposition,” *Journal of Manufacturing Science and Engineering*, vol. 143, no. 5, p. 051009, May 2021, doi: 10.1115/1.4048515.

[56] C. J. Todaro, M. A. Easton, D. Qiu, D. Zhang, M. J. Bermingham, E. W. Lui, M. Brandt, D. H. StJohn, and M. Qian, “Grain structure control during metal 3D printing by high-intensity ultrasound,” *Nature Communications*, vol. 11, no. 1, p. 142, Dec. 2020, doi: 10.1038/s41467-019-13874-z.

[57] C. J. Todaro, M. A. Easton, D. Qiu, M. Brandt, D. H. StJohn, and M. Qian, “Grain refinement of stainless steel in ultrasound-assisted additive manufacturing,” *Additive Manufacturing*, vol. 37, p. 101632, Jan. 2021, doi: 10.1016/j.addma.2020.101632.

[58] J. C. Haley, B. Zheng, U. S. Bertoli, A. D. Dupuy, J. M. Schoenung, and E. J. Lavernia, “Working distance passive stability in laser directed energy deposition additive

manufacturing," *Materials & Design*, vol. 161, pp. 86–94, Jan. 2019, doi: 10.1016/j.matdes.2018.11.021.

[59] I. Yadroitsev, "Hierarchical design principles of selective laser melting for high quality metallic objects," *Additive Manufacturing*, p. 12, 2015.

[60] "Photron FASTCAM Viewer 4." Photron.

[61] G. Van Rossum and F. Drake, "Python 3 Reference Manual." CreateSpace, Scotts Valley, CA, 2009.

[62] D. M. D. Abràmoff, "Image Processing with ImageJ," *Biophotonics International*, p. 7, Jul. 2004.

[63] "AZtec HKL CHANNEL5." Oxford Instruments.

[64] D. G. Mccartney and J. D. Hunt, "Measurements of cell and primary dendrite arm spacings in directionally solidified aluminum alloys," *Acta Metallurgica*, vol. 29, pp. 1851–1863, 1981, doi: https://doi.org/10.1016/0001-6160(81)90111-5.

[65] R Core Team, "R: A Language and Environment for Statistical Computing." R Foundation for Statistical Computing, Vienna, Austria, 2013. Accessed: Jan. 26, 2022. [Online]. Available: http://www.R-project.org/

[66] D. W. Zhou, D. Y. Liu, X. G. Hu, and C. F. Ma, "Effect of acoustic cavitation on boiling heat transfer," *Experimental Thermal and Fluid Science*, vol. 26, no. 8, pp. 931–938, Oct. 2002, doi: 10.1016/S0894-1777(02)00201-7.

[67] P. N. T. Wells, "Absorption and dispersion of ultrasound in biological tissue," *Ultrasound in Medicine & Biology*, vol. 1, no. 4, pp. 369–376, Mar. 1975, doi: 10.1016/0301-5629(75)90124-6.

[68] G. L. Morini, "Viscous Dissipation," *Encyclopedia of Microfluidics and Nanofluidics*. Springer, Boston, MA. [Online]. Available: https://doi.org/10.1007/978-0-387-48998-8

[69] D. Li, *Encyclopedia of microfluidics and nanofluidics*. New York, N.Y: Springer, 2008.

[70] "The Marangoni Effect," *Multiphysics Cyclopedia*. COMSOL Multiphysics, 2015. [Online]. Available: https://www.comsol.com/multiphysics/marangoni-effect

[71] N. K. Adam, *The physics and chemistry of surfaces*, 3rd ed. London: Oxford University Press, 1941.

[72] T. S. Chow, "Wetting of rough surfaces," *Journal of Physics: Condensed Matter*, vol. 10, no. 1998, pp. L445–L451.

[73] J.-W. Song and L.-W. Fan, "Temperature dependence of the contact angle of water: A review of research progress, theoretical understanding, and implications for boiling heat transfer," *Advances in Colloid and Interface Science*, vol. 288, p. 102339, Feb. 2021, doi: 10.1016/j.cis.2020.102339.

[74] J. C. Haley, J. M. Schoenung, and E. J. Lavernia, "Modelling particle impact on the melt pool and wettability effects in laser directed energy deposition additive manufacturing," *Materials Science and Engineering: A*, vol. 761, p. 138052, Jul. 2019, doi: 10.1016/j.msea.2019.138052.

[75] P. Sahoo, T. Debroy, and M. J. McNallan, "Surface tension of binary metal—surface active solute systems under conditions relevant to welding metallurgy," *MTB*, vol. 19, no. 3, pp. 483–491, Jun. 1988, doi: 10.1007/BF02657748.

[76] Y. Wang, Q. Shi, and H. L. Tsai, "Modeling of the effects of surface-active elements on flow patterns and weld penetration," *Metallurgical and Materials Transactions B*, vol. 32, no. 1, pp. 145–161, Feb. 2001, doi: 10.1007/s11663-001-0017-7.

[77] P. S. Wei and F. K. Chung, “Unsteady marangoni flow in a molten pool when welding dissimilar metals,” *Metallurgical and Materials Transactions B*, vol. 31, no. 6, pp. 1387–1403, Dec. 2000, doi: 10.1007/s11663-000-0024-0.

[78] S. H. Park and S. D. Kim, “Plasma surface treatment of HDPE powder in a fluidized bed reactor,” *Polymer Bulletin*, vol. 33, no. 2, pp. 249–256, Jul. 1994, doi: 10.1007/BF00297363.

[79] J. Yu, S. Ueno, and K. Hiragushi, “Improvement in Flowability, Oxidation Resistance and Water Wettability of Graphite Powders by TiO_2 Coating,” *Journal of the Ceramic Society of Japan*, vol. 104, no. 1210, pp. 481–485, 1996, doi: 10.2109/jcersj.104.481.

[80] T. Mukherjee, W. Zhang, and T. DebRoy, “An improved prediction of residual stresses and distortion in additive manufacturing,” *Computational Materials Science*, vol. 126, pp. 360–372, Jan. 2017, doi: 10.1016/j.commatsci.2016.10.003.

[81] T. S. Hutchison, “Ultrasonic Absorption in Solids: How high-frequency sound is damped by imperfections in solids.,” *Science*, vol. 132, no. 3428, pp. 643–652, Sep. 1960, doi: 10.1126/science.132.3428.643.

[82] J. Krautkrämer and H. Krautkrämer, *Ultrasonic Testing of Materials*, 4th ed. Springer Berlin, Heidelberg, 1990.

[83] F. P. Mechel, *Formulas of Acoustics*, 2nd ed. Springer Berlin, Heidelberg, 2008.

[84] X. Sun, F. Jiang, and J. Wang, “Acoustic Properties of 316L Stainless Steel Lattice Structures Fabricated via Selective Laser Melting,” *Metals*, vol. 10, no. 1, p. 111, Jan. 2020, doi: 10.3390/met10010111.

[85] Y. Wu, L. Han, H. Gong, and A. S. Ahmad, “A modified model for simulating the effect of temperature on ultrasonic attenuation in 7050 aluminum alloy,” *AIP Advances*, vol. 8, no. 8, p. 085003, Aug. 2018, doi: 10.1063/1.5045627.

[86] R. Berg E., “ultrasonics,” *Encyclopedia Brittanica*. 2017. [Online]. Available: https://www.britannica.com/science/ultrasonics#ref527466

[87] F. Wang, D. Eskin, J. Mi, C. Wang, B. Koe, A. King, C. Reinhard, and T. Connolley, “A synchrotron X-radiography study of the fragmentation and refinement of primary intermetallic particles in an Al-35 Cu alloy induced by ultrasonic melt processing,” *Acta Materialia*, vol. 141, pp. 142–153, Dec. 2017, doi: 10.1016/j.actamat.2017.09.010.

[88] S. Wang, Z. P. Guo, X. P. Zhang, A. Zhang, and J. W. Kang, “On the mechanism of dendritic fragmentation by ultrasound induced cavitation,” *Ultrasonics Sonochemistry*, vol. 51, pp. 160–165, Mar. 2019, doi: 10.1016/j.ultsonch.2018.10.031.

[89] S. Wang, J. Kang, Z. Guo, T. L. Lee, X. Zhang, Q. Wang, C. Deng, and J. Mi, “In situ high speed imaging study and modelling of the fatigue fragmentation of dendritic structures in ultrasonic fields,” *Acta Materialia*, vol. 165, pp. 388–397, Feb. 2019, doi: 10.1016/j.actamat.2018.11.053.

[90] S. Kou, *Welding Metallurgy*, 3rd ed. Wiley, 2020.

[91] D. A. Porter, K. E. Easterling, and M. Y. Sherif, “Alloy Solidification,” in *Phase Transformations in Metals and Alloys*, 3rd ed., Boca Raton, FL: Taylor & Francis Group, 2009, pp. 209–230.

[92] G. Chirita, I. Stefanescu, D. Soares, and F. S. Silva, “Influence of vibration on the solidification behaviour and tensile properties of an Al–18wt%Si alloy,” *Materials & Design*, vol. 30, no. 5, pp. 1575–1580, May 2009, doi: 10.1016/j.matdes.2008.07.045.

[93] N. Omura, Y. Murakami, M. Li, T. Tamura, K. Miwa, H. Furukawa, and M. Harada, “Effects of Mechanical Vibration on Cooling Rate and DAS of AC4C Aluminum Alloy Gravity Die

Castings," *Materials Transactions*, vol. 50, no. 11, pp. 2604–2608, 2009, doi: 10.2320/matertrans.M2009247.

[94] C.-W. Kuo, C.-M. Lin, G.-H. Lai, Y.-C. Chen, Y.-T. Chang, and W. Wu, "Characterization and Mechanism of 304 Stainless Steel Vibration Welding," *Materials Transactions*, vol. 48, no. 9, pp. 2319–2323, 2007, doi: 10.2320/matertrans.MB200706.

[95] Y. Cui, C. Xu, and Q. Han, "Microstructure Improvement in Weld Metal Using Ultrasonic Vibrations," *Advanced Engineering Materials*, vol. 9, no. 3, pp. 161–163, Mar. 2007, doi: 10.1002/adem.200600228.

[96] M. Tang, P. C. Pistorius, and J. L. Beuth, "Prediction of lack-of-fusion porosity for powder bed fusion," *Additive Manufacturing*, vol. 14, pp. 39–48, Mar. 2017, doi: 10.1016/j.addma.2016.12.001.

[97] T. Mukherjee and T. DebRoy, "Mitigation of lack of fusion defects in powder bed fusion additive manufacturing," *Journal of Manufacturing Processes*, vol. 36, pp. 442–449, Dec. 2018, doi: 10.1016/j.jmapro.2018.10.028.

[98] D. F. Susan, J. D. Puskar, J. A. Brooks, and C. V. Robino, "Quantitative characterization of porosity in stainless steel LENS powders and deposits," *Materials Characterization*, vol. 57, no. 1, pp. 36–43, Jul. 2006, doi: 10.1016/j.matchar.2005.12.005.

[99] D. B. Miracle, "High entropy alloys as a bold step forward in alloy development," *Nature Communications*, vol. 10, no. 1, p. 1805, Dec. 2019, doi: 10.1038/s41467-019-09700-1.

[100] B. Cantor, I. T. H. Chang, P. Knight, and A. J. B. Vincent, "Microstructural development in equiatomic multicomponent alloys," *Materials Science and Engineering: A*, vol. 375–377, pp. 213–218, Jul. 2004, doi: 10.1016/j.msea.2003.10.257.

[101] J.-W. Yeh, S.-K. Chen, S.-J. Lin, J.-Y. Gan, T.-S. Chin, T.-T. Shun, C.-H. Tsau, and S.-Y. Chang, "Nanostructured High-Entropy Alloys with Multiple Principal Elements: Novel Alloy Design Concepts and Outcomes," *Advanced Engineering Materials*, vol. 6, no. 5, pp. 299–303, May 2004, doi: 10.1002/adem.200300567.

[102] Y. F. Ye, Q. Wang, J. Lu, C. T. Liu, and Y. Yang, "High-entropy alloy: challenges and prospects," *Materials Today*, vol. 19, no. 6, pp. 349–362, Jul. 2016, doi: 10.1016/j.mattod.2015.11.026.

[103] C. M. Rost, E. Sachet, T. Borman, A. Moballegh, E. C. Dickey, D. Hou, J. L. Jones, S. Curtarolo, and J.-P. Maria, "Entropy-stabilized oxides," *Nat Commun*, vol. 6, no. 1, p. 8485, Dec. 2015, doi: 10.1038/ncomms9485.

[104] N. G. Jones, J. W. Aveson, A. Bhowmik, B. D. Conduit, and H. J. Stone, "On the entropic stabilisation of an Al0.5CrFeCoNiCu high entropy alloy," *Intermetallics*, vol. 54, pp. 148–153, Nov. 2014, doi: 10.1016/j.intermet.2014.06.004.

[105] F. Otto, Y. Yang, H. Bei, and E. P. George, "Relative effects of enthalpy and entropy on the phase stability of equiatomic high-entropy alloys," *Acta Materialia*, vol. 61, no. 7, pp. 2628–2638, Apr. 2013, doi: 10.1016/j.actamat.2013.01.042.

[106] Z. Wu, H. Bei, F. Otto, G. M. Pharr, and E. P. George, "Recovery, recrystallization, grain growth and phase stability of a family of FCC-structured multi-component equiatomic solid solution alloys," *Intermetallics*, vol. 46, pp. 131–140, Mar. 2014, doi: 10.1016/j.intermet.2013.10.024.

[107] F. Zhang, C. Zhang, S. L. Chen, J. Zhu, W. S. Cao, and U. R. Kattner, "An understanding of high entropy alloys from phase diagram calculations," *Calphad*, vol. 45, pp. 1–10, Jun. 2014, doi: 10.1016/j.calphad.2013.10.006.

[108] D. A. Porter, K. E. Easterling, and M. Y. Sherif, *Phase Transformations in Metals and Alloys*, 3rd ed. Boca Raton, FL: Taylor & Francis Group, 2009.

[109] A. D. Dupuy, I.-T. Chiu, P. Shafer, E. Arenholz, Y. Takamura, and J. M. Schoenung, "Hidden transformations in entropy-stabilized oxides," *Journal of the European Ceramic Society*, vol. 41, no. 13, pp. 6660–6669, Oct. 2021, doi: 10.1016/j.jeurceramsoc.2021.06.014.

[110] A. D. Dupuy, X. Wang, and J. M. Schoenung, "Entropic phase transformation in nanocrystalline high entropy oxides," *Materials Research Letters*, vol. 7, no. 2, pp. 60–67, Feb. 2019, doi: 10.1080/21663831.2018.1554605.

[111]T. Runčevski and C. M. Brown, "The Rietveld Refinement Method: Half of a Century Anniversary," *Crystal Growth & Design*, vol. 21, no. 9, pp. 4821–4822, Sep. 2021, doi: 10.1021/acs.cgd.1c00854.

[112] A. D. Dupuy, M. R. Chellali, H. Hahn, and J. M. Schoenung, "Nucleation and growth behavior of multicomponent secondary phases in entropy-stabilized oxides," *Journal of Materials Research*, vol. 38, no. 1, pp. 198–214, Jan. 2023, doi: 10.1557/s43578-022-00784-y.

[113] J. Sure, D. S. Maha Vishnu, H.-K. Kim, and C. Schwandt, "Facile Electrochemical Synthesis of Nanoscale (TiNbTaZrHf)C High-Entropy Carbide Powder," *Angewandte Chemie - International Edition*, vol. 59, no. 29, pp. 11830–11835, 2020, doi: 10.1038/s41598-018-26827-1.

[114] E. Castle, T. Csanádi, S. Grasso, J. Dusza, and M. Reece, "Processing and Properties of High-Entropy Ultra-High Temperature Carbides," *Scientific Reports*, vol. 8, no. 1, p. 8609, Dec. 2018, doi: 10.1038/s41598-018-26827-1.

[115] J. Gild, Y. Zhang, T. Harrington, S. Jiang, T. Hu, M. C. Quinn, W. M. Mellor, N. Zhou, K. Vecchio, and J. Luo, "High-Entropy Metal Diborides: A New Class of High-Entropy Materials and a New Type of Ultrahigh Temperature Ceramics," *Scientific Reports*, vol. 6, no. 1, p. 37946, Dec. 2016, doi: 10.1038/srep37946.

[116] T. Jin, X. Sang, R. R. Unocic, R. T. Kinch, X. Liu, J. Hu, H. Liu, and S. Dai, "Mechanochemical-Assisted Synthesis of High-Entropy Metal Nitride via a Soft Urea Strategy," *Advanced Materials*, vol. 30, no. 23, pp. 1–5, 2018, doi: 10.1002/adma.201707512.

[117] R.-Z. Zhang, F. Gucci, H. Zhu, K. Chen, and M. J. Reece, "Data-Driven Design of Ecofriendly Thermoelectric High-Entropy Sulfides," *Inorganic Chemistry*, vol. 57, no. 20, pp. 13027–13033, Oct. 2018, doi: 10.1021/acs.inorgchem.8b02379.

[118] J. Gild, M. Samiee, J. L. Braun, T. Harrington, H. Vega, P. E. Hopkins, K. Vecchio, and J. Luo, "High-entropy fluorite oxides," *Journal of the European Ceramic Society*, vol. 38, no. 10, pp. 3578–3584, Aug. 2018, doi: 10.1016/j.jeurceramsoc.2018.04.010.

[119] D. Bérardan, S. Franger, A. K. Meena, and N. Dragoe, "Room temperature lithium superionic conductivity in high entropy oxides," *Journal of Materials Chemistry A*, vol. 4, no. 24, pp. 9536–9541, 2016, doi: 10.1039/C6TA03249D.

[120] D. Bérardan, S. Franger, D. Dragoe, A. K. Meena, and N. Dragoe, "Colossal dielectric constant in high entropy oxides," *Phys. Status Solidi RRL*, vol. 10, no. 4, pp. 328–333, Apr. 2016, doi: 10.1002/pssr.201600043.

[121] A. Sarkar, L. Velasco, D. Wang, Q. Wang, G. Talasila, L. de Biasi, C. Kübel, T. Brezesinski, S. S. Bhattacharya, H. Hahn, and B. Breitung, "High entropy oxides for reversible energy storage," *Nature Communications*, vol. 9, no. 1, p. 3400, Dec. 2018, doi: 10.1038/s41467-018-05774-5.

[122] J. L. Braun, C. M. Rost, M. Lim, A. Giri, D. H. Olson, G. N. Kotsonis, G. Stan, D. W. Brenner, J.-P. Maria, and P. E. Hopkins, "Charge-Induced Disorder Controls the Thermal Conductivity of Entropy-Stabilized Oxides," *Advanced Materials*, vol. 30, p. 1805004, 2018, doi: 10.1002/adma.201805004.

[123] S. H. Albedwawi, A. AlJaberi, G. N. Haidemenopoulos, and K. Polychronopoulou, "High entropy oxides-exploring a paradigm of promising catalysts: A review," *Materials & Design*, vol. 202, p. 109534, Apr. 2021, doi: 10.1016/j.matdes.2021.109534.

[124] Y. Xu, X. Xu, and L. Bi, "A high-entropy spinel ceramic oxide as the cathode for proton-conducting solid oxide fuel cells," *Journal of Advanced Ceramics*, vol. 11, no. 5, pp. 794–804, May 2022, doi: 10.1007/s40145-022-0573-7.

[125] K. C. Pitike, A. E. Marquez-Rossy, A. Flores-Betancourt, D. X. Chen, K. Santosh, V. R. Cooper, and E. Lara-Curzio, "On the elastic anisotropy of the entropy-stabilized oxide (Mg, Co, Ni, Cu, Zn)O compound," *Journal of Applied Physics*, vol. 128, no. 1, p. 015101, Jul. 2020, doi: 10.1063/5.0011352.

[126] W. Hong, F. Chen, Q. Shen, Y. Han, W. G. Fahrenholtz, and L. Zhang, "Microstructural evolution and mechanical properties of (Mg,Co,Ni,Cu,Zn)O high-entropy ceramics," *Journal of the American Ceramic Society*, p. jace.16075, Oct. 2018, doi: 10.1111/jace.16075.

[127] X. Wang, J. Cortez, A. D. Dupuy, J. M. Schoenung, and W. J. Bowman, "High entropy oxide (Co,Cu,Mg,Ni,Zn)O exhibits grain size dependent room temperature deformation," *Materials Research Letters*, vol. 11, no. 3, pp. 196–204, Mar. 2023, doi: 10.1080/21663831.2022.2135409.

[128] P. H. Mayrhofer, A. Hörling, L. Karlsson, J. Sjölén, T. Larsson, C. Mitterer, and L. Hultman, “Self-organized nanostructures in the Ti–Al–N system,” *Applied Physics Letters*, vol. 83, no. 10, pp. 2049–2051, Sep. 2003, doi: 10.1063/1.1608464.

[129] T. Sakuma, Y.-I. Yoshizawa, and H. Suto, “The modulated structure formed by isothermal ageing in Zr02-5.2 moi % Y20a alloy,” p. 8.

[130] S. H. Gould, “The Method of Archimedes,” *The American Mathematical Monthly*, vol. 62, no. 7P1, pp. 473–476, Aug. 1955, doi: 10.1080/00029890.1955.11988664.

[131] A. I. Saville, A. Creuziger, E. B. Mitchell, S. C. Vogel, J. T. Benzing, J. Klemm-Toole, K. D. Clarke, and A. J. Clarke, “MAUD Rietveld Refinement Software for Neutron Diffraction Texture Studies of Single- and Dual-Phase Materials,” *Integrating Materials and Manufacturing Innovation*, vol. 10, no. 3, pp. 461–487, Sep. 2021, doi: 10.1007/s40192-021-00224-5.

[132] X. Li and B. Bhushan, “A review of nanoindentation continuous stiffness measurement technique and its applications,” *Materials Characterization*, vol. 48, no. 1, pp. 11–36, Feb. 2002, doi: 10.1016/S1044-5803(02)00192-4.

[133] M. Mata, O. Casals, and J. Alcalá, “The plastic zone size in indentation experiments: The analogy with the expansion of a spherical cavity,” *International Journal of Solids and Structures*, vol. 43, no. 20, pp. 5994–6013, Oct. 2006, doi: 10.1016/j.ijsolstr.2005.07.002.

[134] V. M. Matyunin, N. Abusaif, and A. Y. Marchenkov, “Characteristics of the deformed zone around Vickers indentations in metals,” *IOP Conference Series: Materials Science and Engineering*, vol. 537, no. 3, p. 032004, May 2019, doi: 10.1088/1757-899X/537/3/032004.

[135] T. E. Mitchell, K. P. D. Lagerlöf, and A. H. Heuer, “Dislocations in ceramics,” *Materials Science and Technology*, vol. 1, no. 11, pp. 944–949, Nov. 1985, doi: 10.1179/mst.1985.1.11.944.

[136] Y. Han, X. Liu, Q. Zhang, M. Huang, Y. Li, W. Pan, P. Zong, L. Li, Z. Yang, Y. Feng, P. Zhang, and C. Wan, “Ultra-dense dislocations stabilized in high entropy oxide ceramics,” *Nature Communications*, vol. 13, no. 1, p. 2871, May 2022, doi: 10.1038/s41467-022-30260-4.

[137] G. K. Bansal and A. H. Heuer, “Precipitation Strengthening in Non-Stoichiometric Mg-Al Spinel,” in *Fracture Mechanics of Ceramics*, R. C. Bradt, D. P. H. Hasselman, and F. F. Lange, Eds. Boston, MA: Springer US, 1974, pp. 677–690. doi: 10.1007/978-1-4615-7014-1_15.

[138] Q. Wang, Z. Li, S. Pang, X. Li, C. Dong, and P. Liaw, “Coherent Precipitation and Strengthening in Compositionally Complex Alloys: A Review,” *Entropy*, vol. 20, no. 11, p. 878, Nov. 2018, doi: 10.3390/e20110878.

[139] K. Ma, H. Wen, T. Hu, T. D. Topping, D. Isheim, D. N. Seidman, E. J. Lavernia, and J. M. Schoenung, “Mechanical behavior and strengthening mechanisms in ultrafine grain precipitation-strengthened aluminum alloy,” *Acta Materialia*, vol. 62, pp. 141–155, Jan. 2014, doi: 10.1016/j.actamat.2013.09.042.

[140] P. L. Meena, R. Kumar, and K. Sreenivas, “Structural, elastic and magnetic properties of spinel Co3O4,” *Indian Journal of Pure & Applied Physics*, vol. 56, pp. 890–895, 2018.

[141] A. Kelly and R. B. Nicholson, “Strengthening methods in crystals,” *Composites*, p. 10, 1971, doi: 10.1016/0010-4361(71)90159-5.

[142] J. M. Silcock, T. J. Heal, and H. K. Hardy, “Structural ageing characteristics of binary aluminium-copper alloys,” *Journal of the Institute of Metals*, vol. 82, p. 239, 1954.

[143] L. J. Cohen and O. Ishai, “The Elastic Properties of Three-Phase Composites,” *Journal of Composite Materials*, vol. 1, no. 4, pp. 390–403, Oct. 1967, doi: 10.1177/002199836700100407.

[144] X. Huang, G. Xie, X. Liu, H. Fu, L. Shao, and Z. Hao, “The influence of precipitation transformation on Young’s modulus and strengthening mechanism of a Cu–Be binary alloy,” *Materials Science and Engineering: A*, vol. 772, p. 138592, Jan. 2020, doi: 10.1016/j.msea.2019.138592.

[145] M. Meyers and K. Chawla, *Mechanical Behavior of Materials*, 2nd ed. Cambridge University Press, 2008.

[146] R. Chaim, “Percolative composite model for prediction of the properties of nanocrystalline materials,” *Journal of Materials Research*, vol. 12, no. 7, pp. 1828–1836, Jul. 1997, doi: 10.1557/JMR.1997.0251.

[147] G. Bracq, M. Laurent-Brocq, C. Varvenne, L. Perrière, W. A. Curtin, J.-M. Joubert, and I. Guillot, “Combining experiments and modeling to explore the solid solution strengthening of high and medium entropy alloys,” *Acta Materialia*, vol. 177, pp. 266–279, Sep. 2019, doi: 10.1016/j.actamat.2019.06.050.

[148] S. Nag and W. A. Curtin, “Effect of solute-solute interactions on strengthening of random alloys from dilute to high entropy alloys,” *Acta Materialia*, vol. 200, pp. 659–673, Nov. 2020, doi: 10.1016/j.actamat.2020.08.011.

[149] E. Isotta, W. Peng, A. Balodhi, and A. Zevalkink, “Elastic Moduli: a Tool for Understanding Chemical Bonding and Thermal Transport in Thermoelectric Materials,”

Angewandte Chemie International Edition, vol. 62, no. 12, p. e202213649, Mar. 2023, doi: 10.1002/anie.202213649.

[150] Y. Maehara and T. G. Langdon, "Superplasticity in ceramics," *Journal of Materials Science*, vol. 25, pp. 2275–2286, 1990, doi: 10.1007/BF00638018.

[151] F. Wakai, S. Sakaguchi, and Y. Matsuno, "Superplasticity of Yttria-Stabilized Tetragonal ZrO2 Polycrystals," *Advanced Ceramic Materials*, vol. 1, no. 3, pp. 259–263, Jul. 1986.

[152] K. Hiraga, B. N. Kim, K. Morita, and Y. Sakka, "High-Strain-Rate Superplasticity in Oxide Ceramics," *MSF*, vol. 447–448, pp. 291–298, Feb. 2004, doi: 10.4028/www.scientific.net/MSF.447-448.291.

[153] R. C. Gifkins, "Grain rearrangements during superplastic deformation," *Journal of Materials Science*, vol. 13, no. 9, pp. 1926–1936, Sep. 1978, doi: 10.1007/BF00552899.

[154] J. Cortez, A. D. Dupuy, H. Vahidi, O. K. Donaldson, W. J. Bowman, T. J. Rupert, and J. M. Schoenung, "Grain size dependent indentation respnse of single-phase (CoCuMgNiZn)O high entropy oxides," *Unpublished*.

[155] J. E. Norman, X. Wang, A. D. Dupuy, and J. M. Schoenung, "Micropillar compression of Single-Crystal Single-Phase (Co,Cu,Mg,Ni,Zn)O," *Unpublished*.

[156] S. A. El-Azab, J. E. Norman, L. Gomez, A. D. Dupuy, and J. M. Schoenung, "Dislocation-mediated room-temperature mechanical behavior of multiphase entropy stabilized oxides," *Unpublished*.

[157] A. D. Dupuy and J. M. Schoenung, "Morphological evolution in nanostructured secondary phases in entropy stabilized oxides," *Materials Characterization*, vol. 193, p. 112301, Nov. 2022, doi: 10.1016/j.matchar.2022.112301.

[158] H. W. Hayden, S. Floreen, and P. D. Goodell, “The deformation mechanisms of superplasticity,” *Metallurgical Transactions*, vol. 3, no. 4, pp. 833–842, Apr. 1972, doi: 10.1007/BF02647657.

[159] B. B. Straumal, A. Korneva, G. A. Lopez, A. Kuzmin, E. Rabkin, G. Gerstein, A. B. Straumal, and A. S. Gornakova, “Grain Boundary Wetting by a Second Solid Phase in the High Entropy Alloys: A Review,” *Materials*, vol. 14, no. 24, p. 7506, Dec. 2021, doi: 10.3390/ma14247506.

[160] B. Straumal, T. Lepkova, A. Korneva, G. Gerstein, O. Kogtenkova, and A. Gornakova, “Grain Boundary Wetting by the Second Solid Phase: 20 Years of History,” *Metals*, vol. 13, no. 5, p. 929, May 2023, doi: 10.3390/met13050929.

[161] Q. C. Nguyen, T. Csanádi, J. Gubicza, R. Valiev, B. Straumal, and T. G. Langdon, “The Effect of Grain Boundary Sliding and Strain Rate Sensitivity on the Ductility of Ultrafine-Grained Materials,” *MSF*, vol. 667–669, pp. 677–682, Dec. 2010, doi: 10.4028/www.scientific.net/MSF.667-669.677.

[162] T. Chakrabarti and S. Manna, “Zener pinning through coherent precipitate: A phase-field study,” *Computational Materials Science*, vol. 154, pp. 84–90, Nov. 2018, doi: 10.1016/j.commatsci.2018.07.041.

[163] C. S. Smith, “Metal interfaces,” in *ASM*, Cleveland, OH, p. 65.

[164] P. R. Rios, “A Theory for Grain Boundary Pinning by Particles,” *Acta Metallurgica*, vol. 35, no. 12, pp. 2805–2814, 1987.

[165] D. Fan, L. Chen, and S. P. Chen, “Numerical Simulation of Zener Pinning with Growing Second-Phase Particles,” *Journal of the American Ceramic Society*, vol. 81, no. 3, pp. 526–532, Mar. 1998, doi: 10.1111/j.1151-2916.1998.tb02370.x.

[166] A. H. Chokshi, “Diffusion creep in oxide ceramics,” *Journal of the European Ceramic Society*, vol. 22, no. 14–15, pp. 2469–2478, Jan. 2002, doi: 10.1016/S0955-2219(02)00105-X.

[167] S. Schachner, S. Jin, D. Gruber, and H. Harmuth, “Three stage creep behavior of MgO containing ordinary refractories in tension and compression,” *Ceramics International*, vol. 45, no. 7, pp. 9483–9490, May 2019, doi: 10.1016/j.ceramint.2018.09.124.

Appendix A: Supplementary information for Chapter 3

A.1 Nanoindentation load vs. depth curves

Representative load vs. depth curves for equimolar, Co-deficient, and Cu-deficient TM-ESO in their as-sintered single-phase state, and heat treated for 2 and 12 hours (forming multiphase materials), are shown in Fig. A1. A Berkovich tip was used to apply a load of 5 mN at a load rate of 1 mN/s and a hold time of 2 s. Fifty measurements were taken per sample. No pop-in effects were observed.

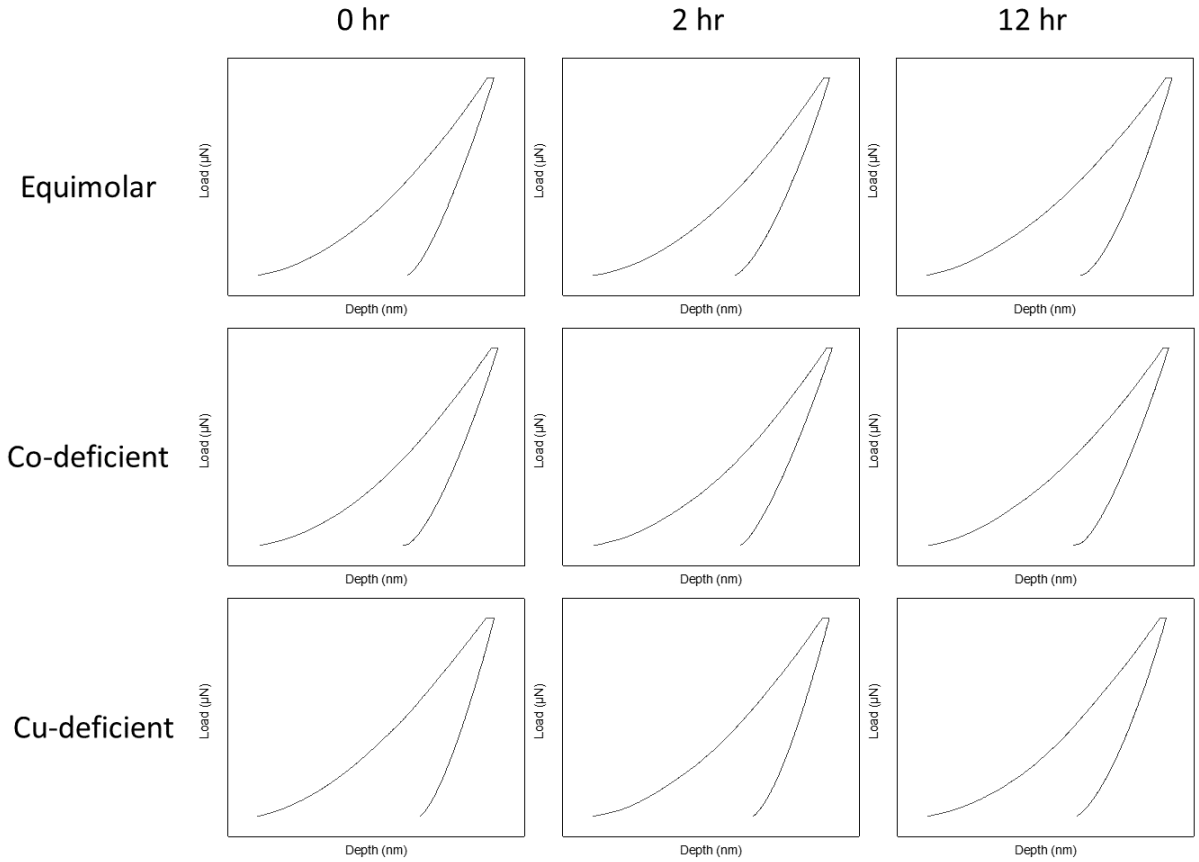

Figure A.1: Representative load vs. depth curves for each nanoindentation testing condition for TM-ESO. The columns correspond to the three heat treatment times used to prepare the samples (0 hr, 2 hr and 12 hr), and the rows correspond to the three compositions: equimolar, Co-deficient, and Cu-deficient. As-sintered samples are single-phase, and heat-treated samples are multiphase, as summarized in Table 3.2.

A.2 Strengthening increment calculation parameters

Table A.1 lists the shear modulus values by phase that were used in the strengthening increment calculations.

Table A.1: Shear modulus values used for strengthening increment calculations for heat treated, multiphase equimolar, Co-deficient, and Cu-deficient TM-ESO samples.

Phase	Shear modulus (GPa)	Reference
Rocksalt	58	This work
CuO Tenorite	47	[125]
Co_3O_4 Spinel	85	[140]

Tables A.2 – A.4 list relevant structural and microstructural parameters that were used in the strengthening increment calculations for the equimolar, Co-deficient, and Cu-deficient compositions for each heat treatment condition. The variables r and L are the secondary phase particle radius and particle spacing, respectively. The variables a_p and a_m are the lattice parameters for the secondary phase particles and primary matrix phase, respectively, and b is the Burger's vector of the matrix phase. The values for $r_{tenorite}$ and $L_{tenorite}$ were measured from scanning electron microscope and energy dispersive spectroscopy micrographs. The values for r_{spinel} and L_{spinel} were taken from literature [112]. The values for $f_{tenorite}$, f_{spinel}, $a_{p,tenorite}$, $a_{p,spinel}$, and a_m were extracted from X-ray diffraction data.

Table A.2a: Parameters used for strengthening increment calculations for heat-treated multiphase equimolar TM-ESO samples.

Heat Treatment Time (hr)	$r_{tenorite}$ (µm)	r_{spinel} (µm)	$f_{tenorite}$ (at. %)	f_{spinel} (at. %)	$L_{tenorite}$ (µm)	L_{spinel} (µm)
2	0.10	0.24	6	6	0.25	0.27
12	0.09	0.24	14	10	0.74	0.27

Table A.2b: Parameters used for strengthening increment calculations for heat-treated multiphase equimolar TM-ESO samples, continued.

Heat Treatment Time (hr)	$a_{p,tenorite}$ (nm)	$a_{p,spinel}$ (nm)	a_m (nm)	b (nm)
2	0.4722	0.8103	0.423273	1.197
12	0.4686	0.8104	0.423266	1.197

Table A.3: Parameters used for strengthening increment calculations for multiphase Co-deficient TM-ESO samples. HT stands for “heat treatment”.

Heat Treatment Time (hr)	$r_{tenorite}$ **(μm)**	$f_{tenorite}$ **(at. %)**	$a_{p,tenorite}$ **(nm)**	a_m **(nm)**	b **(nm)**	$L_{tenorite}$ **(μm)**
2	0.09	5	0.47074	0.42302	1.196	0.37
12	0.10	16	0.47069	0.42308	1.197	0.94

Table A.4: Parameters used for strengthening increment calculations for multiphase Cu-deficient TM-ESO samples. HT stands for “heat treatment”.

Heat Treatment Time (hr)	r_{spinel} **(μm)**	f_{spinel} **(at. %)**	$a_{p,spinel}$ **(nm)**	a_m **(nm)**	b **(nm)**	L_{spinel} **(μm)**
2	0.004	.05	0.8009	0.4232	1.1969	0.01
12	0.24	8	0.8101	0.4233	1.1973	0.27

A.3 Upper and lower bound elastic modulus of secondary phases

Lower and upper bound elastic modulus values found in literature were used to estimate a range of expected elastic modulus values for equimolar, Co-deficient, and Cu-deficient TM-ESOs. The values used are listed in Table A.6.

Table A.6: Lower and upper bound elastic modulus values for CuO tenorite and Co_3O_4 spinel phases

Phase	**Lower Bound Elastic Modulus (GPa)**	**Upper Bound Elastic Modulus (GPa)**	**Reference**
CuO Tenorite	60	130	[125]
Co_3O_4 Spinel	190	220	[140]

Appendix B: Supplementary information for Chapter 4

B.1 Raw data from high-temperature compression experiments

The stress-strain curves generated during the high-temperature compression experiments of Samples A – F are shown in Figs. B.1 – B.32. The strain rates that were extracted from each graph to calculate the stress exponent *n* for Samples A – F are summarized below in Tables B.1 – B.6.

B.1.1 Raw data for Sample A

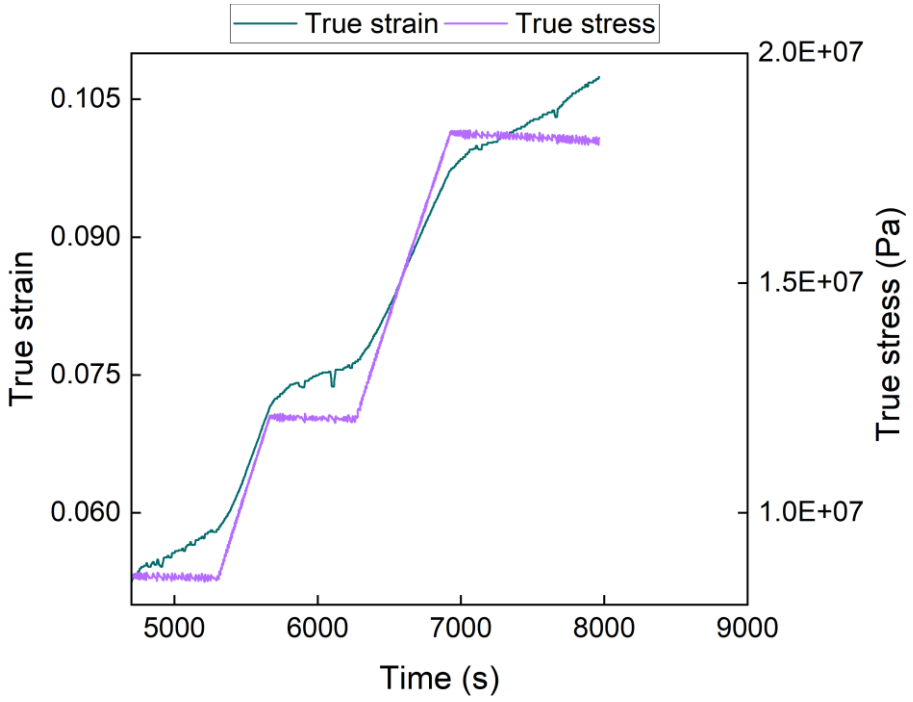

Figure B.1: Time-stress-strain curve generated during high-temperature compression experiment of Sample A conducted at 600 °C.

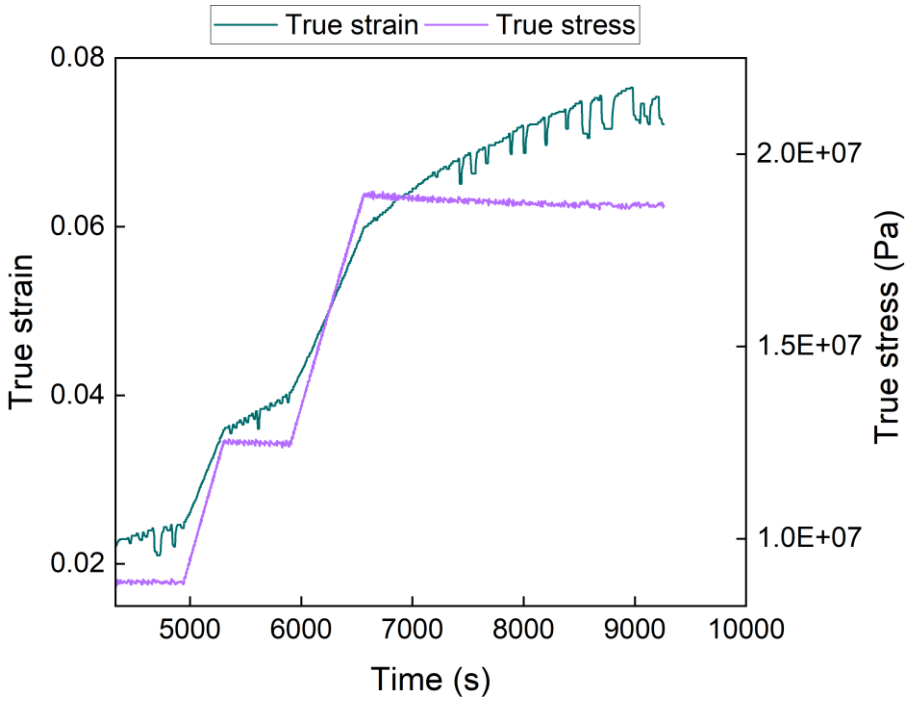

Figure B.2: Time-stress-strain curve generated during high-temperature compression experiment of Sample A conducted at 650 °C.

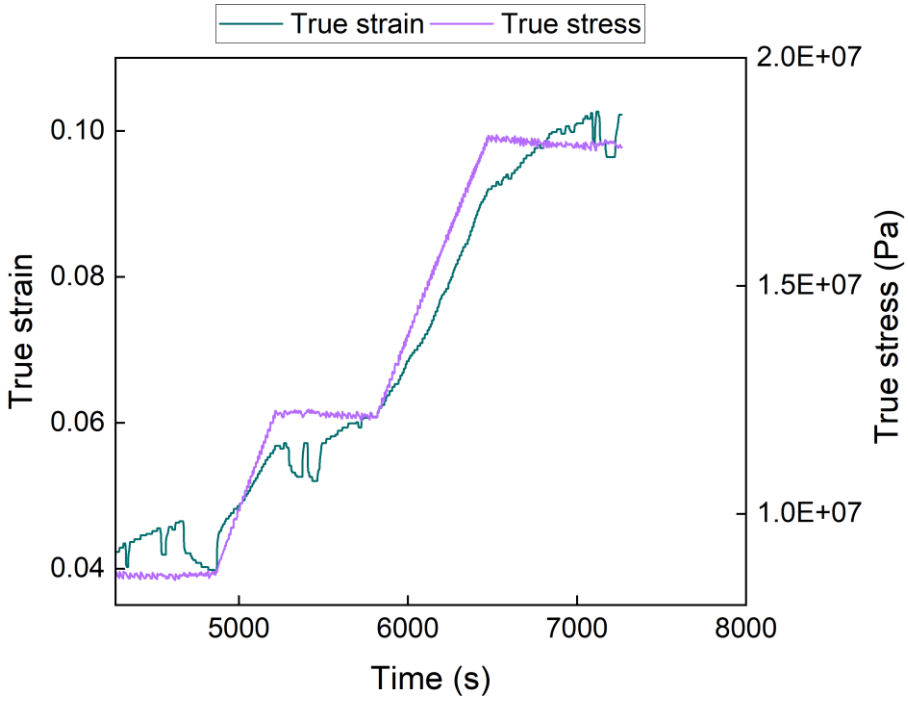

Figure B.3: Time-stress-strain curve generated during high-temperature compression experiment of Sample A conducted at 700 °C.

Table B.1: Strain rates extracted from high-temperature compression test data for Sample A.

Temperature (°C)	**Strain rate (s^{-1})**		
	13 MPa	20 MPa	31 MPa
600	8.36×10^{-6}	7.56×10^{-6}	8.94×10^{-6}
650	4.97×10^{-6}	7.06×10^{-6}	9.89×10^{-6}
700	1.52×10^{-5}	1.71×10^{-5}	1.87×10^{-5}

B.1.2 Raw data for Sample B

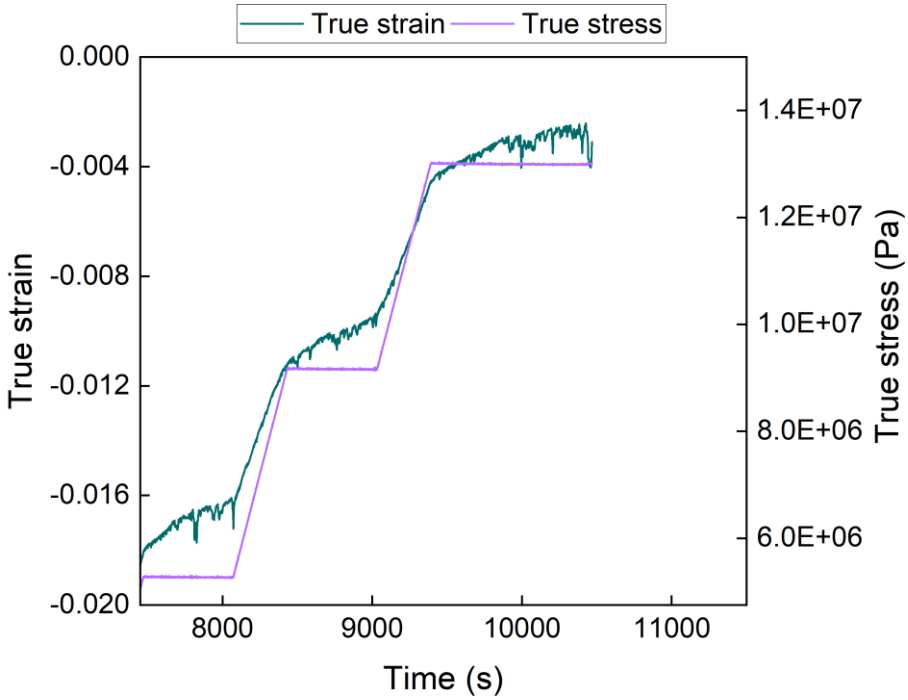

Figure B.4: Time-stress-strain curve generated during high-temperature compression experiment of Sample B conducted at 600 °C.

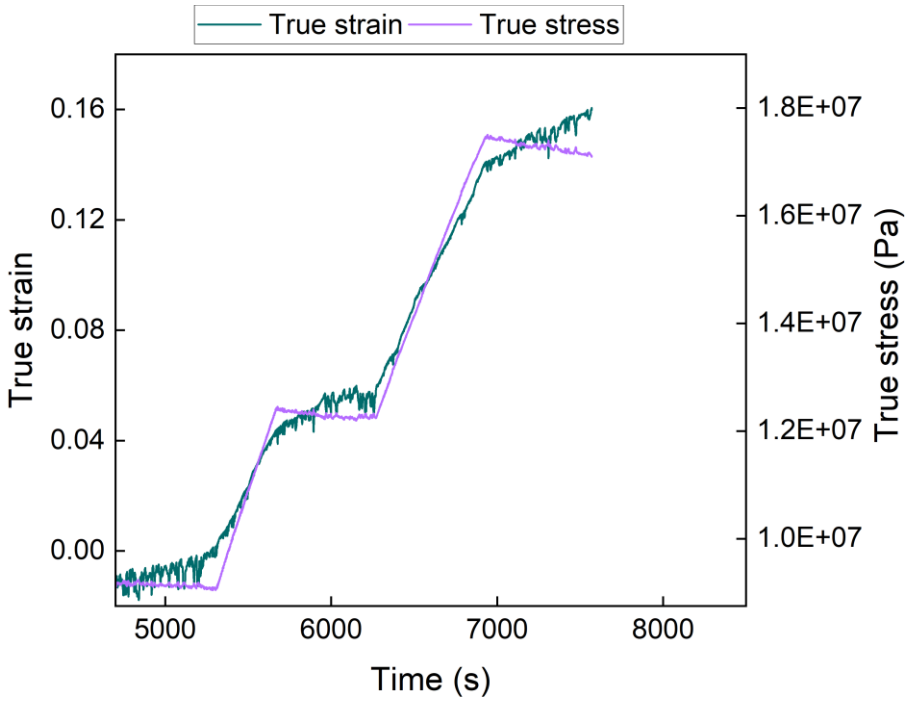

Figure B.5: Time-stress-strain curve generated during high-temperature compression experiment of Sample B conducted at 650 °C.

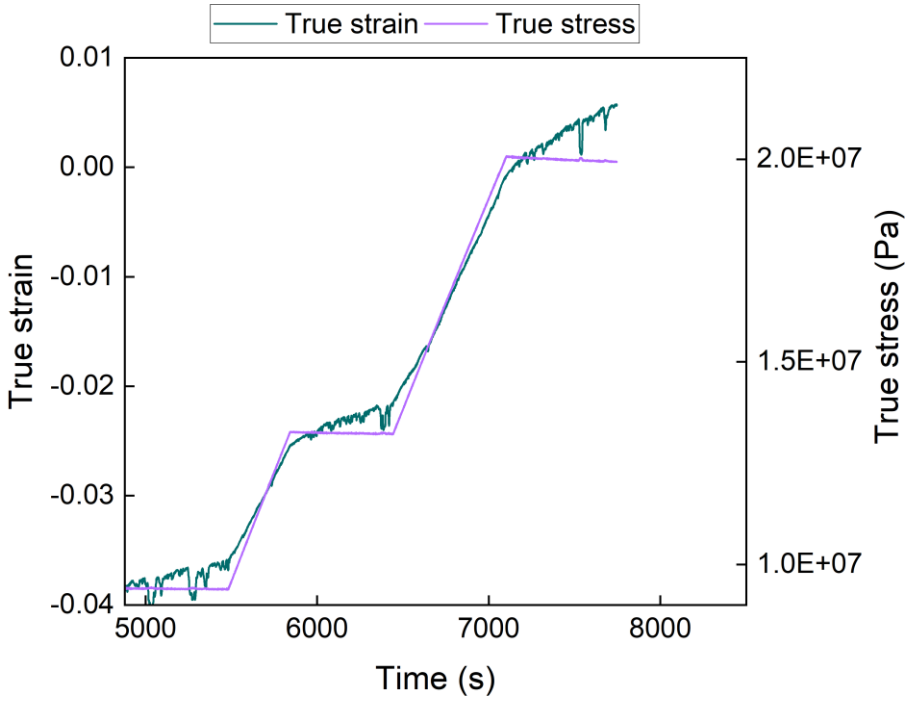

Figure B.6: Time-stress-strain curve generated during high-temperature compression experiment of Sample B conducted at 700 °C.

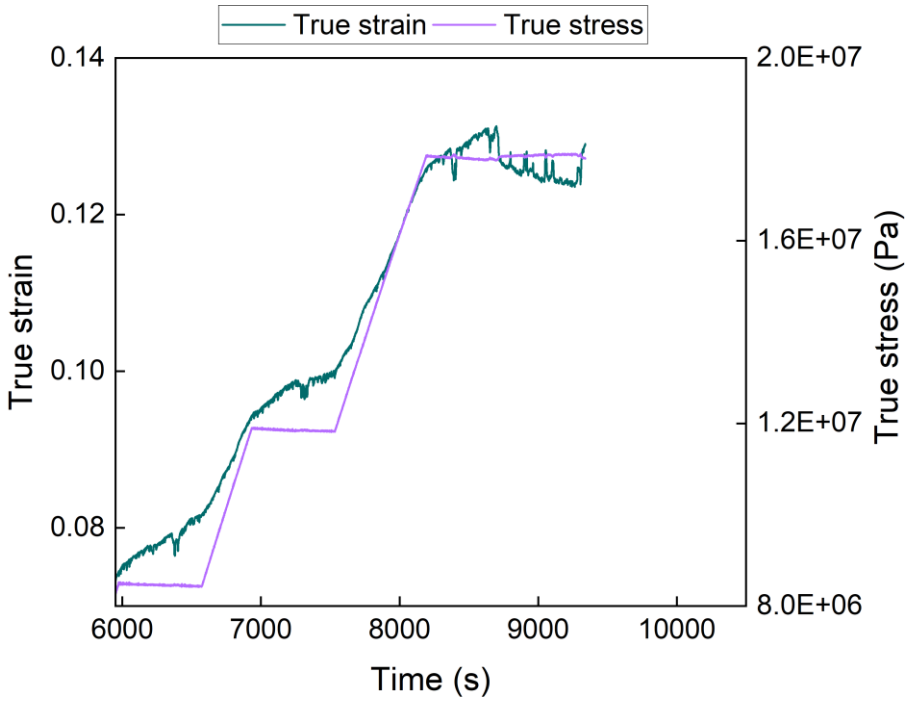

Figure B.7: Time-stress-strain curve generated during high-temperature compression experiment of Sample B conducted at 750 °C.

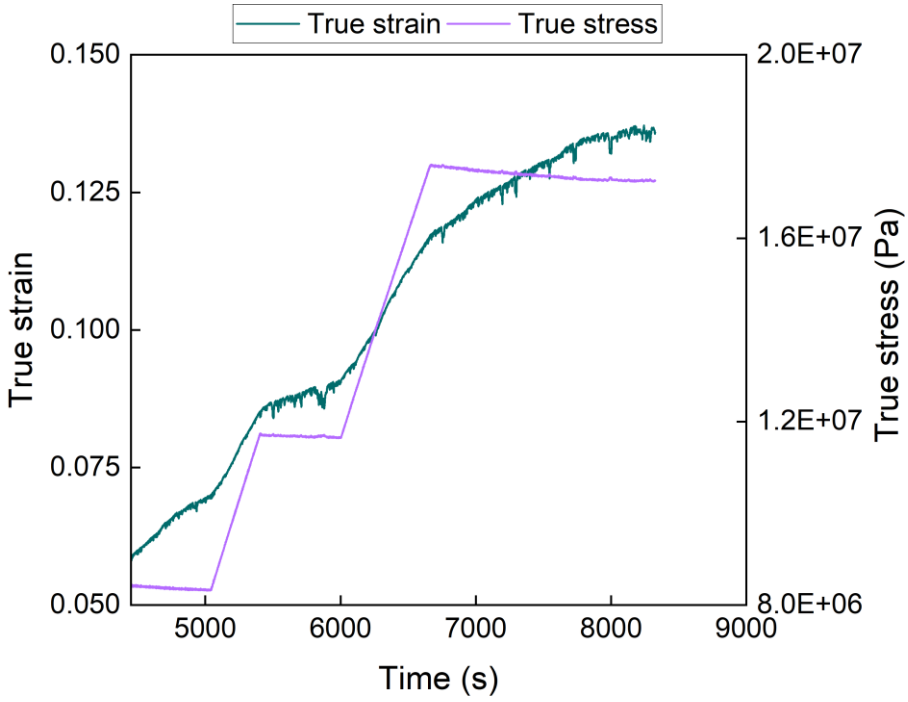

Figure B.8: Time-stress-strain curve generated during high-temperature compression experiment of Sample B conducted at 800 °C.

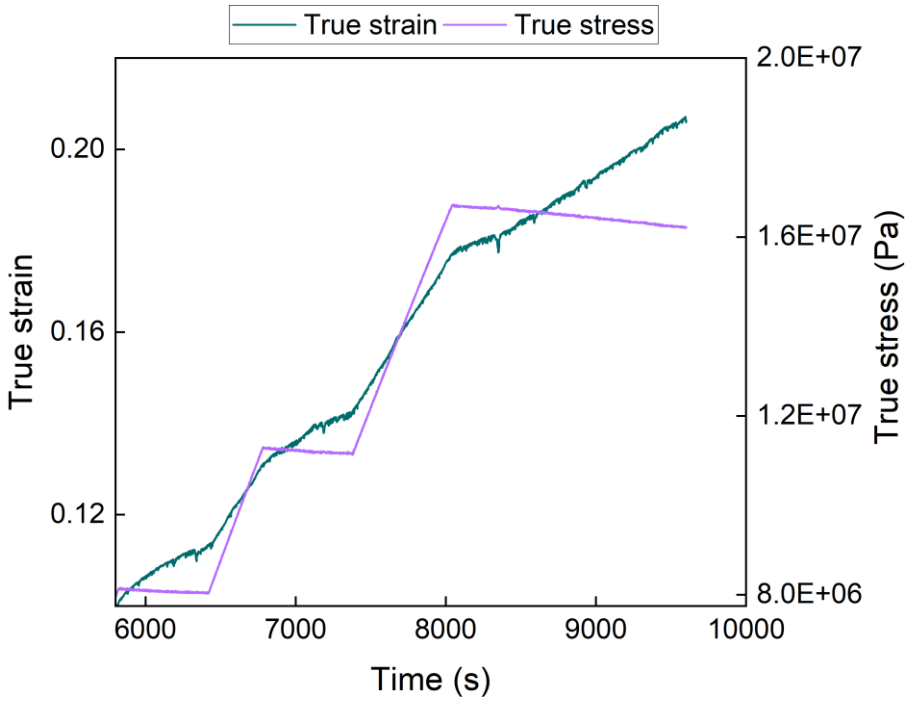

Figure B.9: Time-stress-strain curve generated during high-temperature compression experiment of Sample B conducted at 850 °C.

Table B.2: Strain rates extracted from high-temperature compression test data for Sample B.

Temperature (°C)	**Strain rate (s^{-1})**				
	5 MPa	9 MPa	13 MPa	20 MPa	31 MPa
600	1.91×10^{-6}	2.37×10^{-6}	1.37×10^{-6}	--	--
650	--	1.49×10^{-5}	2.66×10^{-5}	2.71×10^{-5}	--
700	--	3.98×10^{-6}	5.08×10^{-6}	9.00×10^{-6}	--
750	--	--	1.07×10^{-5}	8.57×10^{-6}	9.75×10^{-6}
800	--	--	1.95×10^{-5}	7.08×10^{-6}	1.22×10^{-5}
850	--	--	1.88×10^{-5}	1.88×10^{-5}	1.98×10^{-5}

B.1.3 Raw data for Sample C

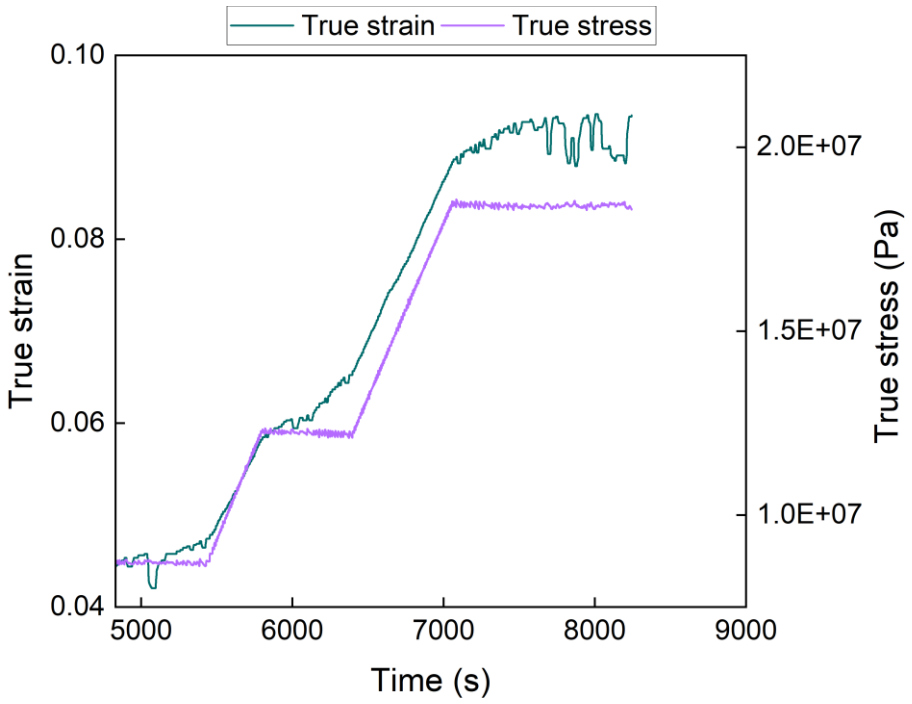

Figure B.10: Time-stress-strain curve generated during high-temperature compression experiment of Sample C conducted at 600 °C.

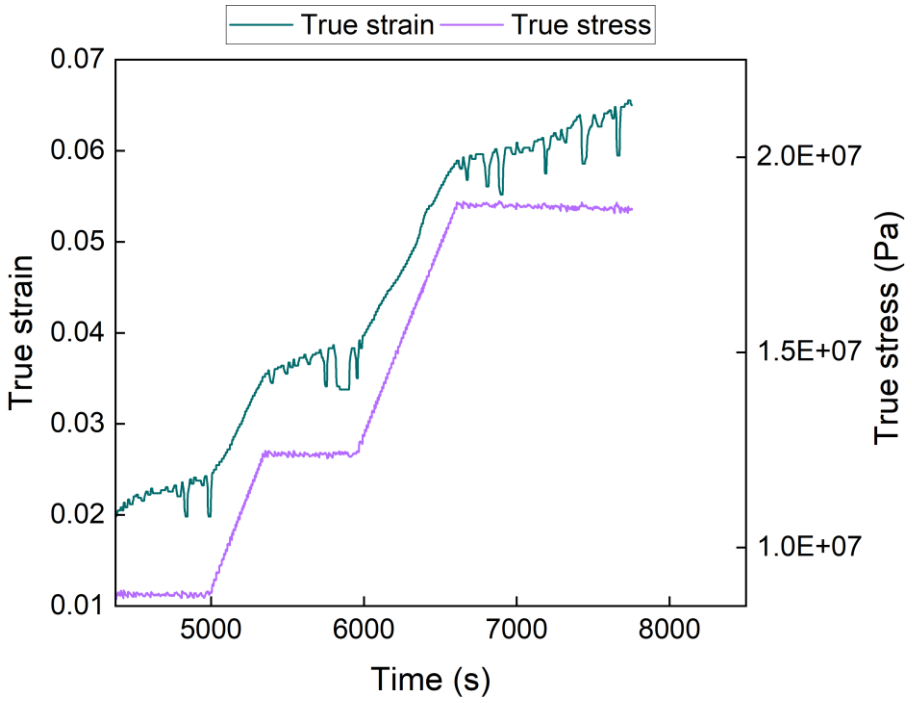

Figure B.11: Time-stress-strain curve generated during high-temperature compression experiment of Sample C conducted at 650 °C.

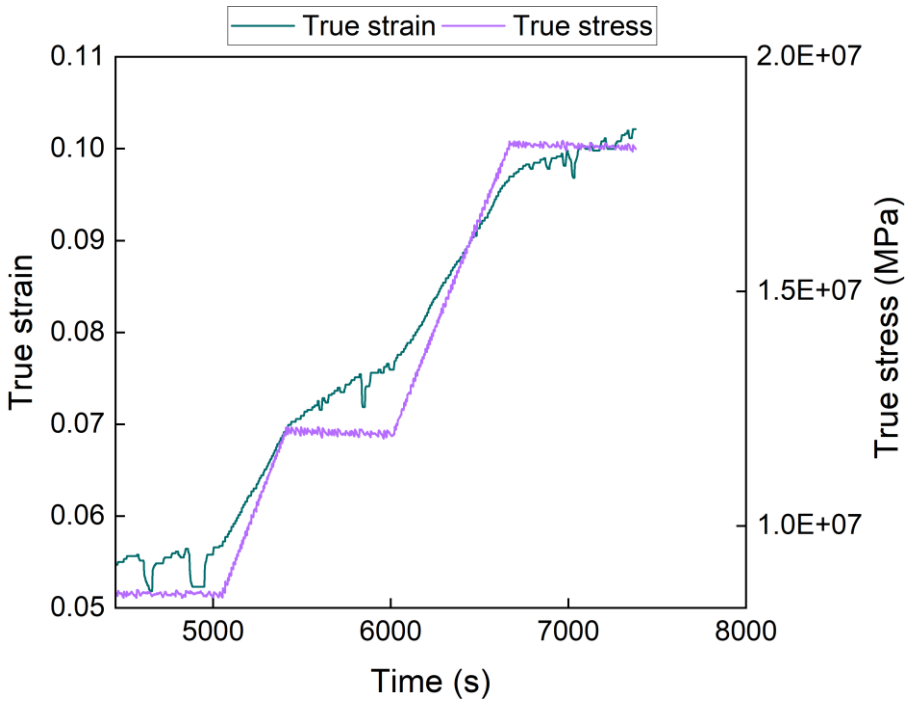

Figure B.12: Time-stress-strain curve generated during high-temperature compression experiment of Sample C conducted at 700 °C.

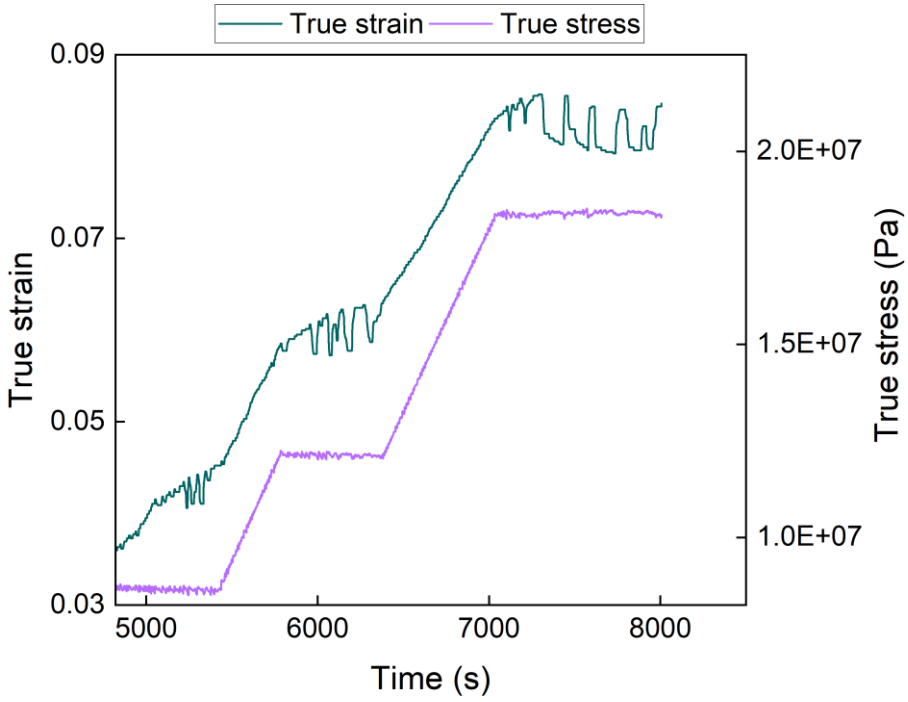

Figure B.13: Time-stress-strain curve generated during high-temperature compression experiment of Sample C conducted at 750 °C.

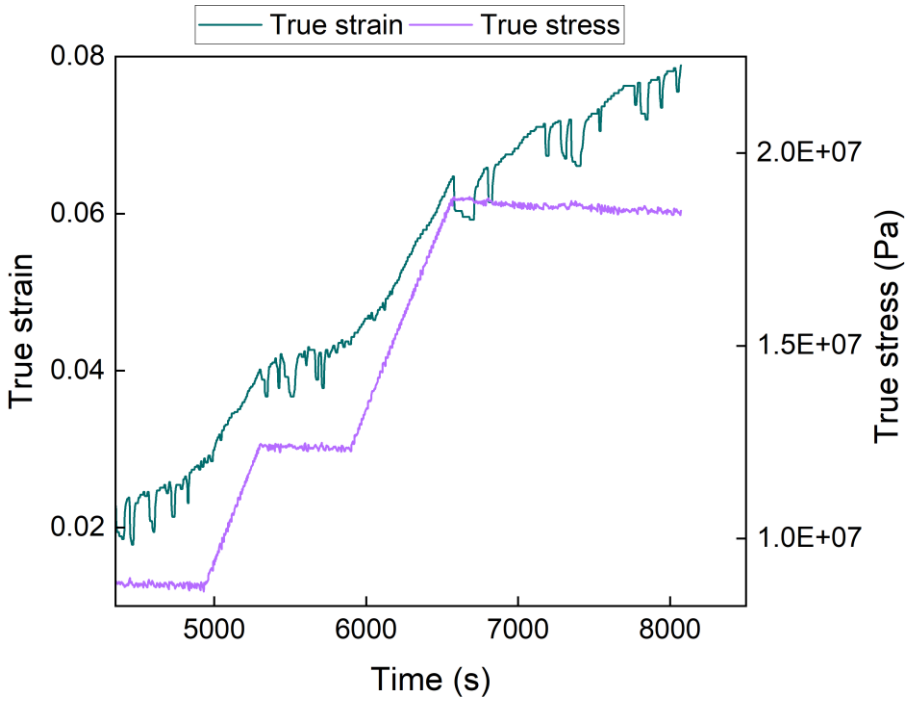

Figure B.14: Time-stress-strain curve generated during high-temperature compression experiment of Sample C conducted at 800 °C.

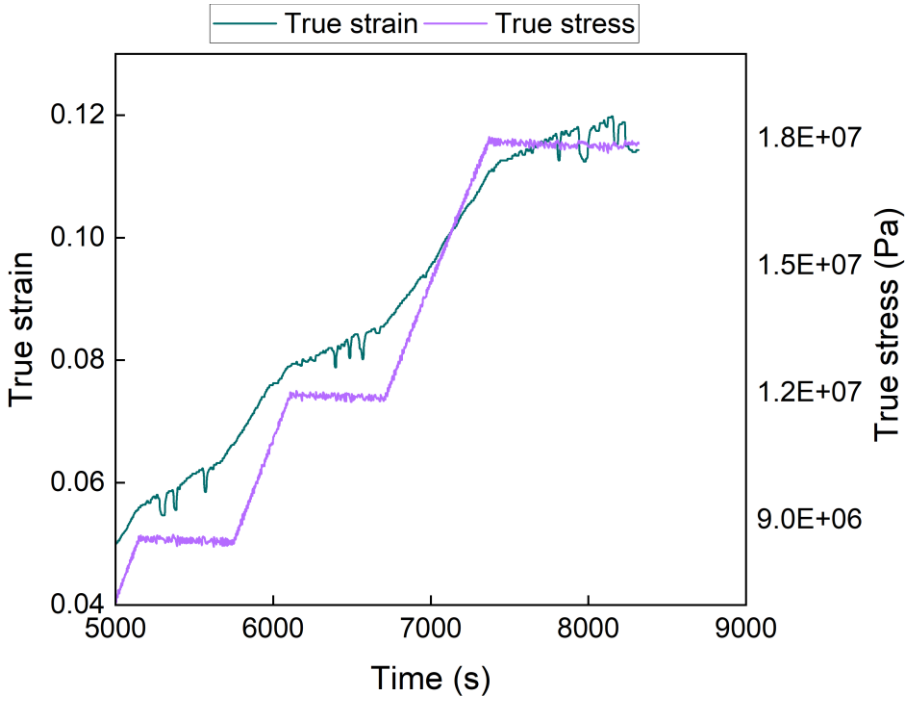

Figure B.15: Time-stress-strain curve generated during high-temperature compression experiment of Sample C conducted at 850 °C.

Table B.3: Strain rates extracted from high-temperature compression test data for Sample C.

Temperature (°C)	**Strain rate (s^{-1})**		
	13 MPa	20 MPa	31 MPa
600	1.01×10^{-5}	1.17×10^{-5}	9.20×10^{-6}
650	3.32×10^{-6}	5.36×10^{-6}	5.77×10^{-6}
700	8.49×10^{-6}	1.33×10^{-5}	5.60×10^{-5}
750	1.40×10^{-5}	8.34×10^{-6}	9.24×10^{-6}
800	1.22×10^{-5}	9.48×10^{-6}	1.11×10^{-5}
850	1.31×10^{-5}	1.33×10^{-5}	1.63×10^{-5}

B.1.4 Raw data for Sample D

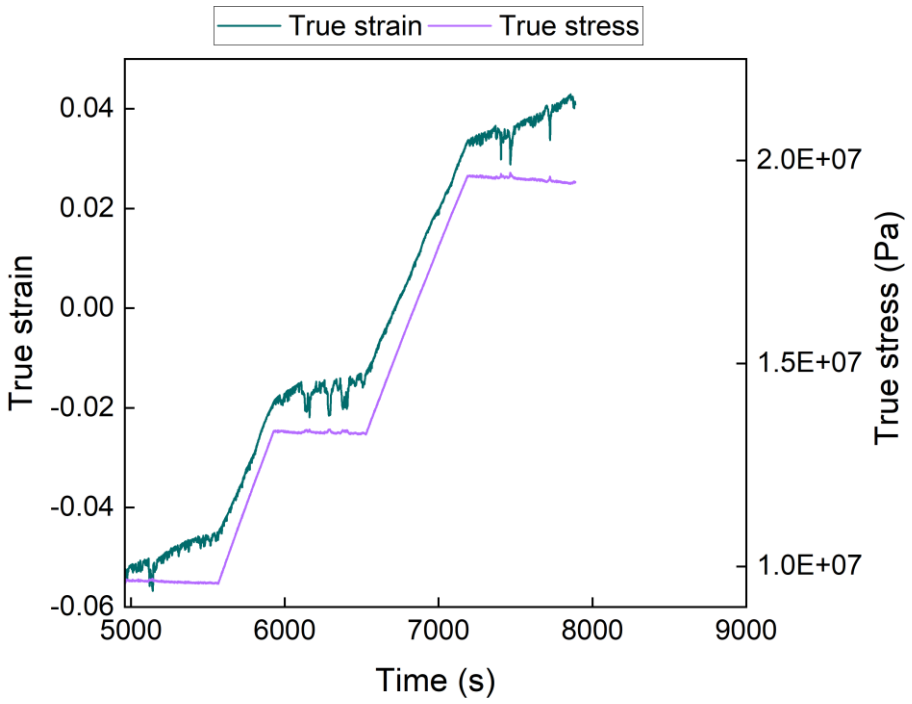

Figure B.16: Time-stress-strain curve generated during high-temperature compression experiment of Sample D conducted at 600 °C.

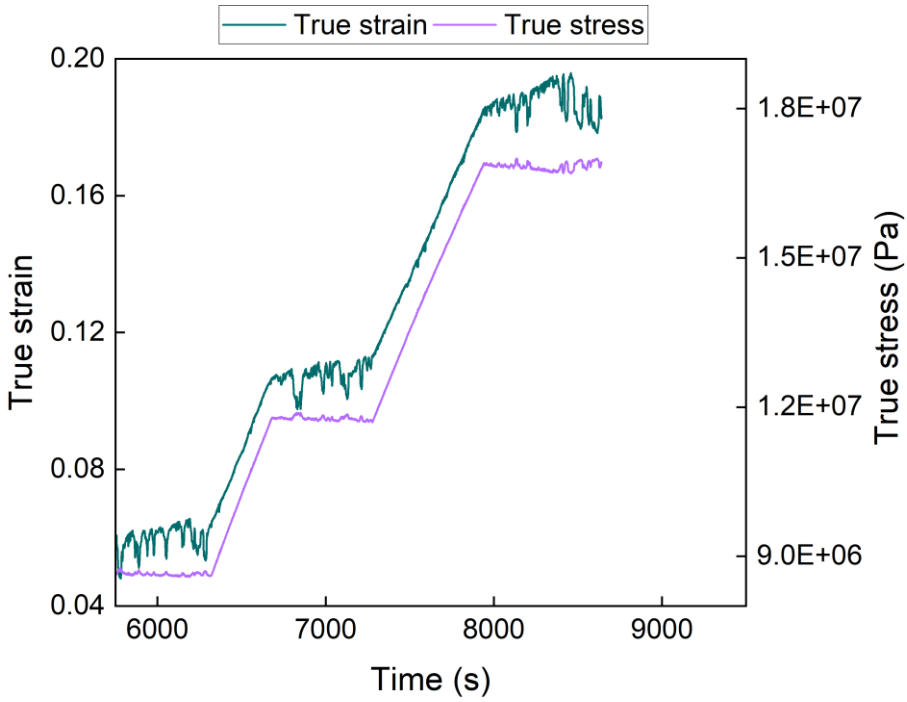

Figure B.17: Time-stress-strain curve generated during high-temperature compression experiment of Sample D conducted at 650 °C.

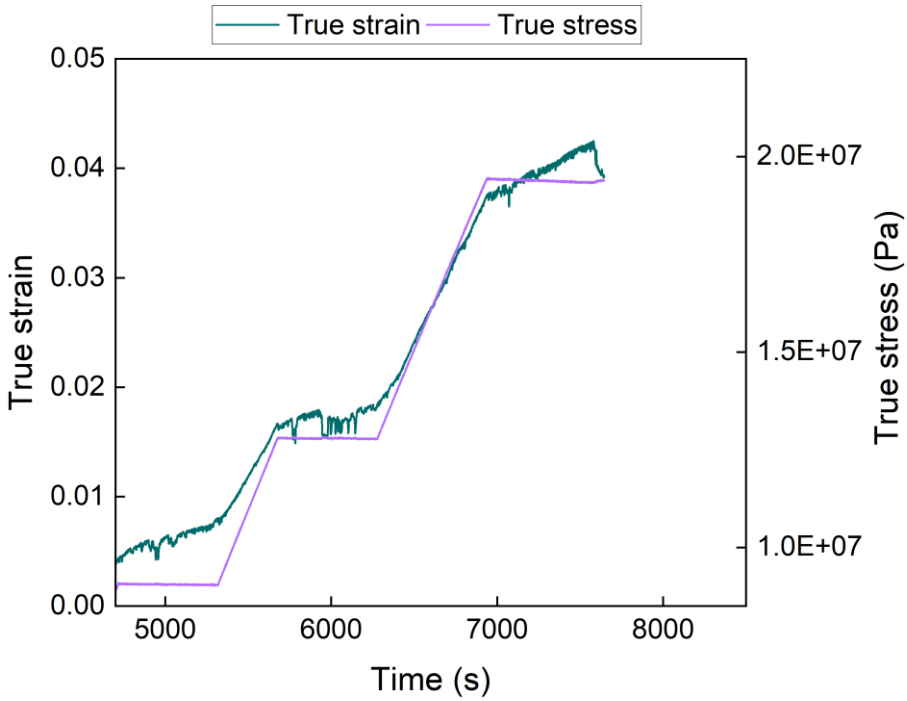

Figure B.18: Time-stress-strain curve generated during high-temperature compression experiment of Sample D conducted at 700 °C.

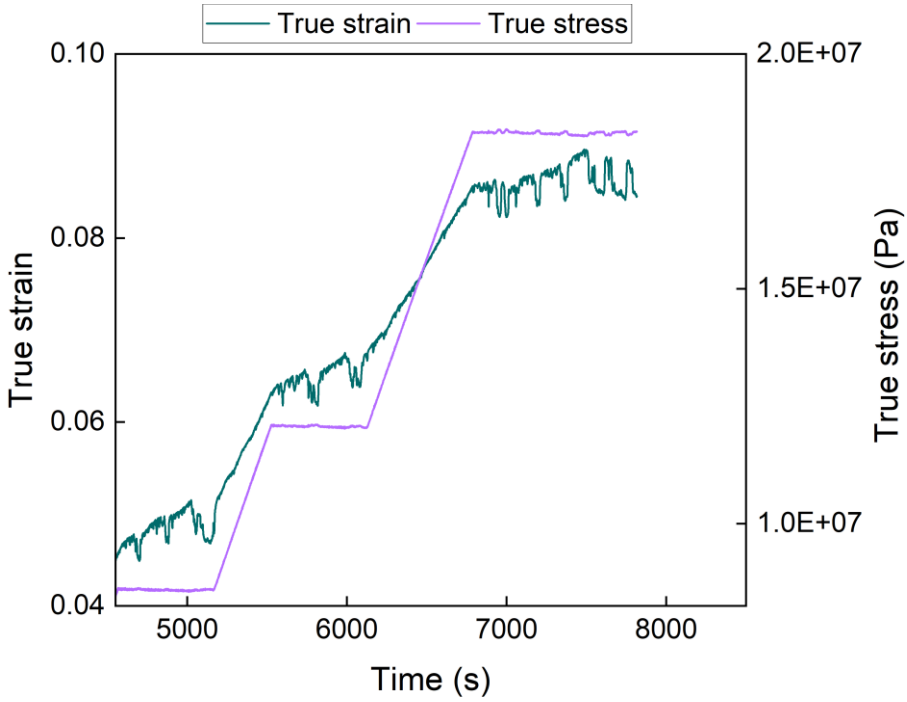

Figure B.19: Time-stress-strain curve generated during high-temperature compression experiment of Sample D conducted at 750 °C.

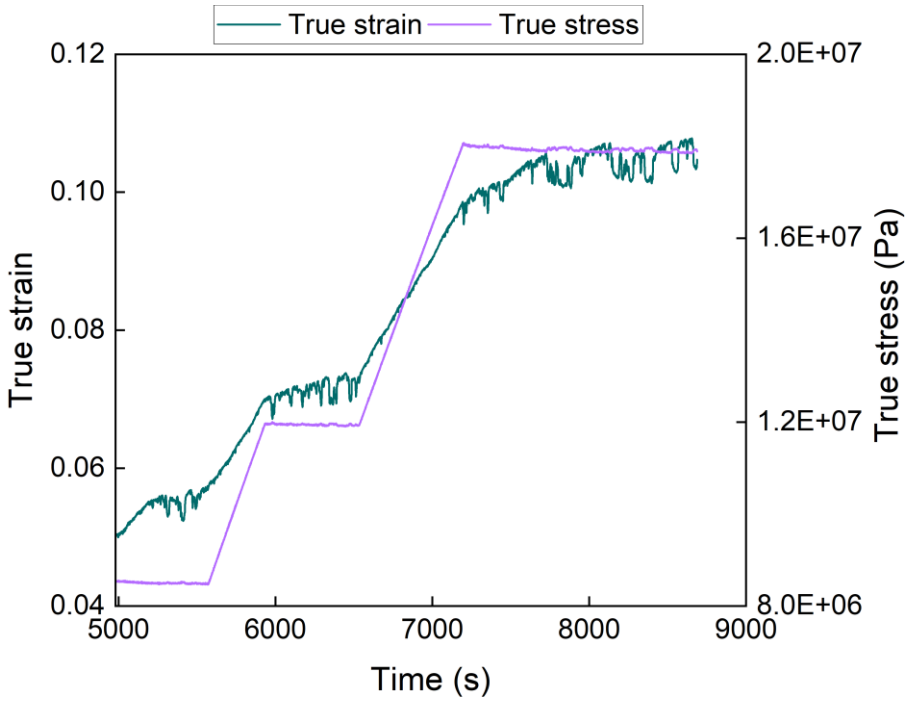

Figure B.20: Time-stress-strain curve generated during high-temperature compression experiment of Sample D conducted at 800 °C.

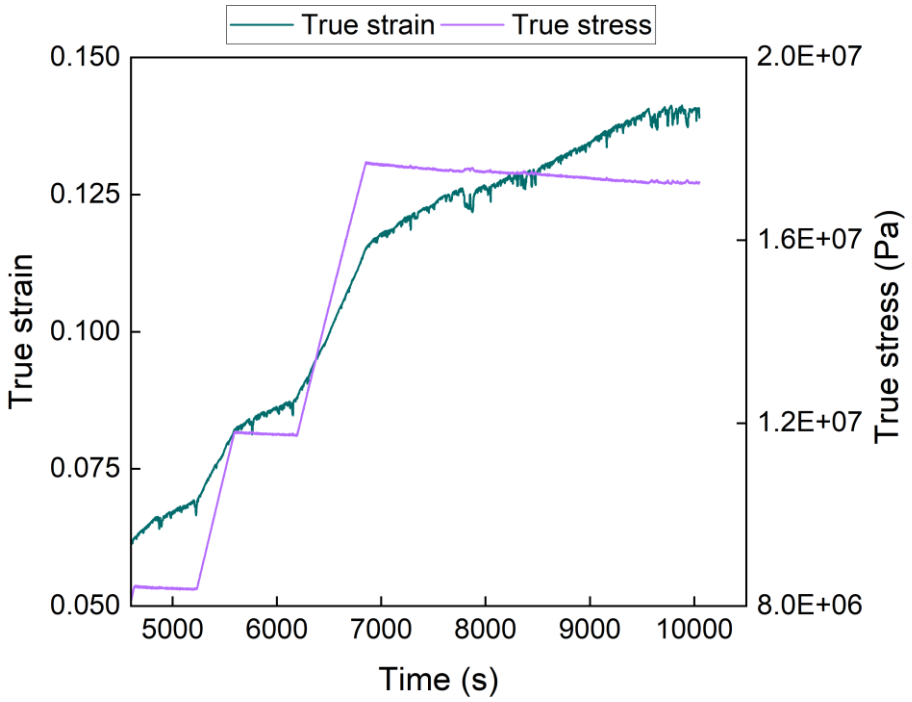

Figure B.21: Time-stress-strain curve generated during high-temperature compression experiment of Sample D conducted at 850 °C.

Table B.4: Strain rates extracted from high-temperature compression test data for Sample D.

Temperature (°C)	**Strain rate (s^{-1})**			
	9 MPa	13 MPa	20 MPa	31 MPa
600	1.02×10^{-5}	5.00×10^{-6}	1.29×10^{-5}	--
650	1.57×10^{-5}	6.09×10^{-6}	1.86×10^{-5}	--
700	4.70×10^{-6}	6.50×10^{-6}	7.78×10^{-6}	--
750	--	1.05×10^{-5}	4.67×10^{-6}	5.34×10^{-6}
800	--	1.02×10^{-5}	5.27×10^{-6}	1.36×10^{-5}
850	--	1.24×10^{-5}	8.27×10^{-6}	8.71×10^{-6}

B.1.5 Raw data for Sample E

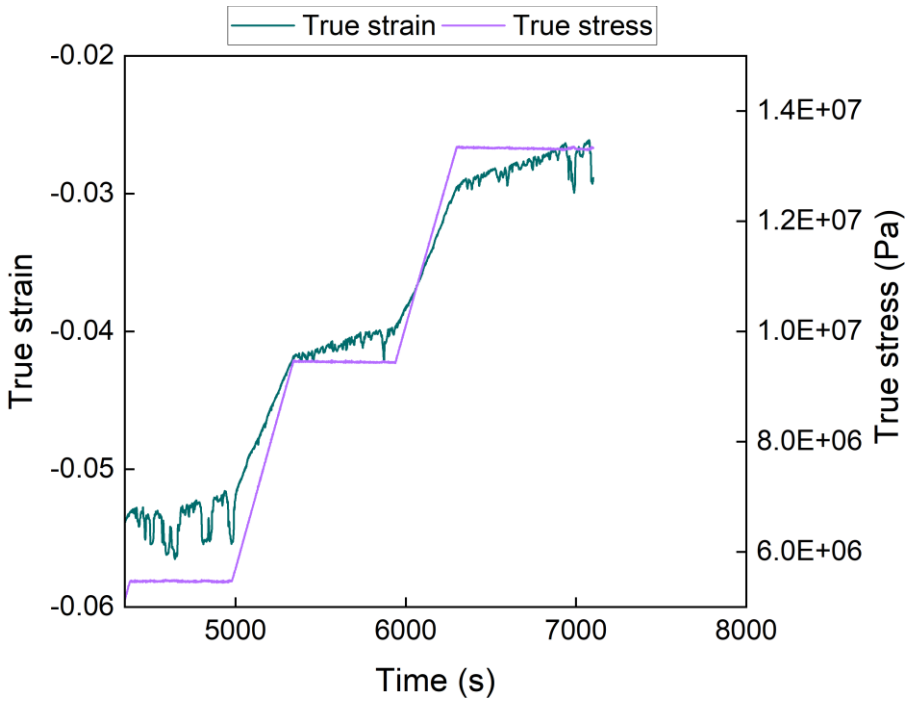

Figure B.22: Time-stress-strain curve generated during high-temperature compression experiment of Sample E conducted at 600 °C.

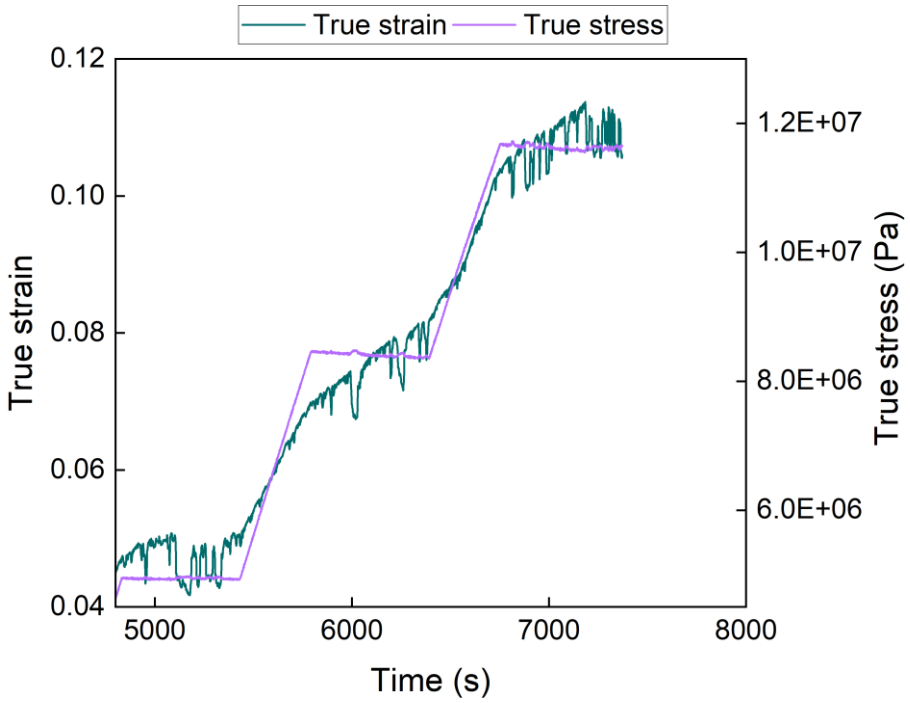

Figure B.23: Time-stress-strain curve generated during high-temperature compression experiment of Sample E conducted at 650 °C.

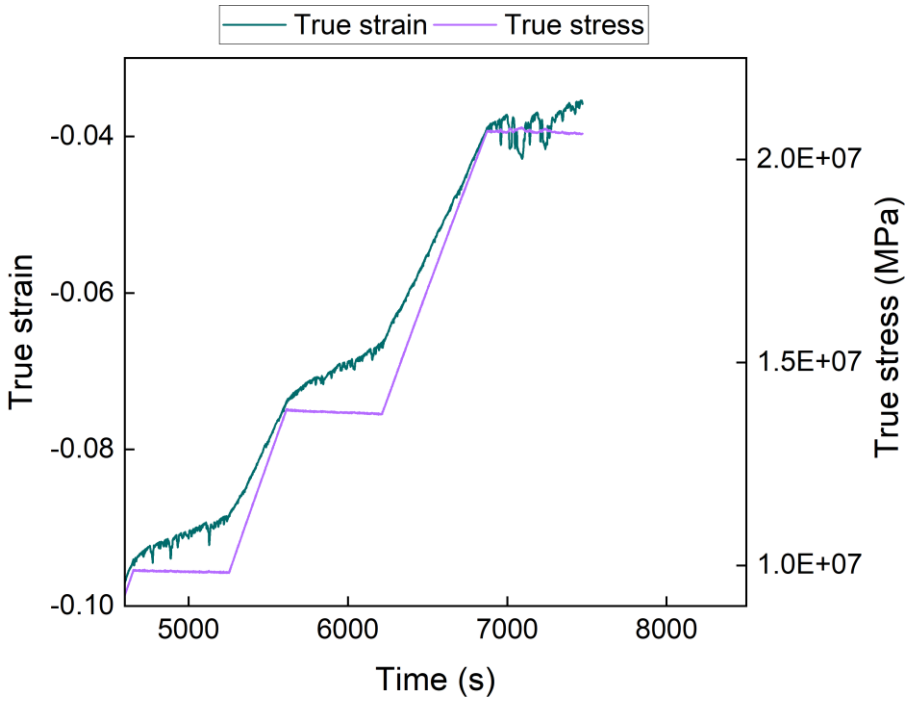

Figure B.24: Time-stress-strain curve generated during high-temperature compression experiment of Sample E conducted at 750 °C.

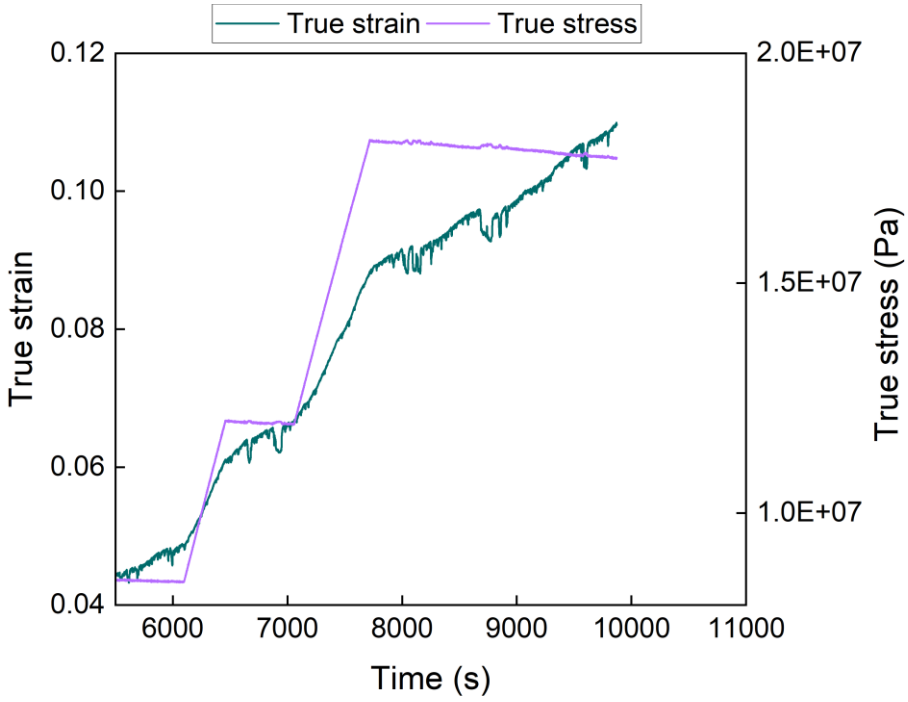

Figure B.25: Time-stress-strain curve generated during high-temperature compression experiment of Sample E conducted at 800 °C.

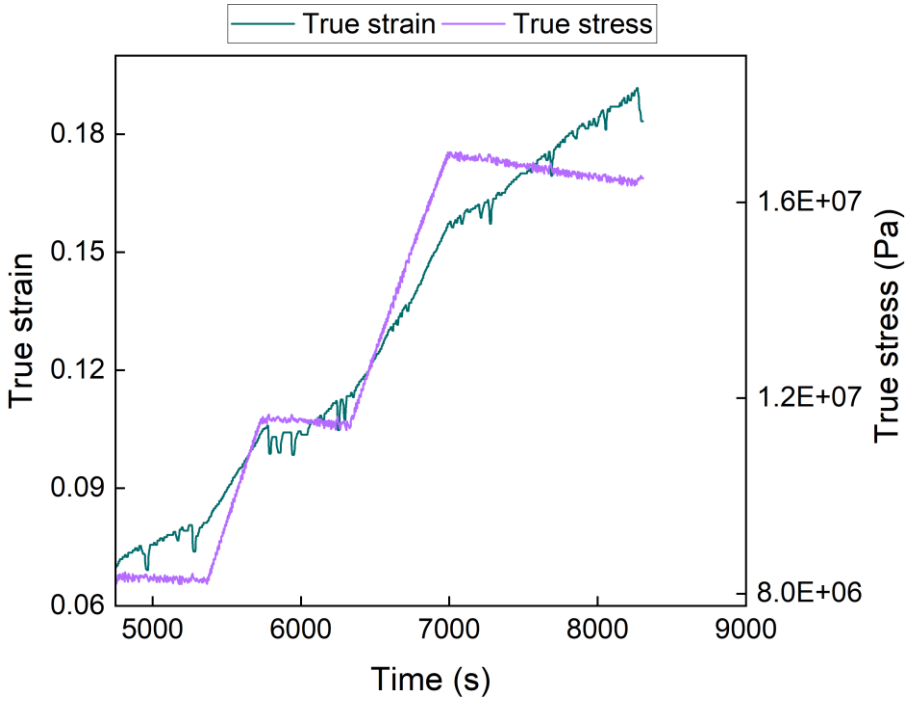

Figure B.26: Time-stress-strain curve generated during high-temperature compression experiment of Sample E conducted at 850 °C.

Table B.5: Strain rates extracted from high-temperature compression test data for Sample E.

Temperature (°C)	**Strain rate (s^{-1})**				
	5 MPa	9 MPa	13 MPa	20 MPa	31 MPa
600	4.50×10^{-6}	3.56×10^{-5}	3.81×10^{-5}	--	--
650	1.24×10^{-5}	1.89×10^{-5}	2.00×10^{-5}	--	--
750	--	8.20×10^{-6}	1.09×10^{-5}	1.31×10^{-5}	--
800	--	8.16×10^{-6}	7.53×10^{-6}	9.78×10^{-6}	--
850		--	1.41×10^{-5}	1.89×10^{-5}	2.79×10^{-5}

B.1.6 Raw data for Sample F

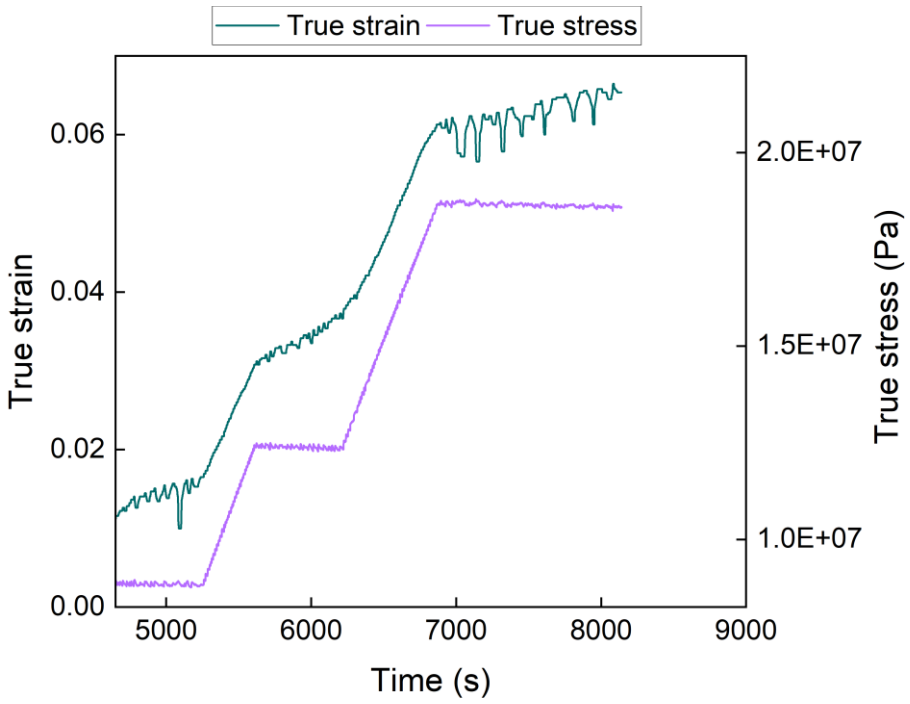

Figure B.27: Time-stress-strain curve generated during high-temperature compression experiment of Sample F conducted at 600 °C.

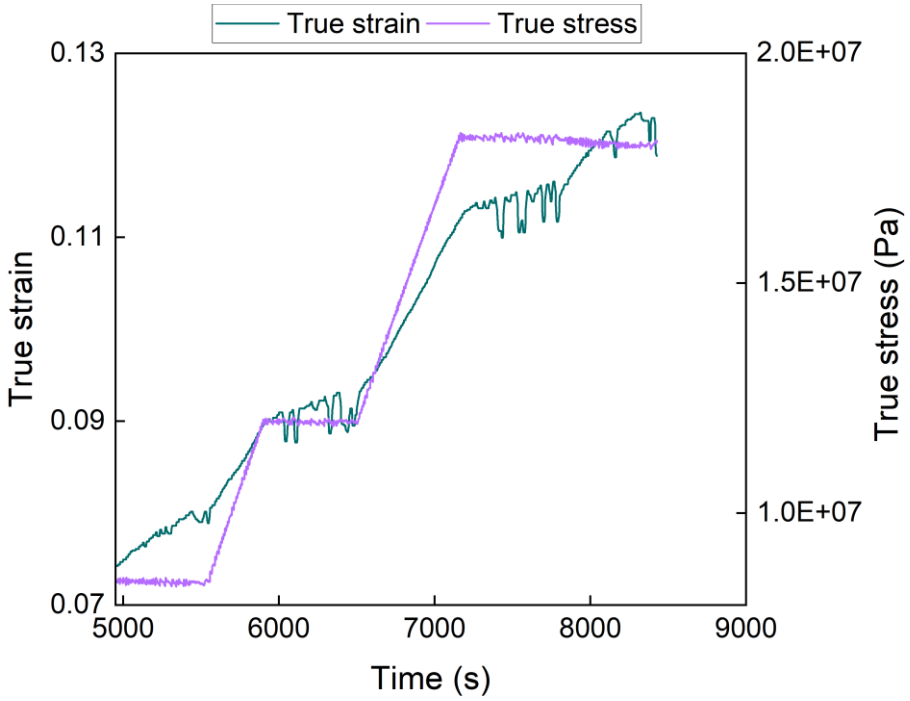

Figure B.28: Time-stress-strain curve generated during high-temperature compression experiment of Sample F conducted at 650 °C.

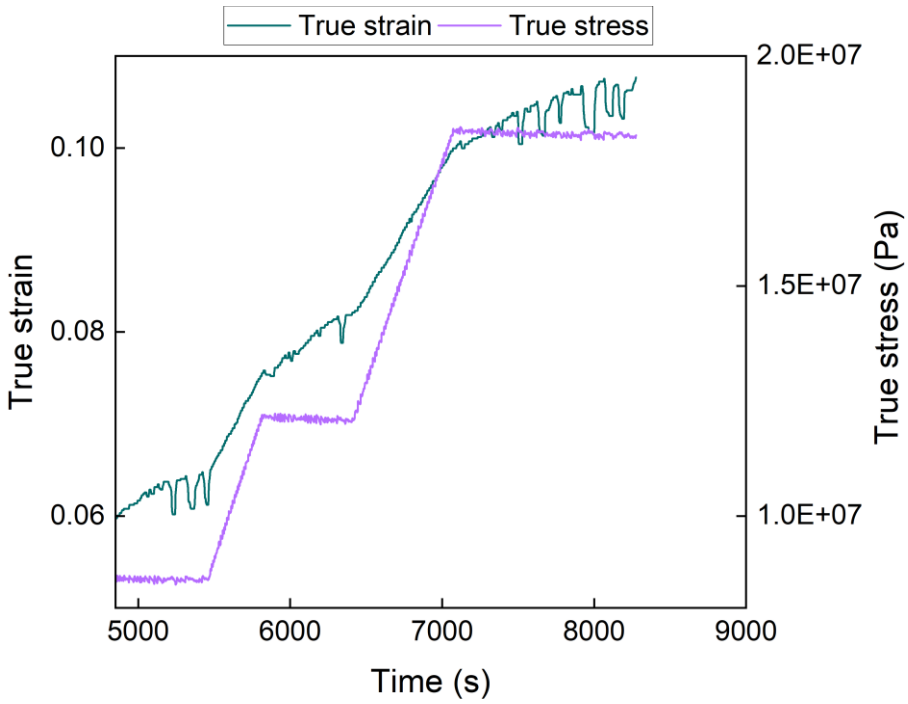

Figure B.29: Time-stress-strain curve generated during high-temperature compression experiment of Sample F conducted at 700 °C.

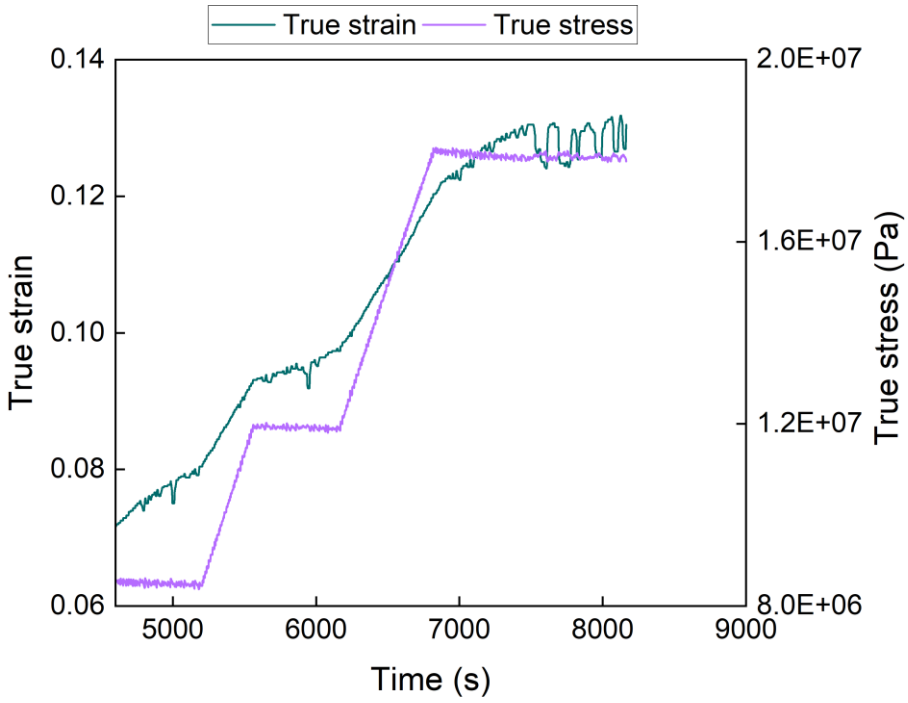

Figure B.30: Time-stress-strain curve generated during high-temperature compression experiment of Sample F conducted at 750 °C.

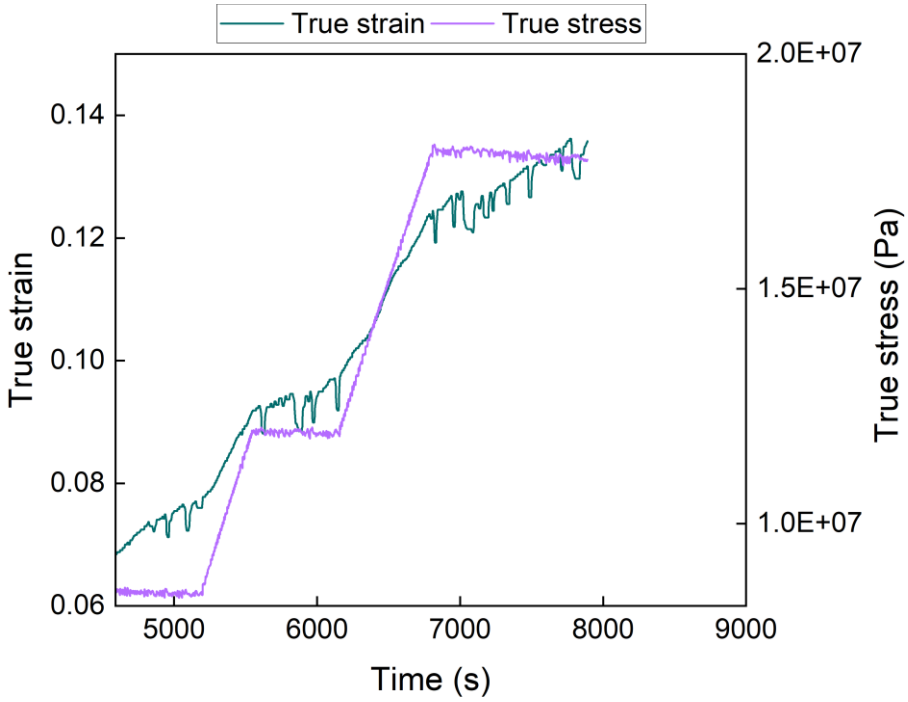

Figure B.31: Time-stress-strain curve generated during high-temperature compression experiment of Sample F conducted at 800 °C.

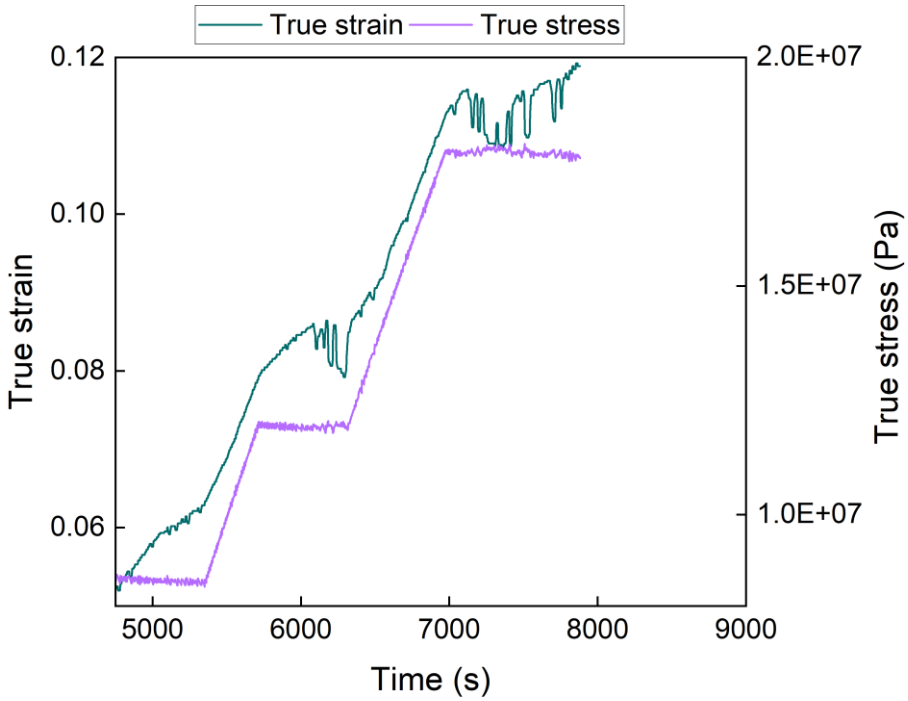

Figure B.32: Time-stress-strain curve generated during high-temperature compression experiment of Sample F conducted at 850 °C.

Table B.6: Strain rates extracted from high-temperature compression test data for Sample F.

Temperature (°C)	**Strain rate (s^{-1})**		
	13 MPa	20 MPa	31 MPa
600	4.42×10^{-6}	9.85×10^{-6}	4.86×10^{-6}
650	5.25×10^{-6}	9.96×10^{-6}	9.97×10^{-6}
700	4.91×10^{-6}	1.19×10^{-5}	5.51×10^{-6}
750	1.31×10^{-5}	1.39×10^{-5}	1.40×10^{-5}
800	1.20×10^{-5}	6.88×10^{-6}	1.27×10^{-5}
850	1.45×10^{-5}	1.81×10^{-5}	1.75×10^{-5}

B.2 Activation energy

The activation energy Q for Samples A – F (Table 4.1) were calculated using Eqn. 4.1. Activation energy was calculated by plotting $\ln(\dot{\varepsilon})$ versus $^{1}/_{T}$ at a fixed load and taking the slope. The calculated activation energies are shown in Fig. B.33.

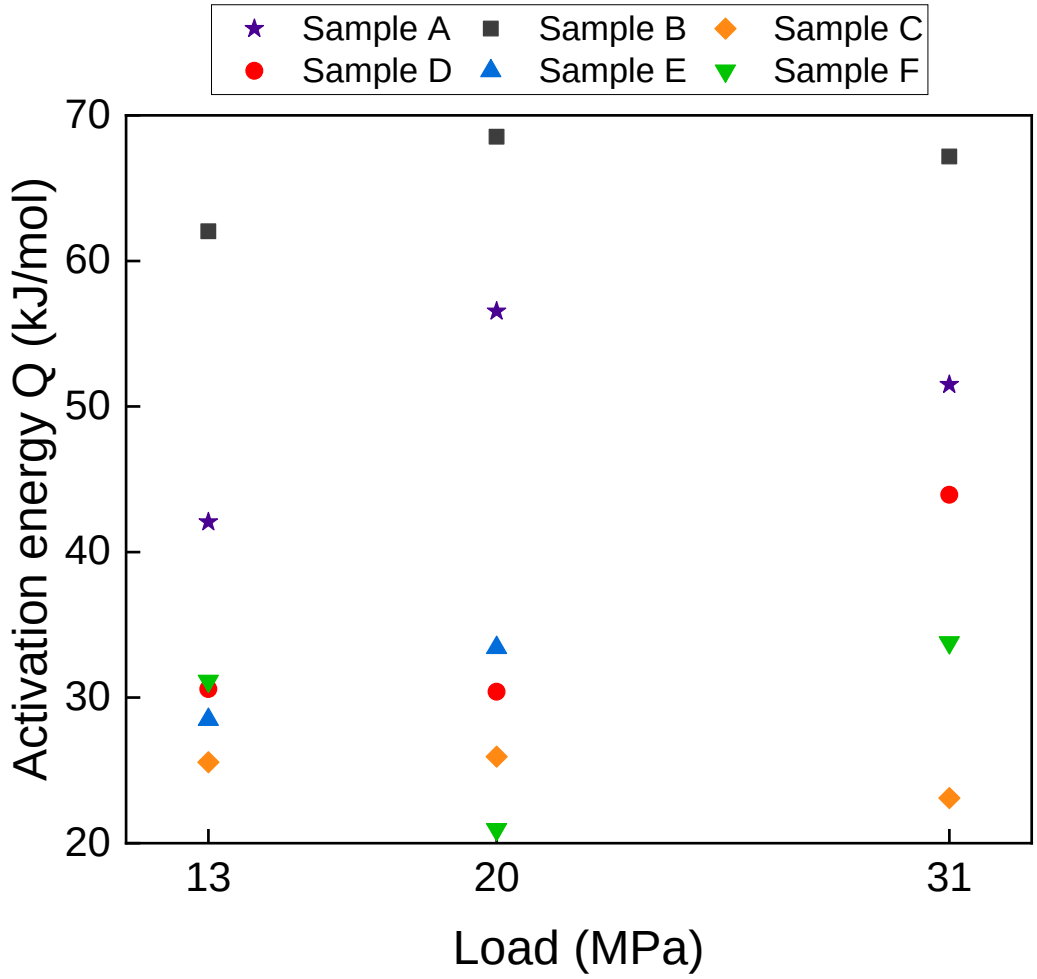

Figure B.33: Calculated activation energy for nanocrystalline (Sample A), fine-grained (Samples B – D), and coarse-grained (Samples E and F) samples deformed at increasing loads.

B.3 Grain size sensitivity

The grain size sensitivity p for Samples A – F (Table 4.1) were calculated using Eqn. 4.1. Grain size sensitivity was calculated by dividing $\ln(\dot{\varepsilon})$ by $\ln(D)$ at a fixed temperature. The calculated grain size sensitivities are shown in Fig. B.34.

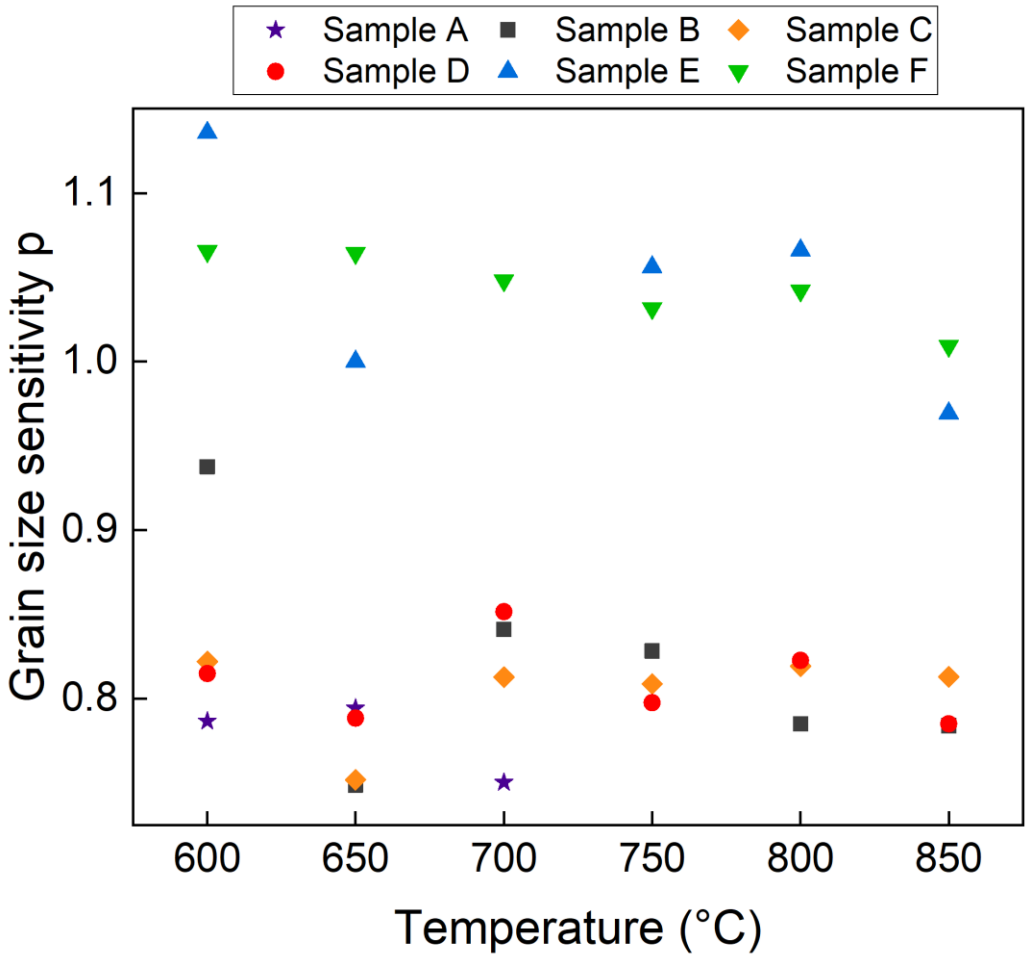

Figure B.34: Calculated grain size sensitivities for nanocrystalline (Sample A), fine-grained (Samples B – D), and coarse-grained (Samples E and F) samples deformed over a range of temperatures.

B.4 Long-hold, high-load experiments

In addition to the high-temperature deformation experiments outlined in Chapter 4, additional deformation experiments were carried out at temperatures of 700 °C and a load of 50 MPa. Samples B – D (Table 4.1) were held at 50 MPa for 1.5 hr to generate a strain-time curve for each experiment, as shown in Fig. B.35. Strain rate results for the long-hold, high-load experiments are shown in Table B.7.

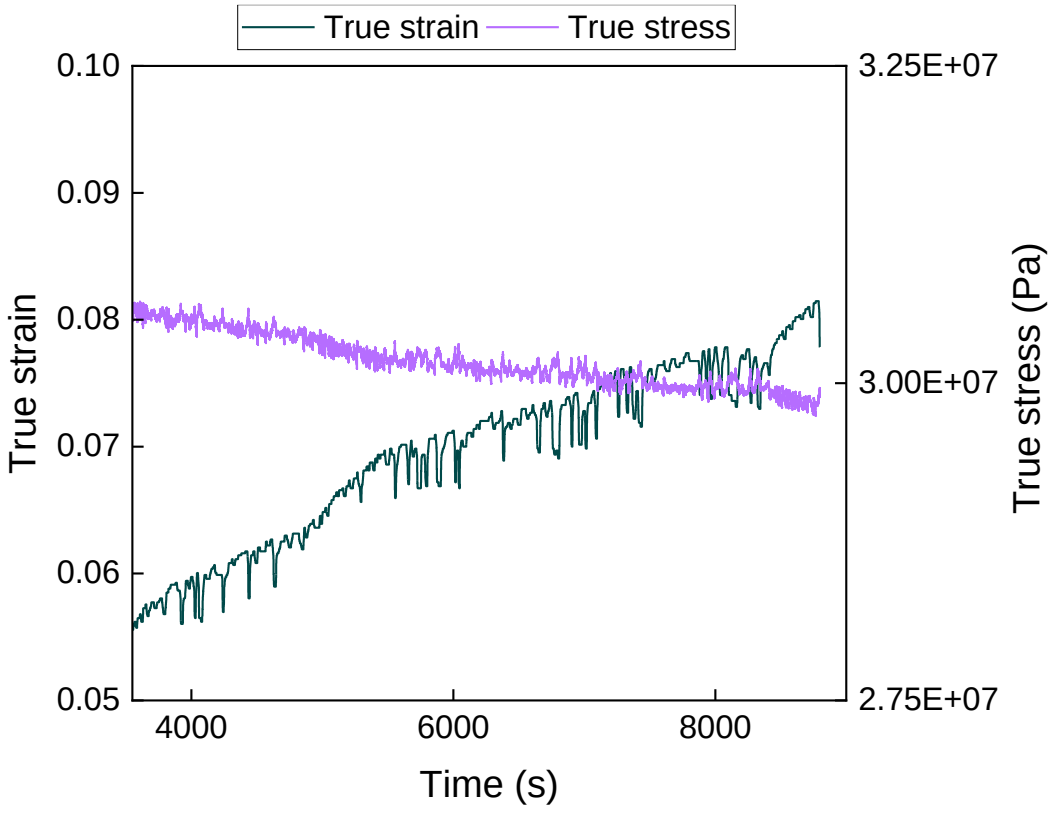

Figure B.35: A representative true strain vs. time graph that was generated during long-hold, high-load experiments.

Table B.7: Measured strain rates for long-hold high-load experiments conducted at a temperature of 700 °C and a load of 50 MPa for Samples B – D.

Sample ID	**Strain rate (s^{-1})**
B	1.3×10^{-5}
C	4.3×10^{-6}
D	6.7×10^{-6}